A Search for Long Lived Neutral Particles Decaying to Hadronic States in Proton-Proton Collisions in the ATLAS Detector at $\sqrt{s} = 8$ TeV and $\sqrt{s} = 13$ TeV at the LHC

Rachel Rosten

A dissertation
submitted in partial fulfillment of the
requirements for the degree of

Doctor of Philosophy

University of Washington

2017

Reading Committee:

Gordon Watts, Chair

Henry Lubatti

Stephen Sharpe

Program Authorized to Offer Degree:
Physics

University of Washington

Abstract

A Search for Long Lived Neutral Particles Decaying to Hadronic States in Proton-Proton Collisions in the ATLAS Detector at $\sqrt{s} = 8$ TeV and $\sqrt{s} = 13$ TeV at the LHC

Rachel Rosten

Chair of the Supervisory Committee:
Dr. Gordon Watts
Physics

A search for the decay of a heavy scalar boson into pairs of long-lived neutral particles in 20.3 fb^{-1} of proton proton collisions at $\sqrt{s} = 8$ TeV and 3.2 fb^{-1} at $\sqrt{s} = 13$ TeV in the ATLAS detector is presented. The search focuses on final states where both long lived particles decay within the hadronic calorimeter of the detector, resulting in jets with unusual properties. No excess was observed and limits were set on the lifetime of the long lived particles for various combinations of scalar boson and long lived particle masses.

TABLE OF CONTENTS

Page

LIST OF FIGURES

ACKNOWLEDGMENTS

I would like to thank the many people who have worked with me and helped me as I earned my degree. My advisor, Gordon Watts, has given me advise on all aspects of my research, writing, and career. Many others have been a part of the team contributing to my research, including Daniel Blackburn, Andrea Coccaro, Henry Lubatti, Daniela Salvatore, Emma Torro, and Monica Verducci. This analysis was a team effort, and without them this thesis, rather than the publication and public results we have presented together, may have been the only testimate to my work. Likewise to all of ATLAS I owe my gratitude. I would also like to thank my friends and family, who have put up with my fretting and doubts as long as they. Without them, I cannot say how much of my mind and happiness would be left to me.

Chapter 1

THEORETICAL BACKGROUND

The motivation for long-lived particle searches begins with the near-completeness of the Standard Model. Three of the four known forces and all observed particles are represented, along with their interactions, within the theoretical framework of the Standard Model. It has been remarkably successful at predicting and describing the subatomic world, but is not complete. There is, of course, the noticeable absence of gravity. Other observed phenomena, such as dark matter or the local (and perhaps universal) baryon asymmetry, are also not explained by the Standard Model. We necessarily seek further evidence of physics beyond the Standard Model to explore the underlying phenomena behind our current observations. With an endless supply of possible models produced by industrious theorists it is prudent to devise some general searches for new physics based upon shared features of many models. One common element of many theories is the presence of long-lived particles, where here "long" is not infinite but is large enough for particles to possess macroscopic decay lengths. This analysis searches for one such type of long-lived particle with the optimistic intent of discovering physics beyond the Standard Model and the more pragmatic intent of eliminating phase space for theories containing such particles.

1.1 The Standard Model

The Standard Model (SM) of particle physics describes the known fundamental particles of nature and their interactions. These particles are the six quarks, six leptons, twelve gauge bosons, the Higgs boson, and all their corresponding anti-particles. They can be can be neatly displayed in a single table as in Table 1.1. What follows is a brief description of these particles and their properties followed by a similarly brief description of the Standard Model.

Table 1.1: Standard Model Fundamental Particles

	Fermion Gen I	Fermion Gen II	Fermion Gen III	Bosons
Leptons	$\boldsymbol{e}$ -1 $\frac{1}{2}$ 0.511 MeV	$\boldsymbol{\mu}$ -1 $\frac{1}{2}$ 105.7 MeV	$\boldsymbol{\tau}$ -1 $\frac{1}{2}$ 1.777 GeV	$\boldsymbol{\gamma}$ 0 1 0
	$\boldsymbol{\nu_\mathrm{e}}$ 0 $\frac{1}{2}$ <2.2 eV	$\boldsymbol{\nu_\mu}$ 0 $\frac{1}{2}$ <0.17 MeV	$\boldsymbol{\nu_\tau}$ 0 $\frac{1}{2}$ <15.5 GeV	$\boldsymbol{W^\pm}$ ±1 1 80.4 GeV
Quarks	$\boldsymbol{u}$ $\frac{2}{3}$ $\frac{1}{2}$ 2.3 MeV	$\boldsymbol{c}$ $\frac{2}{3}$ $\frac{1}{2}$ 1.275 GeV	$\boldsymbol{t}$ $\frac{2}{3}$ $\frac{1}{2}$ 173.07 GeV	$\boldsymbol{Z}$ 0 1 91.2 GeV
	$\boldsymbol{d}$ $-\frac{1}{3}$ $\frac{1}{2}$ 4.8 MeV	$\boldsymbol{s}$ $-\frac{1}{3}$ $\frac{1}{2}$ 95 MeV	$\boldsymbol{b}$ $-\frac{1}{3}$ $\frac{1}{2}$ 4.18 GeV	$\boldsymbol{g}$ 0 1 0
	↑ EM Charge	↑ Spin	↑ Mass	$\boldsymbol{h}$ 0 0 125 GeV

Table 1.2: The particles of the Standard Model are shown organized by the three fermion generations separated by quarks and leptons on the left and the bosons in the last column on the right. Beneath each particle label is, from left to right, its electromagnetic charge in units of e, its spin, and its mass. Quark masses are quoted at a renormalization scale $\mu = 2$ GeV.

1.1.1 Particles and Forces

Leptons and quarks are both fermions and therefore possess half-integer spin. They are differentiated by the presence of color charge in the quarks. The strong force, responsible for the confinement of quarks and gluons, acts only on particles carrying color charge. The Higgs and the mediators of the forces, the W^+, W^-, Z, and the photon, are all bosons, integer spin particles that can interact (when allowed by other conserved quantities) with the fermions as well as with one another (except for the photon).

The leptons come in six flavors forming three generations of spin 1/2 particles. For each flavor there exists the corresponding anti-particle. We have, in the first generation, the electron and the electron neutrino. In the second are the muon and muon neutrino while the third contains the tau and tau neutrino. The electron, muon, and tau each carry a unit of electric charge while the neutrinos are eponymously neutral. The neutrinos themselves are nearly massless and often approximated as massless in particle physics (collider) interactions. The observation of neutrino flavor observations [12, 13] indicates that there is a non-zero difference between the neutrino masses so at most one can be truly massless. The SM takes them as massless but neutrino masses can be non-trivially added.

The six quarks are similarly found in three generations. The down and up quarks, responsible for the familiar proton and neutron, possess nearly degenerate mass and carry charges of $-\frac{1}{3}e$ and $+\frac{2}{3}e$ respectively. The strange and charm quarks forms the second generation, while the bottom and top quarks form the third with similar charges. The mass differences between quarks is increasingly large and the most massive quark, the top, is so short lived that it is the single quark to escape the effects of confinement. This is not because the top does not experience the strong force, but because it decays via the weak force with a lifetime smaller than the timescale of the strong force.

Confinement is the result of the strong force which governs the interaction of color charge, either red, green, or blue, carried by quarks as well as gluons. The strong force acts between colored particles and increases with distance, forcing quarks into color singlet states of trios of valence quarks or quark-antiquark pairs. Only color singlets can exist as free particles. If a gluon existed in the color singlet state it would allow for interaction via the strong force over large distances. No evidence of such an interaction has been observed.

The bosons which mediate the forces between particles are all spin 1 particles, while the Higgs boson is a scalar. The vector bosons are absorbed and emitted by other particles, "communicating" the forces between them. The photon mediates the electromagnetic force, the W and Z bosons the weak force, and the eight gluons mediate the strong force. The gluons exist in color states composed of two colors, always one color and one anti-color, each. They are never color singlets and thus they, like the quarks, are subject to confinement. The role of the Higgs will be discussed later in this section.

1.1.2 Standard Model Formulation

The Standard Model (SM) of particle physics is a non-abelian gauge field theory. As a field theory, it is a formulation of a set fields extending throughout spacetime, the excitations of which are quantized and are the particles we observe. Forces between particles are the result of interactions of the boson fields with themselves and the fermion fields. As a gauge theory it is invariant under a continuous group of local transformations. Specifically, such transformations leave the action - the integral of the Lagrangian between two times - invariant. The gauge fields correspond to gauge groups whose generators are the gauge bosons. The SM is based on the SU(3) × SU(2) × U(1) gauge symmetry describing the strong force ($\mathrm{SU(3)_C}$), weak force ($\mathrm{SU(2)_L}$), and electromagnetic force ($\mathrm{U(1)_Y}$).

Global invariance under a U(1) or SU(N) gauge symmetry corresponds to a conserved charge or charges. To revisit quantum electrodynamics (QED), we can consider U(1) in isolation. The global U(1) invariance corresponds to invariance under rotation of the phase of the field and necessitates the conservation of electric charge. Local invariance, where the degree of rotation is spacetime dependent, in turn necessitates the electromagnetic gauge field, A^μ, and thus the photon, to maintain the invariance of the action. There are $N^2 - 1$ generators of an SU(N) group, hence three weak gauge bosons and the eight gluons. In the case of the strong force the global SU(3) invariance necessitates the conservation of color charges while the gluon field is required for its local invariance.

QCD is a non-abelian gauge theory and is thus asymptotically free provided there are sufficiently few flavors of quarks [14]. Given an SU(3) gauge group the maximum number of allowed flavors is 16 - QCD is safe with its mere 6 quark flavors. The possible existence of additional, as yet unobserved, heavier quark flavors has not been ruled out. Asymptotic freedom that is the complement of confinement of quarks and gluons discussed previously. At short distances (and at high energies) the forces between particles are very weak, while at longer distances (say, around the radius of a proton), the force is strong.

In the SM Larangian the gauge group of QED is instead a result of the combined SU(2) ×

U(1) symmetry. The above-mentioned conservation of electric charge Q actually arises from global invariance under SU(2)$\times$U(1) symmetry: conservation of weak isospin, I, corresponds to global SU(2) rotations while weak hypercharge, Y, corresponds to global U(1) rotations, with electric charge given by:

$$Q = \frac{Y}{2} + I_3 \tag{1.1}$$

The generators of this SU(2) gauge group are three W bosons while that of the U(1) gauge group is the B boson. Electroweak symmetry breaking, summarized shortly, results in the transformation of these four bosons into the familiar ones and predicts the now-confirmed existence of the Higgs boson.

The SM Lagrangian is most easily understood by beginning with the QCD terms, introducing the electroweak terms, and ending with a description of the addition of mass terms.

The QCD terms can be written as:

$$\mathcal{L}_{\mathrm{QCD}} = -\frac{1}{2}\mathrm{tr}\mathbf{G}_{\mu\nu}\mathbf{G}^{\mu\nu} + i\overline{u}(\partial_\mu - ig_{\mathrm{s}}\mathbf{G}^{\mathrm{a}}_\mu T^{\mathrm{a}})\gamma^\mu u + i\overline{d}(\partial_\mu - ig_{\mathrm{s}}\mathbf{G}^{\mathrm{a}}_\mu T^{\mathrm{a}})\gamma^\mu d \tag{1.2}$$

The matrix field $\mathbf{G}_{\mu\nu}$ is the gluon field strength tensor while $\mathbf{G}^{\mathrm{a}}_\mu$ is the gluon gauge field, with the index “a” running over the eight gluon fields. The “u” and “d” terms are the Dirac spinors for up-type and down-type quarks, respectively, and are summed over all three generations. The strong coupling constant is represented by g_{s} and the SU(3) generators are T^{a}. Finally, the γ^μ are the Dirac matrices. The first term in $\mathcal{L}_{\mathrm{QCD}}$ is then the gauge term for QCD, with the quarks’ kinetic terms and their interaction terms with the gauge field arising from the right two terms.

The electroweak terms can be written as:

$$\begin{aligned}\mathcal{L}_{\mathrm{EW}} = -\frac{1}{4}B_{\mu\nu}B^{\mu\nu} - \frac{1}{8}\mathrm{tr}\mathbf{W}_{\mu\nu}\mathbf{W}^{\mu\nu} \\ +\overline{\chi}_{\mathrm{L}} i\overline{\sigma}^{\mu}(\partial_\mu - ig_1\frac{1}{2}B_\mu + i\frac{g_2}{2}\mathbf{W}_\mu)\chi_{\mathrm{L}} \\ +\overline{\nu}_{\mathrm{R}} i\overline{\sigma}^{\mu}(\partial_\mu - ig_1\frac{1}{2}B_\mu)\nu_{\mathrm{R}} \\ +\overline{e}_{\mathrm{R}} i\overline{\sigma}^{\mu}(\partial_\mu - ig_1\frac{1}{2}B_\mu)e_{\mathrm{R}}\end{aligned} \tag{1.3}$$

$$\chi_{\mathrm{L}} = \begin{pmatrix} \nu_{\mathrm{L}} \\ e_{\mathrm{L}} \end{pmatrix} \tag{1.4}$$

The gauge fields B and $\mathbf{W}$ correspond to U(1) and SU(2), respectively and their field strength tensors are in the gauge term on the top line. The lepton (e) and neutrino (ν) fields are components of χ_{L} for left-handed states and are separated for right handed states. The significance of this separation will be discussed shortly. It should also be understood that, although they are not written in Equation 1.3, analogous fields for up and down type quarks are present in the full Lagrangian. The Pauli matrices appear as σ and the two coupling constants are g_1 and g_2.

It can be easily observed in the decay of charged pions that the weak force, responsible for their decay, couples to left-handed helicity states for particles and right-handed ones for antiparticles. Helicity is the sign of the dot product of a particle's spin with its direction of motion. More accurately, the weak force couples to left-handed chiral states for particles and right-handed chiral states for antiparticles. These correspond to left-handed and right-handed helicity states, respectively, in the limit of low mass with respect to particle energy. The near-masslessness of the neutrinos present in the decay of charged pions allows the effects of this coupling to be observed via the helicity suppression of the lighter electron final state as compared to the muon final state. The spin 0 pion produces two daughters with opposite spin and momenta, and thus the same helicity, favoring decays where the left handed chiral state contains a larger right-handed helicity component for the charged daughter.

The masses of the gauge bosons presented a challenge for electroweak unification. A locally gauge invariant electroweak force required massless gauge bosons, but the weak force was known to be a short range force thought correctly to be mediated by massive particles. Fermion masses also presented a problem to unification. Consider a generic fermion mass term:

$$\mathcal{L}_{\text{mass}}^{\text{fermion}} = -\overline{\psi}_{\text{L}} M \psi_{\text{R}} + hc. \tag{1.5}$$

where M is an arbitrary mass matrix. The left- and right-handed terms are coupled, but they transform differently under SU(2). Such a mass term is not gauge invariant. The inclusion of mass terms for the massive gauge bosons and fermions must arise from some additional source.

1.1.3 Higgs Mechanism

The Higgs Mechanism [15, 16, 17, 18, 19] was the brilliant solution to the mass problem in electroweak unification [20, 21, 22]. It is the addition of a new scalar field to the Lagrangian that gains a vacuum expectation value below the scale of electroweak symmetry breaking. We can label the three W fields W_1, W_2, and W_3 and with some foresight introduce the following definitions:

$$W^{\pm} = \frac{1}{\sqrt{2}}(W_1 \mp iW_2) \tag{1.6}$$

$$\begin{pmatrix} \gamma \\ Z^0 \end{pmatrix} = \begin{pmatrix} \cos\theta_{\text{W}} & \sin\theta_{\text{W}} \\ -\sin\theta_{\text{W}} & \cos\theta_{\text{W}} \end{pmatrix} \begin{pmatrix} B \\ W^3 \end{pmatrix} \tag{1.7}$$

If θ_{W} is chosen such that:

$$\tan\theta_{\text{W}} = \frac{g_1}{g_2} \tag{1.8}$$

Then the two gauge fields can be written as:

$$Z_\mu = \frac{1}{\sqrt{g_1^2 + g_2^2}}(g_2 W_\mu^3 - g_1 B_\mu) \tag{1.9}$$

and

$$A_\mu = \frac{1}{\sqrt{g_1^2 + g_2^2}}(g_2 W_\mu^3 + g_1 B_\mu) \tag{1.10}$$

Here, $W^\pm$, Z, and A are the familiar weak and electromagnetic fields. The angle θ_W introduced here is the Weinberg weak mixing angle.

The new field is the complex scalar field ϕ:

$$\phi = \frac{1}{\sqrt{2}} \begin{pmatrix} \phi^+ \\ \phi^0 \end{pmatrix} \tag{1.11}$$

The superscripts refer to the electric charge Q of the two components. The field carries weak hypercharge $Y = 1$, so by Equation 1.1 the $I_3 = +\frac{1}{2}$ component has EM charge $Q = 1$ while the $I_3 = -\frac{1}{2}$ component is neutral.

This field is a doublet under SU(2) and so the new addition to $\mathcal{L}_\mathrm{SM}$ is:

$$\mathcal{L}_\mathrm{H} = \overline{D}_\mu \phi^\dagger D^\mu \phi - \mu^2 \phi^\dagger \phi - \lambda(\phi^\dagger \phi)^2 \tag{1.12}$$

$$D_\mu = \partial_\mu - i g_1 \frac{1}{2} B_\mu - i g_2 \frac{\sigma_i}{2} W_\mu^i \tag{1.13}$$

This is the Lagrangian of a scalar field with mass μ and a self-coupling parameter λ scaling interactions of the field with itself. The general renormalizable potential bounded from below which corresponds to such a field can be written as:

$$V(\phi) = \frac{1}{2}\mu^2 \phi^2 + \lambda \phi^4 \tag{1.14}$$

Taking $\mu^2 > 0$ and $\lambda > 0$ yields a single stable minimum for the Higgs field at 0. If, however, the mass-like term is negative $\mu^2 < 0$ and $\lambda > 0$ the scalar field has a nonzero minimum at $\langle \phi \rangle = v$ given by:

$$\frac{-\mu^2}{2\lambda} = \frac{v^2}{2} \tag{1.15}$$

where v is the vacuum expectation value, the VEV, of the field.

A convenient gauge to work in is one in which both the real and imaginary parts of ϕ^+ and the imaginary part of ϕ_0 possess a vanishing expectation value. For the remaining component $\phi \to \phi + v$ and $\mathcal{L}_\mathrm{H}$ is taken as:

$$\mathcal{L}_{\text{H}} = \frac{g_2^2 v^2}{8}[(W_\mu^1)^2 + (W_\mu^2)^2] + \frac{v^2}{8}(g_2 W_\mu^3 - g_1 B_\mu)^2 \tag{1.16}$$

Where the Pauli matrices have been applied to expand and simplify the equation. Substituting in Equations 1.6, 1.9, and 1.10 yields:

$$\mathcal{L}_{\text{H}} = \frac{1}{2}(\frac{g_2 v}{2})^2[(W_\mu^+)^2 + (W_\mu^-)^2] + \frac{1}{2}\frac{v^2(g_1^2 + g_2^2)}{2}Z_\mu^2 \tag{1.17}$$

Evidently, there are now two charged W bosons with mass $\frac{g_1 v}{2}$ and a neutral Z boson with mass $\frac{v}{2}\sqrt{g_1^2 + g_2^2}$. The terms for the photon field cancel, leaving it massless. The Z and $W^\pm$ masses are related by $m_{\text{W}} = m_{\text{Z}} \cos\theta_{\text{W}}$. If the Higgs field is present then the masses of these particles arise from electroweak symmetry breaking!

The final piece of the SM are the fermion mass terms. These are added by coupling the left and right-handed fermion fields to one another via the Higgs field, yielding a gauge invariant term. The term for up-type quarks, for example, is:

$$\mathcal{L}_{\text{mass}}^{\text{fermion}} = -\lambda_{\text{f}}\overline{\psi}_{\text{L}}\phi\psi_{\text{R}} + hc. \tag{1.18}$$

where the coupling strength λ_{f} increases with fermion mass (i.e. a Yukawa coupling).

1.2 Physics Beyond the Standard Model

Despite its successes the Standard Model is known to be incomplete. Searches for physics beyond the Standard Model (BSM) are numerous thanks to the myriad theories of the nature of BSM physics itself. The present analysis performed a search for neutral long lived particles based on one particular BSM model, a hidden sector model. However, as will be described, long lived particles (LLPs) are a common feature of many BSM models and provide strong motivation for developing analyses around their signatures.

1.2.1 Motivation

Aside from its obvious exclusion of gravity there are many observed phenomena not accounted for in the Standard Model. For example, the matter described by the SM is estimated to account for only about 5% of the energy in the observable universe. A quarter is in the form of dark matter and the remainder in the form of dark energy. Dark matter's existence was first surmised from the rotation curves of stars and galactic clusters and is now supported by numerous other measurements and observations including the gravitational lensing of background objects in the presence of stars and the anisotropies in the cosmic microwave background. Yet to date the particle nature of dark matter is unknown and the SM provides no plausible candidates. Neutrinos are too relativistic - too *hot* - to be adequate candidates for the majority of dark matter while neutral hadrons are found in an abundance too small to account for the amount of dark matter observed in other measurements. The nature of dark energy is equally uncertain despite its critical role in driving the acceleration of the expansion of the universe.

Other, perhaps more subtle, phenomena unexplained by the standard model include the Higgs mass hierarchy problem, the fermion mass hierarchy problem, and the presence of neutrino masses. Generically, a hierarchy problem is a large and seemingly unexplained difference in magnitudes of related quantities. The Higgs mass hierarchy problem results from the fact that the loop corrections to the mass squared of a scalar field are quadratically divergent.

$$m_{\text{obs}}^2 = m_0^2 + \mathcal{O}(\Lambda^2) \tag{1.19}$$

Here m_{obs} is the observed mass of the Higgs, about 125 GeV. The tree-level mass is given by $m_0^2 = -2\mu^2$ and is a free parameter in the SM. The terms included in $\mathcal{O}(\Lambda^2)$ are the one-loop corrections to the Higgs mass and are proportional to the cut-off scale for the SM, Λ. Λ is taken as the Planck scale, the energy at which the quantum effects of gravity cannot be neglected. This sets the corrections to the Higgs bare mass to $O(10^{19}\text{ GeV})^2$. While it is not impossible that the bare mass of the Higgs nearly exactly cancels out the corrections from the loop diagrams, a scenario referred to as *fine tuning*, it is certainly seen as motivation to probe for underlying mechanisms not yet discovered.

The fermion mass hierarchy problem concerns the large difference in fermion masses between generations. (In fact, whether there are only three generations is also not established by the Standard Model.) The lightest fermions, the neutrinos, present an additional challenge to the SM. That they possess mass was first demonstrated by observations of neutrino flavor changing. Neutrino flavor eigenstates are a mixture of mass eigenstates and vice versa. Hence, a neutrino created as an electron neutrino may be observed to be a different flavor when detected. Yet not only are neutrino masses absent in the SM, it only includes left-handed neutrinos while a renormalizeable model with neutrino masses would necessarily need to include right-handed neutrinos as well.

The observed asymmetry in the presence of matter versus antimatter (i.e. our existence) in the observable universe is also unexplained by the SM. The amount of asymmetry that could result from CP-violating interactions allowed by the SM is insufficient to account for the abundance of matter in the current universe. Without some extension or modification of the SM and a corresponding experimental discovery (though we might expect the latter to proceed the former), each of these topics, and others, remain discussed but not explained.

1.2.2 Long Lived Particles

Theorists provide varied and numerous models intended to address topics which the SM in known to incompletely address. Developing a search dedicated to each model is not only beyond the resources available to the physics community, it is inefficient. Instead, signatures common to many models form a better motivator for building an analysis.

One common feature of many models is the presence or one or more types of long lived particles (LLPs). A reason for their ubiquity is the presence of several mechanisms leading to LLPs. They can be the result of small couplings, conserved quantum numbers, degenerate masses, and other phenomena.

As an example, consider supersymmetry (SUSY). SUSY assigns a fermion superpartner to each SM boson and vice versa. This solves the Higgs mass hierarchy problem as the corrections from SM particles are canceled by those due to their superpartners. However, no superparticles have yet been observed, implying that SUSY must be broken. Several different proposed mechanisms exist for breaking SUSY. All either definitely, or possibly depending on parameters, contain particles which would possess long lifetimes and decay to more familiar SM particles.

Likewise, a variety of models have been introduced to explain the existence of dark matter (DM). Some of these add an extra sector, with its own gauge groups, separate from the SM sector but which can communicate via some mediator particle. These are referred to *hidden sectors* because they are hidden to the SM except via the communicator. Prior to the observation of the Higgs many such models were introduced with the Higgs as a mediator which could go unobserved if it strongly favored decays into the hidden sector. Yet extra sectors provide an easy means of accommodating DM. If the lightest hidden sector particle is stable, that is if it cannot decay to the SM via the communicator, then it is a candidate dark matter particle. Assuming the coupling between sectors is weak, then particles which *do* decay back to the SM can do so with long lifetimes.

1.2.3 Hidden Sectors

Hidden sector models [23, 24, 25, 26] propose a sector of new particles which couple to the SM via some communicator particle. These sectors are frequently a part of a broader theory but may constitute a stand-alone model as well. The hidden sector model used in the 2012 analysis is from a class of models called the Hidden Valley models. In the Hidden Valley framework a new non-abelian gauge group G_{v} adds a new sector, where the subscript “v” hereafter indicates “valley” quantities. For example, q_{v} would be a “valley quark”. This hidden sector is weakly coupled to the SM sector by a communicator particle which mixes with its hidden sector counterpart. If the communicator has a high mass and the mixing is sufficiently weak then such a sector could remain hidden until experiments generate collisions at high enough energies to access it regularly.

In the specific Hidden Valley model considered in 2012, G_{v} is confining and the sector contains at least two valley quarks q_{v} which consequently hadronize into valley hadrons. They are neutral under the Standard Model gauge group G_{SM} and thus not directly detectable (although any with infinite lifetimes would be dark matter candidates). The SM sector particles are likewise neutral under G_{v}. The massive communicator particle - in this case the Higgs or another scalar boson - requires sufficient energy for its production and thus the production of valley particles. The lightest valley particles which are produced may decay back to SM sector particles via the communicator, but need do so via an off-shell communicator and thus possess long lifetimes.

Consider a hidden sector gauge group G_{v} consisting of an $SU(3) \times U(1)$ group. A scalar field Φ is added and the $U(1)$ symmetry is spontaneously broken as in the SM. The Φ_v associated with this field mixes with the SM Higgs or some SM sector Φ that has yet to be discovered. Two massive q_{v}, a valley up and valley down quark, are present and hadronize like their SM counterparts. They carry a $U(1)$ charge and the lightest v-hadrons they can form are an isospin triplet of π_{v} analogous to the SM pions. The valley-neutral π_{v} decays to SM particles via the Φ_v, neutral in both sectors, which mixes with the SM Φ. The SM Φ possesses a Yukawa coupling to SM fermions and so decays preferentially to heavy fermions.

The exact nature of the decays and particles within the hidden sector are actually not the focus of this search. They are merely one mechanism by which long lived neutral particles may be produced and decay to the SM. A more generic toy model can simply consider some SM scalar Φ decaying to a pair of scalars or pseudoscalars s, as in Figure 1.1, with the details at the vertex taken to be unimportant. Here the s is the long lived particle, invisible to the SM, which decays to SM fermions. Due to the Yukawa coupling with the Φ the decays will primarily be to kinematically accessible heavy quarks.

Due to the lifetime of the s, the signature resulting from their production by a collision in a particle detector will consist of a spray of particles (from the hadronization of the SM fermions) seemingly detached - that is, displaced - from the collision point of the protons. Detectors and their standard software are developed based on searches for and measurements of more familiar signatures associated with SM decays and will not be tuned to such a signature. Dedicated searches for displaced signatures are therefore necessary to detect such decays resulting from a hidden sector or any similar phenomena giving rise to LLPs.

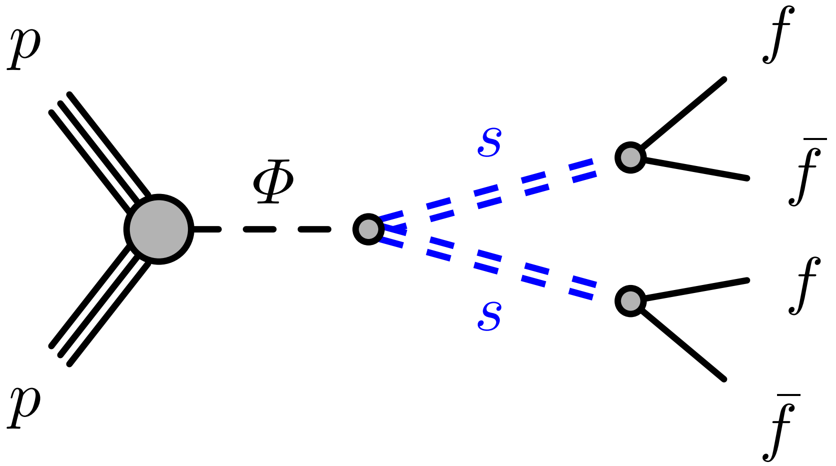

Figure 1.1: A diagram illustrating the type of decays considered in this analysis. A scalar Φ decays to two long lived particles s which in turn decays to pairs of SM fermions.

1.3 Proton Proton Collisions

The evolution of particle states when two protons collide at high energies needs to be understood in order to predict the final states that result. A description of both hard and soft processes is necessary in order to accurately understand and simulate collisions. This section describes briefly the theory of proton-proton collisions and gives an overview of the terminology used to describe the resulting event.

1.3.1 The Hard Scatter

An interesting high energy collision of protons is actually a collision of partons - the scattering is one of parton states. In the initial state each incoming proton is composed of a sea of gluons and quark-antiquark pairs in addition to the three valence quarks. The majority of a proton's energy is generally occupied by particles within this sea of gluons, while the valence quarks share the remainder. The internal energy distribution is described by a parton distribution function (PDF). This distribution must be determined non-perturbatively due to the low internal energies.

A PDF gives the probability density for a parton to carry a some fraction x of the parton's total momentum at a given squared energy scale Q^2 determined by the expected momentum transfer. Deep inelastic lepton-hadron scattering experiments and hadron-hadron collision experiments are performed to determine each PDF's dependence on x. Results must be extrapolated to higher and lower Q^2 and this, combined with the original uncertainties from the scattering experiments, explains why no universal PDF has been developed. Instead, several are available and an overall systematic uncertainty is included in analyses due to the uncertainty in the PDFs.

Figure 1.2 shows an example of the PDF produced by the MSTW collaboration, MSTW 2008. The function $f(x, Q^2)$ gives the probability of finding a parton of the chosen flavor containing a fraction x of the proton's total energy at the energy scale Q. The PDFs are parameterized as $xf(x, Q^2)$ as a function of x. Note the tendency for a high momentum parton to be a quark, particularly a light quark. Collisions between pairs of gluons thus tend to be softer overall than the collisions between pairs of quarks.

To determine hadronic cross-sections the PDFs are convoluted with parton cross-sections, quantities indicating the relative probability of each possible physics process to occur. The phrase *physics process* refers to the production of any of the possible final states from the given initial state interaction. The total proton-proton cross-section, at an 8 TeV center of mass energy, is 102 mb. This is the sum of the cross-sections for each possible final state resulting from the proton-proton collision. The plurality is taken by the relatively-uninteresting elastic scattering of the protons. The most sought after collisions involve two high energy partons and are responsible for only a small fraction of the total cross-section.

The hard scatter itself generally involves only two partons and can be treated perturbatively, at least initially. A scattering event cannot result in a free parton due to the confining nature of QCD. As one colored particle separates from the others in its proton the energy of the gluon field increases, producing pairs of quarks or gluons from the vacuum. This causes

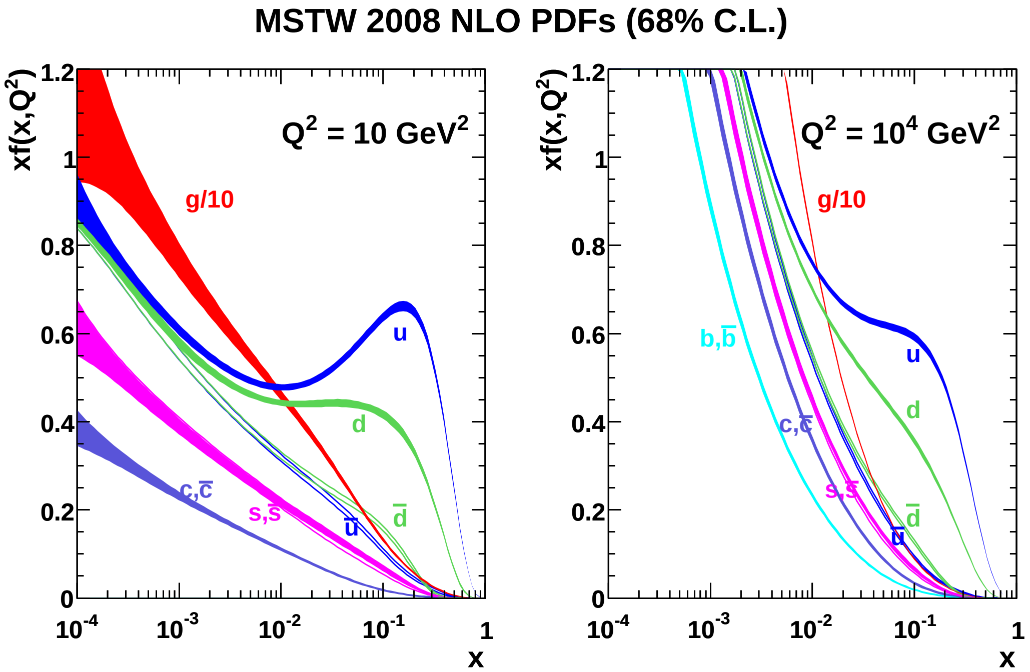

Figure 1.2: The MSTW 2008 proton parton distributions at two energy scales [1].

a chain reaction of pair production until hadronization, the full confinement of all final state quarks into color-neutral states, has occurred. The result is several hadrons collimated along the direction of the initial parton's momentum. The initial stages of jet formation can be described perturbatively until the average energies become too low. Jets will be described in more detail in Section 3.3.

1.3.2 The Underlying Event and Pile-up

Correctly modeling what happens during a collision in a detector does not stop with modeling the hard scatter. Additional contributions to the environment surrounding the hard scatter include the beam remnant, initial state radiation (ISR), and pile-up.

The underlying event (UE) refers to everything that occurs as a result of the collision that is not the result of the hard scatter. While the hard-scatter of two protons involves the scattering event of two partons, remnants of the protons also participate in the event. The exchange of momentum and change in the valence parton state result in the disintegration of the proton and hadronization of the remaining partons. Almost all of the momentum of these particles is usually parallel to the trajectory of the colliding protons and so generally avoids the limited fiducial region of a particle detector.

Initial state radiation, another component of the UE, may have a greater impact on the event's final state. ISR is the result of an incoming parton radiating a gluon which will hadronize and form a soft (low energy) jet or a soft contribution to the jets resulting form the hard scatter. Final state radiation (FSR) analogous to ISR but for outgoing partons, can have a similar effect. Inaccurate modeling of ISR and FSR is important in general, but in events with decaying neutral LLPs it may impact the frequency at which a neutral LLP decay is interpreted, in terms of the signature it produces, as being the likely result of SM interactions only.

While the hard-scatter and UE refer to the interactions involving a solitary pair of protons, such an event is relatively unlikely in modern colliders which collide protons in groups called bunches to maximize the probability of a hard-scatter occurring. Pile-up refers to multiple parton-parton interactions in the same event which are the result of separate proton collisions. The cross-section for interesting hard-scatter events is much smaller than that for less interesting, low energy "glancing blows" between partons. As a result, there is typically one *primary vertex* or PV where a hard-scatter took place and several less interesting *secondary vertices* which are the pile-up vertices. Technically, these extra collision are in-time pile-up. Out-of-time pile-up are measurements resulting from a different collision which are incorporated into the current event. Both in-time and out-of-time pile-up will alter the final state of an event and may result in a signature from the hard-scatter that is consistent with a LLP decay being instead interpreted as likely belonging to a purely SM event.

The impact of pile-up on this search, and of the correct modeling of ISR and pile-up, will be discussed in Section 5.4.

Chapter 2

EXPERIMENTAL APPARATUS

The ATLAS (A Toroidal LHC ApparatuS) detector is a general purpose detector build to study collisions provided by the the Large Hadron Collider (LHC). ATLAS is composed of several layers of subdetectors which will each be detailed. Special attention will be paid to the electromagnetic and hadronic calorimeters (the ECal and HCal), which are of primary importance to this search.

2.1 The CERN Accelerator Complex

At 27 km in circumference the Large Hadron Collider [27] is the world's largest particle collider. Buried about 100 m underground near the city of Geneva and under the European Center for Nuclear Research (CERN), the collider is designed to collide hadrons at a max center of mass (CM) energy of 14 TeV, 7 TeV per beam, with a luminosity of 10^{34} cm^{-2}s^{-2}.

The protons collided by the LHC start their journey as the nuclei of hydrogen atoms, each ionized using a duoplasmaton, and are accelerated by an electric field to 94 keV. The duoplasmaton consists of a cathode emitting electrons into a vacuum chamber into which a gas, in this case hydrogen, is introduced. The gas becomes ionized upon interacting with the electrons, forming a plasma. Charged grids accelerate the plasma into a beam which is ejected from an aperture of the device.

The protons are not fed directly into the LHC and are instead accelerated to higher energies in several stages through the CERN Accelerator Complex before their injection into the collider. The stages of the CERN accelerator complex are displayed in Figure 2.1. The 94 keV protons are injected into LINAC (LINear particle ACcelerator), where their energy is increased by over a factor of 50 to 50 MeV. The protons are then passed to the circular

Proton Synchrotron Booster (PSB) and accelerated to 1.4 GeV, when they are passed on to the Proton Synchrotron (PS) to be accelerated to 25 GeV. The penultimate injection is into the Super Proton Synchrotron (SPS), where the protons are accelerated to 450 GeV. Finally, the protons are injected as the counter rotating beams in the LHC ring and accelerated to their final energy. In 2012, the LHC operated with 4 TeV beams for an 8 TeV CM energy. In 2015, this was increased to 6.5 TeV beams for a 13 TeV CM energy.

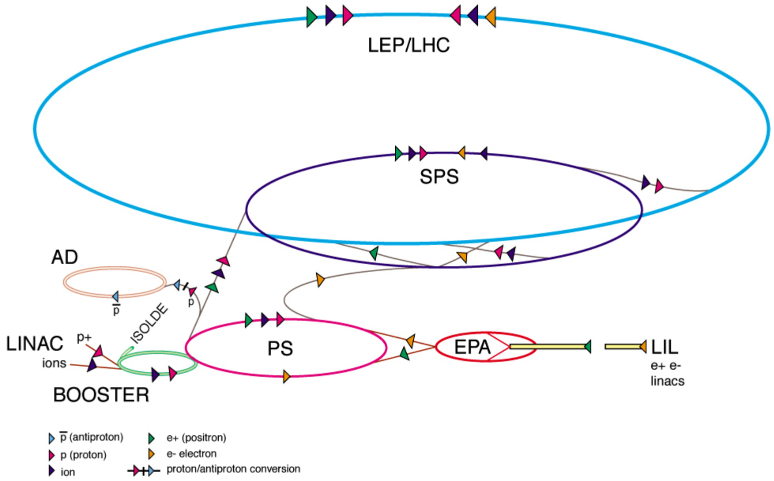

Figure 2.1: The CERN accelerator complex [2]. The linear particle accelerator injects protons into the Proton Synchroton Booster (PSB). Protons from the PSB are injected into the Proton Synchroton, and then into the Super Proton Synchrotorn. Finally, protons are injected into the LHC, the largest ring pictured. The acronym LEP refers to the Large Electron-Positron Collider, which proceeded the LHC. The rings labeled AD (Anti-proton Decelerator) and EPA (electron-position accumulator) are not a part of the LHC experiment but are used by other experiments.

The LHC ring is composed of eight segments, each containing a straight section as well as a curved section along which a portion of the 1232 LHC superconducting magnets bend the beam, as shown in Figure 2.2. The straight sections are 528 m in length and identified by their midpoints, Point 1 through Point 8, with beam injection near Point 1. Beam acceleration is achieved via the Radio Frequency (RF) cavities located at Point 4. RF cavities contain an oscillating electromagnetic field at a frequency such that protons of the desired velocity experience no force while traversing the cavity but all other protons are accelerated by the field to bring them to the desired energy. At Points 3 and 7 collimators focus and shape the beam. Collisions occur at Points 1, 2, 5, and 8, where the detectors ATLAS, ALICE, CMS, and LHCb are respectively located. Finally at Point 6, when the protons beams have lost a sufficient amount of particles they are dumped, i.e. directed toward a graphite target, in order to remove them from the collider.

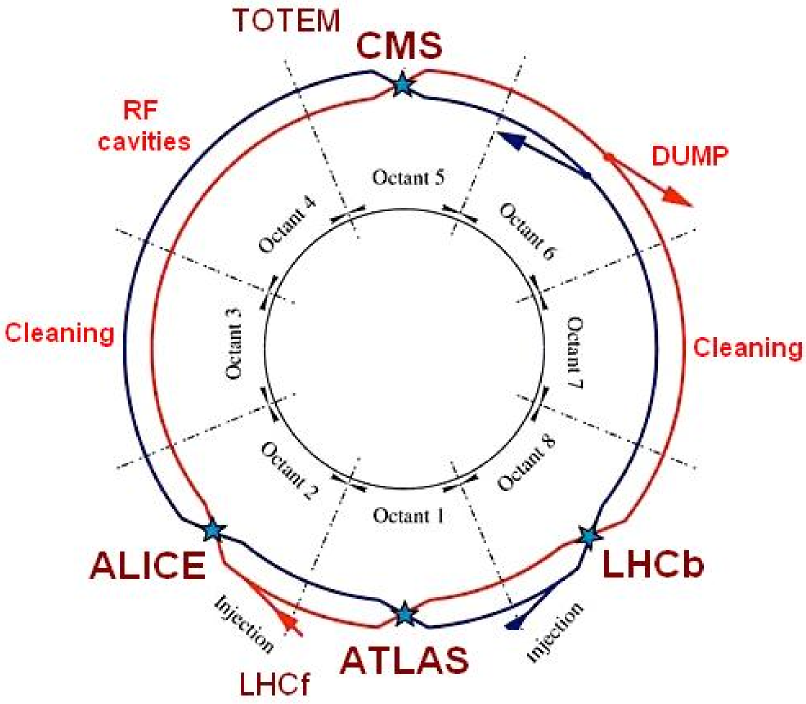

Figure 2.2: The large hadron collider [3]. The primary function of each octant is labeled, included the location of the RF cavities that separate the protons into bunches. Blue stars mark the location where the proton beams are crossed, producing proton collisions for the LHC detectors built around the collision point. The red and blue lines mark the antiparallel paths of the two proton beams in the detector.

Protons do not circulate the LHC in a continuous stream. Instead, protons are separated into bunches of $\sim 10^{11}$ protons each. The RF cavities have an operating frequency of about $\sim 400\ MHz$, corresponding to about 35640 potential wells in the RF field, called buckets. The LHC is optimized for a 25 ns separation between proton bunches, while the bucket separation is about 2.5 ns. This corresponds to a maximum of 3564 proton bunches per beam. The proton beams' buckets are filled in stages from the injections of the upstream accelerators, necessitating injection gaps in the bunch pattern in which no protons are present. Furthermore, the bunch pattern will include abort gaps - long trains of unfilled bunches needed to cleanly dump the beam. The "kicker" magnet responsible for diverting the beam into the graphite target requires ~ 3 μs to reach full field strength. The abort gap is needed because protons dumped early would be thrown into the superconducting magnets or the detectors rather than the target. The inclusion of injection and abort gaps results in only 2808 potential proton bunches out of the 3564 potential bunches when operating with 25 ns bunch spacing. In 2012, the LHC used 50 ns bunch spacing and 1380 bunches per beam.

Bunch crossings (BCs) nominally refer to the crossing of opposite sense proton bunches in ATLAS. However, deliberately unfilled bunches are interspersed with filled ones to create BCs in which only one, or neither, "bunch" actually contains protons. This is done in part to allow for the study of backgrounds resulting from a source other than the collision. The bunch crossings (BCs) relevant to this analysis are:

- Filled BCs: Both buckets are filled with protons

- Empty BCs: Both buckets contain no protons and 5 buckets on either side of the BC are also unfilled

- Unpaired Isolated BCs: One bucket is filled while the other is unfilled, and the unfilled bucket is also surrounded by at least 3 unfilled buckets on each side.

The requirements for additional unfilled buckets for a BC to be officially Empty or an Unpaired Isolated BC serve to isolate the unfilled bucket participating in the crossing from protons leaking from filled buckets into unfilled ones. Empty BCs are used for the study of non-collision non-beam backgrounds, while Unpaired Isolated BCs are of interest for the study of beam-induced non-collision backgrounds.

2.2 Luminosity and pile-up

Each bunch contains $\sim 10^{11}$ protons upon entering the LHC, is several centimeters long in the longitudinal direction, and only about 1 mm wide in the transverse direction. These bunches are squeezed using quadrupole magnets at the points of collision to increase the proton density with respect to the collisional cross-section, β^*. The goal is to increase the probability of collisions and thus the integrated luminosity, $\mathcal{L}$, delivered to the detector. Higher integrated luminosity indicates a larger number of scattering events, providing more data to physics analyses. In 2012 the peak luminosity was $8 * 10^{33}$ cm^{-2}s^{-2}. The integrated luminosity as a function of time throughout the 2012 and 2015 runs is shown in Figure 2.3.

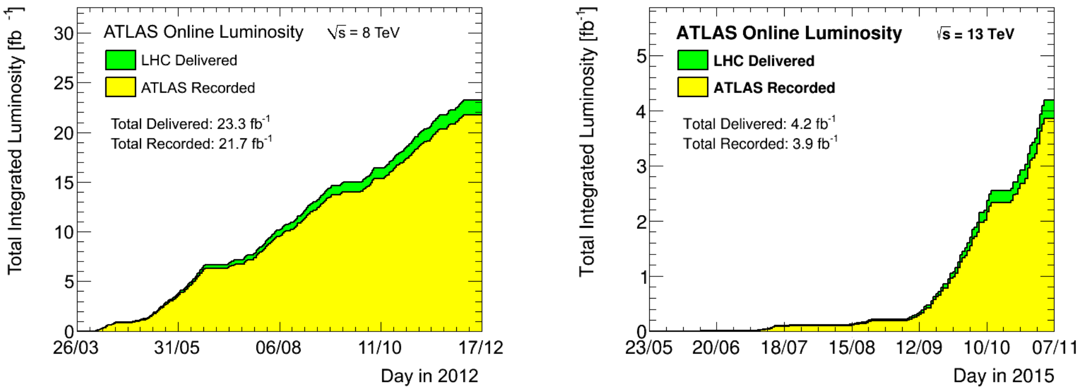

Figure 2.3: Integrated luminosity versus time in 2012 (left) [4] and 2015 (right) [5].

The number of expected events for a given process depends on the process cross-section (σ) and the integrated luminosity ($\mathcal{L}$):

$$N = \mathcal{L}\sigma \tag{2.1}$$

The cross-section depends on the center-of-mass energy and the particular particles involved in the full process, but the luminosity depends only on the beams. The parameters describing the beam are time-dependent the instantaneous luminosity is equal to

$$L = \frac{N_b^2 n_b f_r \gamma_r 4\pi \epsilon_n \beta *}{F} \tag{2.2}$$

Here N_b is the number of protons per bunch, n_b is the number of colliding bunches, and γ_r is the relativistic gamma factor, f_r is the collision frequency. The protons in the beam naturally repel one another, gaining transverse momentum and increasing the transverse width of the bunch. The beam is squeezed and shaped to minimize this effect. The normalized transverse beam emittance ϵ_n is a measure of the beam divergence in the xy plane. Finally F is a geometric factor accounting for the angle at which the beams are crossed at the interaction point.

A bunch-crossing frequently results in more than one proton-proton collision. Multiple collisions in a single BC is referred to as "in-time pile-up" due to the final states of multiple scattering events being incorporated into a single event. Detector elements may also record collisions from bunch-crossings preceding or following the current bunch-crossing if their response time is greater than the bunch separation. This phenomenon is refereed to as "out-of-time" pile-up. Pile-up increases jet and track multiplicity in events and may impact trigger and analysis efficiencies. It naturally depends on luminosity and averaged around 15 collisions per event in both 2012 and 2015.

2.3 The ATLAS Detector

While the LHC provides the hardware to accelerate and collide protons beams it is the several detectors spread along the ring which provide the hardware and software to analyze the resulting collisions. Any detector is built as a balance between the optimal design for its intended scientific purpose and the available materials, funding, and physical limitations. The ATLAS detector [6] was designed as a multi-purpose detector intended to give as complete as possible a picture of the production and decay of particles resulting from proton collisions, thus allowing it to be used both for precision measurements and for searches for new physics. The detector was therefore designed to have precise measurements of both the momentum and energy of a variety of particles within a large volume.

ATLAS, shown in Figure 2.4, is barrel shaped and oriented with its axis of radial symmetry along the beampipe. The long, cylindrical middle portion is properly called the “barrel” and end portions on either side, disc-shaped to cover as much area as possible perpendicular to the beampipe, are termed the “endcaps”. ATLAS contains three subdetectors designed for different measurements: from the beampipe outwards they are the inner detector, the calorimeters, and the muon spectrometer. Each of these subdetetors is also composed of several subsystems. The calorimeters, for example, consist of an inner electromagnetic calorimeter and an outer hadronic calorimeter. Data recorded by the inner detector is used to reconstruct tracks from charged particles passing through it, allowing for the determination of the particle’s charge and momentum. The calorimeters measure the energy deposited by both the charged and neutral particles it stops. Finally, the muon spectrometer provides tracking for particles, primarily muons, that escape the calorimetry. ATLAS additionally has a magnet system providing a 2 T solenoidal magnetic field within the inner detector and a 0.5 T toroidal magnetic field within the muon spectrometer. These magnetic fields bend the trajectory of charged particles passing through them, allowing for the measurements of momenta and charge. Figure 2.5 shows the typical interactions of a variety of particles with the subsystems of ATLAS.

ATLAS uses a right-handed cylindrical coordinate system. In Cartesian coordinates, the z-axis runs along the beam pipe, the x-axis points towards the center of the LHC ring, and the y-axis points skywards. The azimuthal angle is represented by ϕ, while the polar angle θ is usually replaced by the pseudorapidity η for convenience. η is defined as

$$\eta = -\ln(\tan(\frac{\theta}{2})) \tag{2.3}$$

Compare this to the true rapidity y, itself defined as

$$y = \frac{1}{2}\ln(\frac{E+p}{E-p}) \tag{2.4}$$

Rapidity is invariant under boosts in the z direction, while only differences in pseudorapidity are similarly invariant. However, as the mass of a particle approaches zero the two quantities converge.

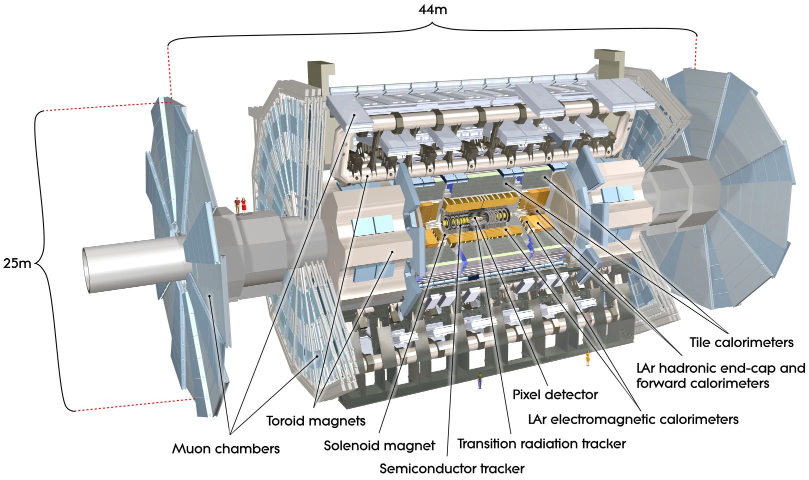

Figure 2.4: A cutaway of the ATLAS detector with each subsytem labeled [6].

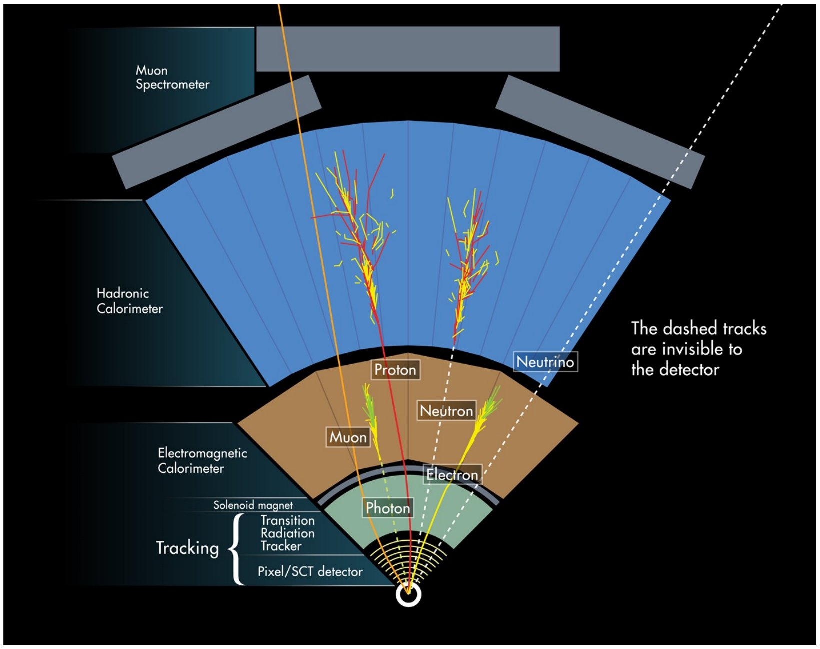

Figure 2.5: The interactions of several common particles with the ATLAS detector [7].

A measurement frequently used in analyses as a measure of the closeness of two particles or objects is ΔR, defined as:

$$\Delta R = \sqrt{\Delta\eta^2 + \Delta\phi^2} \tag{2.5}$$

While R is generally taken as:

$$R = \sqrt{x^2 + y^2} \tag{2.6}$$

2.3.1 The Inner Detector

The Inner Detector (ID), shown in Figure 2.6 is designed to detect the passage of charged particles in order to determine their momentum and charge. It is comprised of concentric layers of detecting material and has a total radius R of 1.2 m and length in z of 6.2 m. This corresponds to a pseudorapidity region of $|\eta| < 2.5$, beyond which particle detection must rely solely on the calorimeters and muon spectrometer. Three subsystems with different detector technologies form the ID: the pixel detector, lying closest to the beampipe, followed by the semi-conductor tracker (SCT), and the transition radiation tracker (TRT). Figure 2.7 shows a cross-section of the ID with distances in R and z and several values of η labeled.

As the particles traverse the layers of the ID they interact with the active material, resulting in local ionization. The magnetic field in which the ID is immersed results in a bending of the path along which the charged particles travel, allowing for the determination of the sign of the charge and its momentum. By combining the locations in which these interactions occurred in a sort of sophisticated connect-the-dots, ATLAS software can reconstruct the path along which the particle passed. These tracks are also extrapolated back to the beampipe in order to determine the interaction point (IP), which is the location of the highest energy collision within the detector.

The pixel detector has the highest granularity of the three subsystems, appropriate given its location closest to the barrel where the charged particle density is at its highest. It is composed silicon (Si) sensors containing pixels $50\,\mu\text{m} \times 400\,\mu\text{m}$ ($\phi \times z$) in size which are arranged in three layers in both the barrel and endcap. The innermost barrel layer is located at $R = 51$ mm and the outermost at $R = 123$ mm, while on either end the first endcap disk

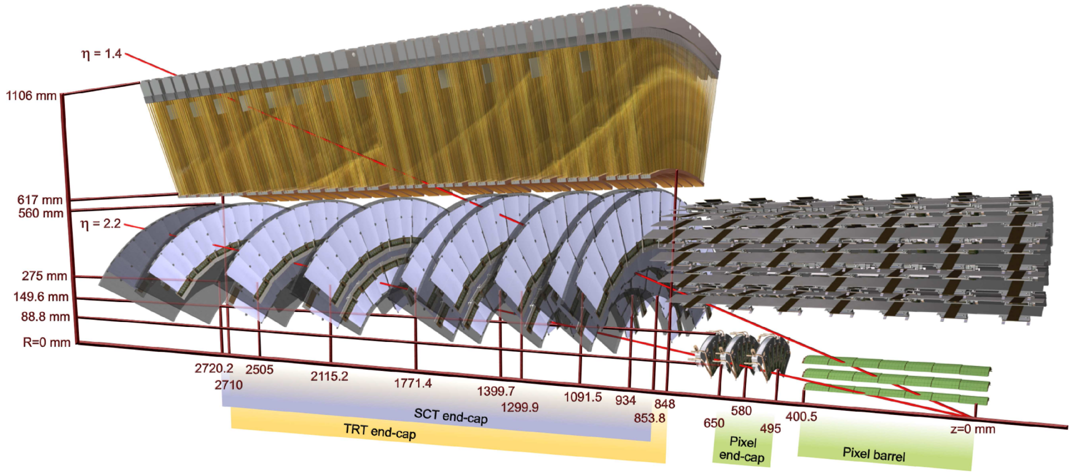

Figure 2.6: The Inner Detector of ATLAS [6].

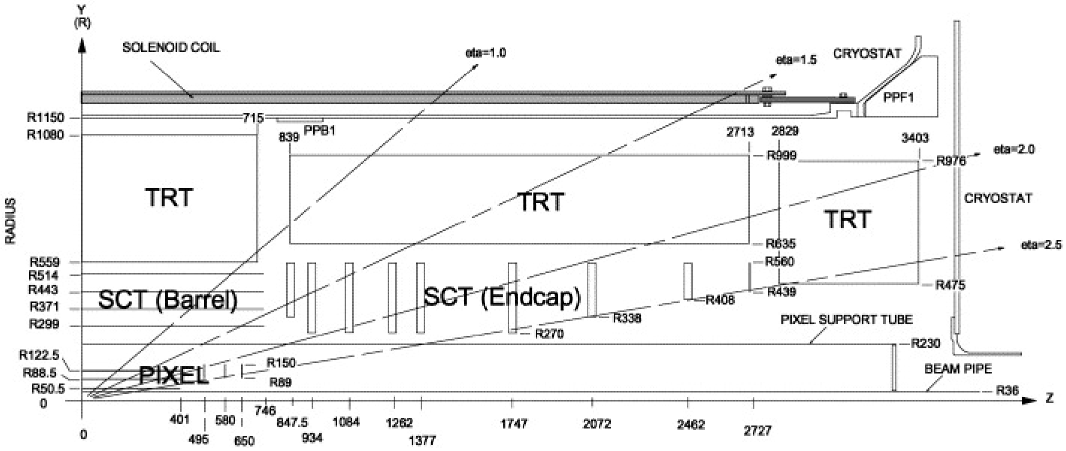

Figure 2.7: A cross-section of the Inner Detector with relevant distances and angles labeled [6].

is located at $|z| = 495$ mm and the last at $|z| = 650$ mm. A typical particle will traverse all three pixel layers. The resolution in the barrel is ~10 µm in $(R - \phi)$ and 115 µm in z, while in the endcap the radial resolution is 115 µm while the $(R - \phi)$ resolution is 10 µm.

The SCT is composed of modules containing microstrip sensors made from silicon wafers, each 120 mm long and 60 mm wide. The modules are arranged in four layers (300 mm < R < 510 mm) in the barrel and nine (850 mm < z < 2730 mm) in each endcap. There are strip planes per module, glued back to back and offset by 40 mrad as shown in Figure 2.8, with the inner strip aligned along z in the case of the barrel and radially in the case of the endcaps. The offset allows for a more accurate position measurement of the location of hits in the detector. A single strip can only indicate the transverse location of a hit, yielding R and ϕ coordinates in the barrel, for example. The 40 mrad stereo angle allows for the determination of the longitudinal coordinate, z for the barrel example. A typical particle will pass through all four layers in the barrel, yielding four space points for track reconstruction. The resolution is $17\,\mu\text{m}$ in $\text{R}-\phi$ in the barrel and endcaps and $580\,\mu\text{m}$ in z (barrel) and R (endcaps).

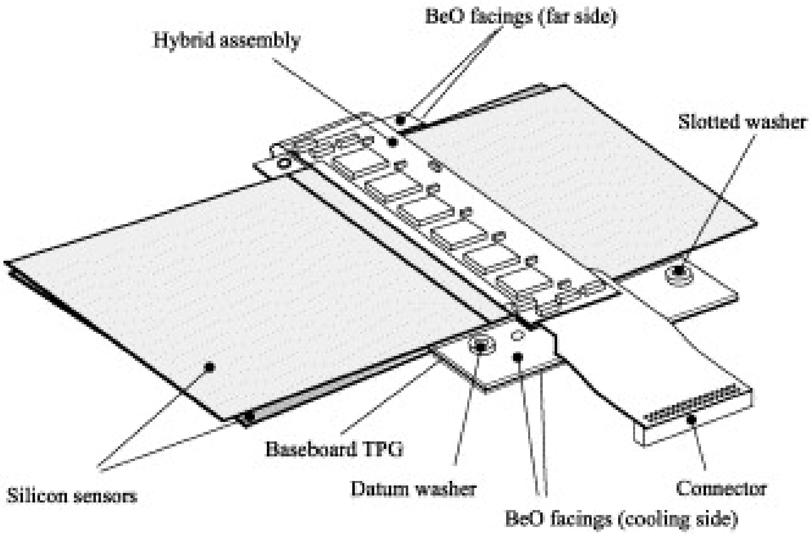

Figure 2.8: An SCT module [6]. The two strips are glued with a 40 mrad offset to allow for the determination of full 3D spacepoints.

The TRT is the outermost subsystem of the ID and the largest by volume. The 4 mm diameter straw tubes that compose the TRT are filled with a xenon-based gas and contain a central gold-plated tungsten-rhenium wire held at 1.56 kV which collects the electrons produced when a charged particle ionizes the gas in the tube. Highly relativistic charged particles crossing the boundary between mediums with different dielectric constants produce transition radiation. To aid in particle identification, polypropylene fibers (barrel) and foil (endcaps) are interleaved with the tubes to initiate the production of transition radiation by low-mass particles. The pulse collected by the central wire is therefore larger in the case of low-mass particles, aiding in differentiating light particles such as electrons from hadrons such as pions. The barrel consists of 73 layers of 71 cm tubes parallel to the beampipe in the barrel, and 160 planes of 37 cm tubes arranged radially in the endcap. Position information is poor along the length of the tubes, so each tube provides hit information in two dimensions only with a $R-\phi$ and $R-z$ resolution of about 130 μm per straw in the barrel and endcap, respectively. Generally a particle traversing the TRT will not leave a hit in each layer - the average is $\sim$ 30 hits per track.

2.3.2 The Calorimeters

The ATLAS calorimetry, Fig 2.9, consists of an inner electromagnetic calorimeter (ECal) and an outer hadronic calorimeter (HCal). Together they cover the pseudorapidity range $|\eta| < 4.5$. Coverage in η is important for reconstructing properly the presence of particles, such as muons and neutrinos, that escape the calorimeters without being stopped. The ECal covers $|\eta| < 1.475$ in the barrel and $1.375 < |\eta| < 3.2$ in the endcaps. The HCal covers $|\eta| < 1.7$ in the barrel, and $1.5 < |\eta| < 3.2$ in the endcaps. The calorimeters measure the energy of charged and neutral particles via a series of interactions which produce a cascade of particles that are then absorbed by dense materials. Complete absorption of the cascade allows the energy of the initiating particle to be determined. Both the ECal and the HCal are sampling calorimeters: alternating layers of an active medium which measures energy and a dense absorbing material which initiates showers interact with and eventually stop incident particles. As a result of the necessary interactions with the absorber, not all of a particle's energy is absorbed by the active material. Careful calibration is needed to correct the initial energy measurements. The ECal specializes in measuring the energy of particles which interact via the electromagnetic force, especially electrons and photons. Incident particles lose energy via bremsstrahlung and interactions with the material via pair production and other QED processes to produce photons and additional electrons in a series of interactions.

The HCal specializes in measuring the energy of incident hadrons, which produce pions and other particles upon interacting with nuclei via the strong force. These particles decay and their decay products, electrons and photons, are absorbed.

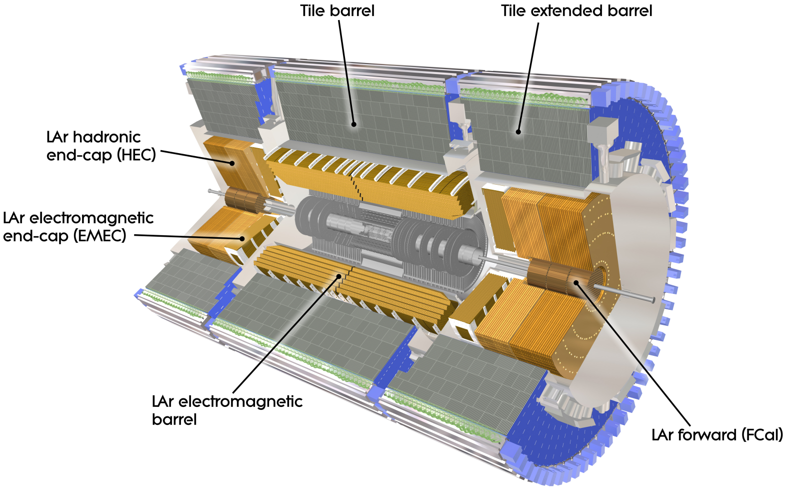

Figure 2.9: The ATLAS calorimeters [6].

The electromagnetic calorimeter uses lead absorbers and liquid Argon (LAr) as the active medium. The incoming particles interact with the lead, producing secondary particles. Interaction of the secondary particles with the argon results in the ionization of the argon. Electrons freed by the ionization are drawn to and collected by electrodes, which are kept at high (about 2 kV) voltage, on the lead surface. The layers are arranged in an accordion geometry, as shown in Figure 2.10, preventing coverage gaps in ϕ that would otherwise be present due to the space required by the readout electronics. The ECal covers up to $|\eta| < 3.2$. The barrel is composed of two half-barrels, one for $z > 0$ and one for $z < 0$, with inner radii of 2.8 m and outer radii of 4 m. The portion of this region covered by tracking ($|\eta| < 2.5$) includes three ECal layers, with the innermost layer finely segmented to allow for precise position and pointing measurements of the incident particle. This innermost layer has a granularity of 0.003×0.1 ($\Delta\eta \times \Delta\phi$), while the granularity of the middle layers is

0.025×0.025 and the outer layer is 0.050×0.025. The $|\eta|$ region outside of the tracking coverage ($|\eta < 2.5$) is covered only by these coarser middle and outer layers. The middle layer has the greatest depth and is responsible for collecting most of the shower. The endcap consists of one wheel on either side of the barrel, with internal and external radii of 0.3 m and 2.1 m respectively. A presampler is placed in the transition region between the barrel and endcap ($1.5 < |\eta| < 1.8$) to improve the energy measurement by identifying showers initiated in material before the calorimeter.

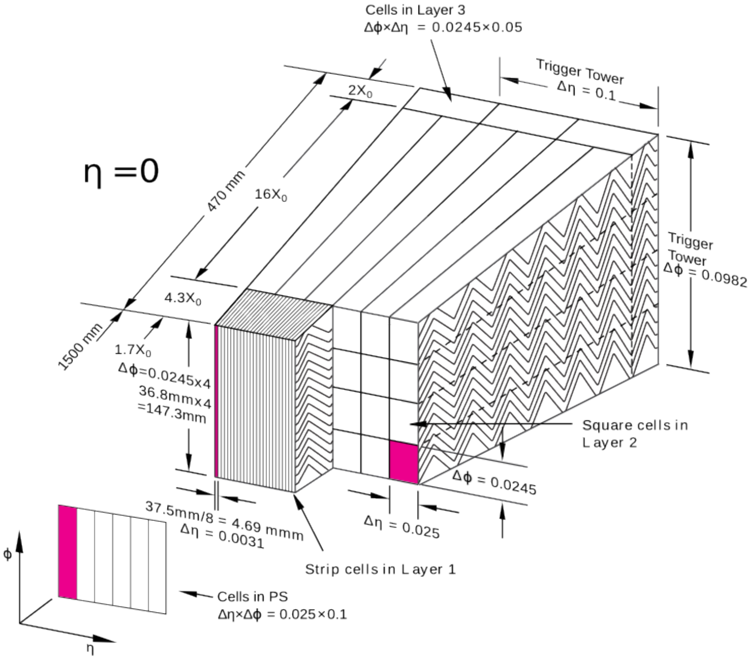

Figure 2.10: The structure of the electromagnetic calorimeter of ATLAS [6]. The shaded pink regions indicates the spatial extent of a single cell, one in the inner layer and one in the other layer.

The radiation length X_0 of a particle is the distance in some medium over which the particle loses 1/e of its energy via electromagnetic interactions. Prior to interacting with the calorimetry particles will have already lost some energy in the material they have already traversed. Figure 2.11 shows the thickness of material, as measured by X_0, for the ECal. For the region $|\eta| < 1.8$ a thin layer called the presampler precedes the main layers to improve the energy resolution, allowing for a more accurate energy measurement for particles which have lost a significant portion of their total energy in material preceding the calorimeter. The preceding material has a radiation depth of 2-6 radiation lengths for electrons and photons. By contrast, the depth of the ECal ranges between 22 and 33 radiation lengths. The lower end of the range corresponds to the transition region, the region between the barrel and endcap covering $1.37 < |\eta| < 1.52$, which also includes more inactive material than other sections of the ECal.

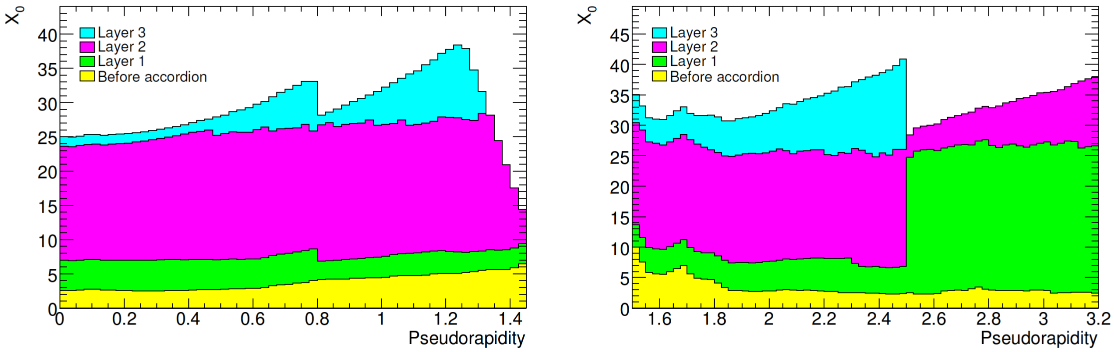

(a) Barrel

(b) Endcap

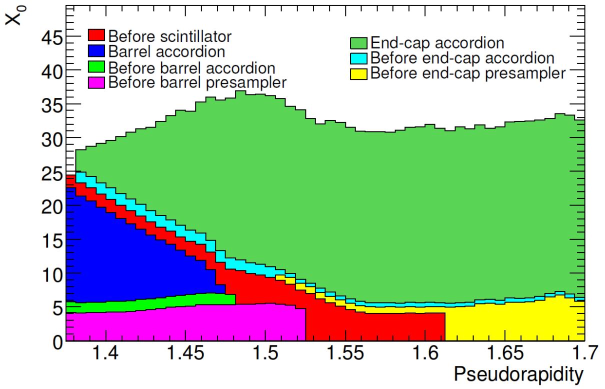

(c) Crack Region

Figure 2.11: The cumulative depth as measured by the radiation length, X_0, of the electromagnetic calorimeter [6].

The average energy resolution in the ECal is

$$\frac{\sigma_E}{E} = \frac{10\%}{\sqrt{E[GeV]}} \tag{2.7}$$

ECal cell time resolution is ~ 0.1 ns. While accurate energy measurements are needed to properly reconstruct a collision event accurate timing aids in discriminating between possible signal and certain types of background events.

Hadrons, even neutral hadrons, will also interact with material in the ECal, but the parameter of interest is the nuclear interaction length λ rather than the radiation length. The nuclear interaction length of a hadron is the mean distance the particle will travel before undergoing an inelastic interaction with a nucleus in the surrounding medium. The ATLAS ECal has a nulclear interaction length of ~ 2.3. Hadronic showers will therefore typically begin in the ECal and intensify in the HCal. The depth of the calorimetry in terms of the interaction length is displayed in Figure 2.12.

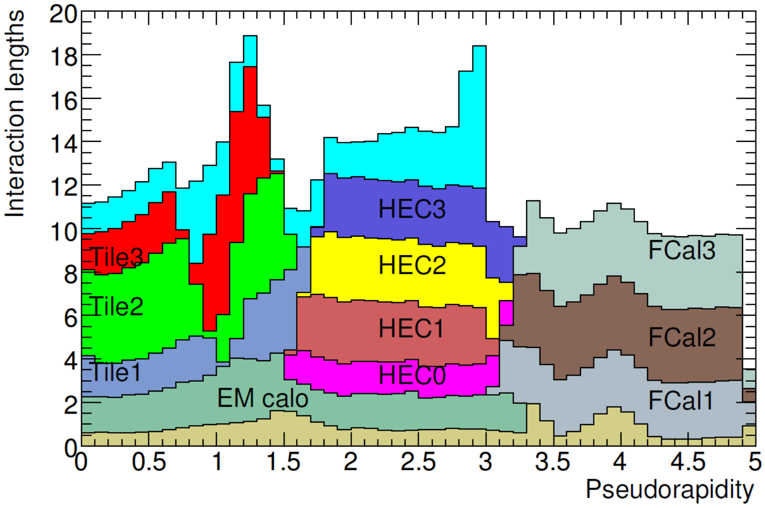

Figure 2.12: The depth of each layer of the ATLAS calorimetery as measured by the interaction length λ [6].

The hadronic calorimeter has poorer position resolution than the ECal, typical of hadronic calorimeters intended to be paired with electromagnetic calorimeters. Hadrons generally require a greater depth of material to be fully stopped and absorbed than do charged leptons such as electrons, in other words $\lambda_{\text{hadron}} > X_{0\text{lepton}}$ is generally true. The HCal barrel, also called the "tile calorimeter" or "tilecal" uses scintillator tiles as the active medium interleaved with an iron absorber. The endcaps use copper as an absorber and LAr as the active material and share the EM endcap cryostats. The barrel covers $|\eta| < 1.7$ while the endcaps cover $1.5 < |\eta| < 3.2$.

The barrel is segmented into three sections, a 5.8 m long central section (covering $|\eta| < 0.8$) with two sections flanking it which are each 2.6 m in length and called the "extended" barrels (covering $0.8 < |\eta| < 1.7$). Each wheel has an inner radius of 2.28 m and an outer radius of 4.25 m. Trapezoidal shaped iron and scintillator tiles are layered plane perpendicular to the beam axis and are stacked in wedge-shaped modules. Each tile spans the full module width in *phi*. A diagram of a barrel module is shown in Figure 2.13. In each of the three barrel sections total of 64 modules, with a single module covering $\phi \sim 0.1$, are arranged radially around the beam axis to achieve full ϕ coverage.

Tiles are grouped into cells each spanning a portion of the length in z and several stacks of tiles in the radial direction. The arrangement of the cells in the modules of the tilecal is shown in Figure 2.14. Light produced by each of the scintillators in a cell is transported by wavelength shifting optical fibers to a single photomultiplier tube (PMT). There are a total of three layers of cells per module, with the thickest layer being the central layer. The granularity of the inner and middle layers is 0.1×0.1 ($\Delta\eta \times \Delta\phi$), while the outer layer has a coarser granularity of 0.2×0.1 ($\Delta\eta \times \Delta\phi$).

The HCal endcap consists of copper plates stacked plane parallel along z with LAr between. The endcaps are segmented into two wheels each, each wheel containing 32 wedge-shaped modules. A single module contains two cell layers stacked longitudinally rather than radially as they are in the barrel. For $1.5 < |\eta| < 2.5$ the endcap has a granularity of 0.1×0.1 ($\Delta\eta \times \Delta\phi$), while for $2.5 < |\eta| < 3.2$ the granularity is a coarser 0.2×0.2 ($\Delta\eta \times \Delta\phi$).

Additional modules are installed in the transition region between the barrel and endcap, which includes a variety of inactive material such as the cryostat walls. These modules are

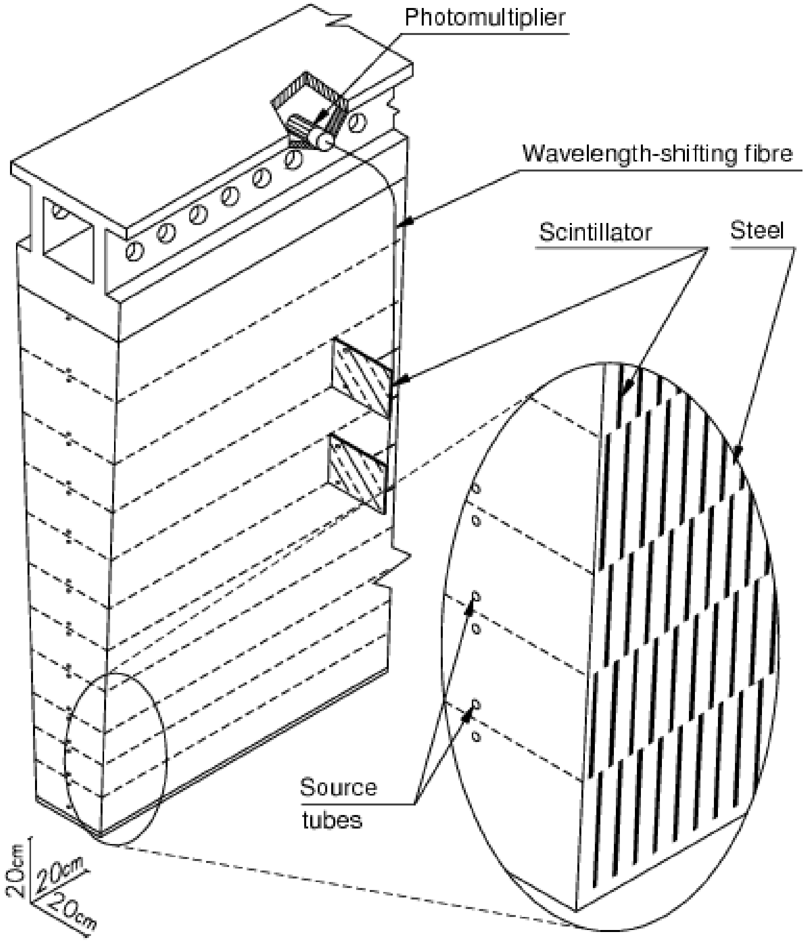

Figure 2.13: A diagram of a module of the hadronic calorimeter [6].

intended to recover energy lost to the inactive material and somewhat improve the poor energy resolution in this region. The combined HCal and ECal have a depth of $\sim$ 11 interaction lengths at $|\eta| = 0$ and posses an average energy resolution of about $\sigma_E/E = 50\%/\sqrt{E[GeV]}$. The timing resolution of the HCal cells is ~ 1 ns.

Three additional layers of calorimetry, called the forward calorimeter or FCal, are intended to extend the coverage in η as far as possible ($3.1 < |\eta| < 4.9$). The innermost layer is composed of copper and liquid argon, while the middle and outer layers use tungsten and argon. The inner layer is designed to extend EM calorimetry while the outer layers extend

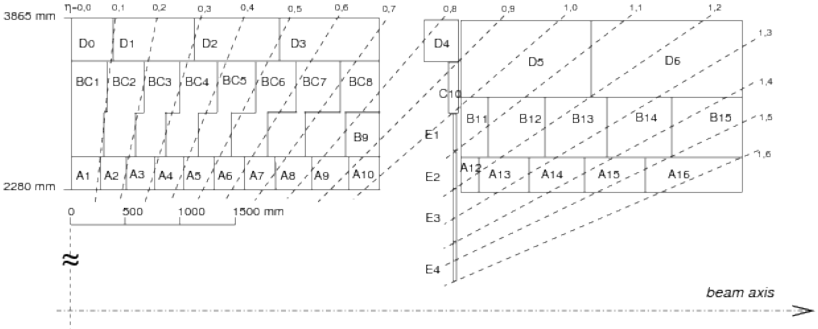

Figure 2.14: The arrangement of cells in a central barrel module (left) and an extended barrel module (right) in the hadronic calorimeter [6].

hadronic calorimetry. They add a depth of 7 to 9 interaction lengths in the forward region but have an energy resolution of $\sigma_E/E = 100\%/\sqrt{E[GeV]}$.

2.3.3 The Muon Spectrometer

Muons exhibit much greater penetration of material than other charged particles generated by collisions and resulting decays. They do not interact via the strong force, they radiate bremsstrahlung far less than the much lighter electron, and are still light enough that they can travel some distance before decaying. Their proper detection and the measurement of their momenta necessarily requires a dedicated detector. The outermost subsystem of ATLAS is dedicated to these particles. The muon spectrometer is designed for muon tracking and covers $|\eta| < 2.7$. To allow for momentum and charge determination the MS is immersed in a magnetic field provided by the toriod magnets around which it is built. The MS subdetector is itself composed of four different subsytems. The Monitored Drift Tube chambers (MDTs) and Cathod Strip Chambers (CSCs) provide tracking information while Resistive Plate Chambers (RPCs) and Thin Gap Chambers (TGCs) provide triggering. Figure 2.15 shows the transverse geometry of the MS while Figure 2.16 shows the geometry in the $R-z$ plane.

The MDTs form the bulk of the MS. Over 350,000 30 mm MDTs with lengths varying

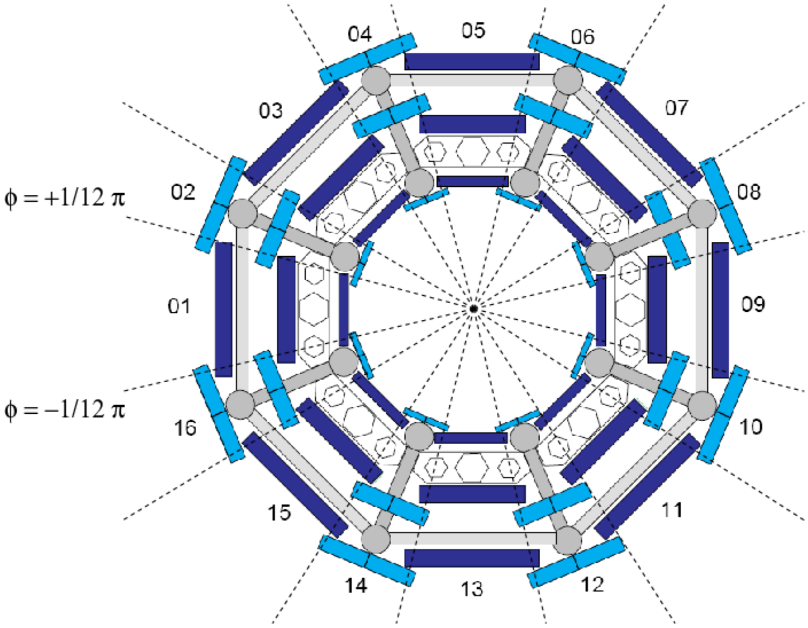

Figure 2.15: The geometry of the muon spectrometer in the transverse plane, sectioned in the barrel [6].

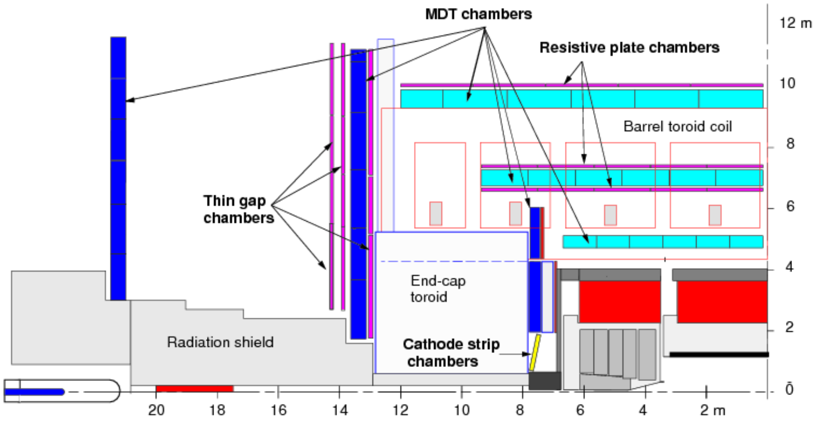

Figure 2.16: The geometry of the muon spectrometer in the $R - z$ plane [6].

between 1.8 m and 5.1 m are arranged in several layers around the calorimetry. They cover $|\eta| < 2.7$, except for the innermost endcap layer which possess a coverage of only $|\eta| < 2.0$. In the barrel the MDTs are arranged into three concentric layers, called stations, at radii

$\sim 5\ m$, $\sim 7.5\ m$, and $\sim 10\ m$. Each station is divided into 16 sectors, alternating between small and large, composed of two MDT multilayers each containing three or four layers of MDTs. Larger sectors contain more MDTs and are located between the toroid coils while the small sectors are positioned adjacent to the coils. Small and large sectors overlap to insure full *phi* coverage. Muons passing through the magnetic field are bent along η - thus the MDTs are oriented perpendicular to the $z-$axis and to the radial direction, providing precision coordinates in the bending plane (η) but no useful information in ϕ. The endcaps are arranged in wheels located at $|z| \sim 7.4\ m$, $\sim 10.8\ m$, $\sim 14\ m$, $\sim 21.5\ m$.

Each MDT contains a tungsten-rhenium central wire anode held at 3 kV and contains a pressurized Ar/CO_2 gas mixture. Muons passing through the tubes ionize the gas and the resulting electrons are attracted to the wire. The drift time of the electrons to the wire depends on the distance between their production point and the wire. The drift circle is defined by the distance of closest approach (the drift radius) to the wire and series of drift circles are used to reconstruct tracks. The drift radius can be determined to within $\sim 80\ \mu$m. This corresponds to a resolution for the full chamber of about 40 μm in the bending plane (in contrast to around 5 mm in the transverse plane).

The MDTs are limited by their counting rate, which would be unacceptably high for the forward ($\eta| > 2.0$) region on the innermost endcap layer. To accommodate this high rate, CSCs are located at high η in the the inner layer of the endcap. They are multiwire proportional chambers with two cathodes on either side of a gas gap and a set of anode wires running through the middle of the gap. The cathode planes are segmented, one in η and one in ϕ, to provide accurate $\eta - \phi$ position measurements with a resolution of 60 μm per plane. Four gas gaps per CSC allow for four hits per track for muons passing through the CSCs.

The RPCs and TGCs provide triggering and precision coordinate measurements in the barrel and endcaps, respectively. In the barrel, the RPCs are located on either side of the middle station and on the inner surface of the outer station, covering $|\eta| < 1.05$. They are gaseous parallel-plate detectors between 22 mm and 35 mm wide. Their fast response time allows for triggering on muons while their small size provides the ϕ coordinate information the MDTs cannot resolve. In the endcaps, seven layers of TGCs, which perform well in a high event-rate environment, surround the middle MDT station. Three layers form the innermost chamber while two each compose the outer layers, covering $1.5 < |\eta| < 2.4$. Like the CSCs, the TGCs are multiwire proportional chambers. The η and ϕ coordinates are provided by the wires and cathode plates, respectively.

2.3.4 The Magnet System

The magnet system of ATLAS generate a magnetic field for the the ID (in the $R{-}\phi$ plane) and the MS (in the $R - z$ plane). Two different magnet subsystems are used: a superconducting solenoid magnet for the ID and air-core toroidal magnets for the MS. The solenoidal magnet is aligned on the beam axis and rests just inside the electromagnetic calorimeter, which acts as the return yoke for the magnet and shares its cryostat. It provides a 2 T magnetic field throughout the ID. The toroid magnets form eight coils arranged radially about the beam axis, one set each for the barrel and each endcap. The barrel toroid provides a $\sim 0.5\ T$ magnetic field while the endcaps toroid provide $\sim 1\ T$.

2.4 Luminosity Detectors

Measurements of luminosity are performed with two detectors: LUCID and the Beam Condition Monitor (BCM) [27]. These measurements are crucial for tracking pile-up and the integrated luminosity. An accurate luminosity measurement is needed to predict the expect number of events from any given physics process.

LUCID (LUminosity measurement using Cerenkov Integrating Detector) measures luminosity via Cerenkov radiation. It is located 10 cm from the beampipe at $z = \pm 17$ m. Twenty aluminum tubes, 1.5 m long with a 15 mm radius, are arranged around the beampipe and point toward the center of ATLAS. The tubes are filled with pressurized C_4F_10 gas, providing a Cerenkov threshold of 10 MeV for passing electrons. At the back of each aluminum tube is a photomultiplier tube to measure the Cerenkov light produced by electrons and other charged particles passing through the gas. When the intensity of Cerenkov light is above the

PMT threshold a hit is recorded.

The BCM is a safety mechanism in addition to a luminosity detector. If its measurements indicate that the beams might damage the detector it will send a beam dump request. Four BCM modules are positioned symmetrically around the interaction point at two stations. Stations are located at $z = \pm 1.84$ m and the modules are located only 5.5 cm from the beampipe. Two are placed in the horizontal plane and two in the verticle, with each pair measuring the luminosity independently. The BCM modules are contain diamond sensors with high sensitivity and response time. They distinguish between beam background such as BIB, which will hit one station and then the next, from particles resulting from beam-beam interactions, which result in particles arriving at the stations simultaneously.

2.4.1 The Trigger System

The frequency of bunch-crossings can reach as high as ~ 40 MHz. In contrast, the frequency at which ATLAS can record events is constrained by data storage space and event processing time to be a “mere” 200 Hz. Clearly, many events cannot be recorded. To complicate the matter, most collisions will result in interactions and final states which are not of any interest to most analyses. For example, elastic collisions are frequent but not useful in searching for new physics. It is therefore necessary to devise a means to capture as many interesting events as possible out of the roughly 10^{15} events occurring in ATLAS over the year.

The ATLAS trigger system [6] was designed to increase the concentration of interesting events by reducing the number recorded events to only those containing potentially interesting physics. It must make the decision to keep or reject an event quickly and is therefore not capable of performing a detailed analysis. To allow for some reconstruction of physics objects, the trigger system is applied in a chain of three stages. At the first stage, called L1 or Level 1, the rejection of most events reduces the initial 40 MHz event rate from the detector to about 75 kHz as output from the L1 trigger. These events are passed on to Level 2 (L2) where they are accepted at about a 3.5 kHz rate and passed on to the Event Filter (EF). The EF selects events at a rate of about 200 Hz and only the data from these events are saved for further analysis.

Triggers may additionally be “prescaled” at any level. A prescaled trigger only runs on a fraction of possible events. For example, a trigger with a L2 prescale would only consider some of the events satisfying its L1 requirements and would not be run at all on the others. This is done to keep individual triggers which would have a very high rate, including many triggers used for calibration, from overloading or using too large a share of the processing resources.

Level 1

The L1 trigger is fully hardware-based and is therefore the least changeable of the trigger chain. It uses basic measurements to make quick decisions of not only whether to outright reject and event, but also where localized reconstruction at L2 should be performed. The available measurements are coarse and use only the calorimeters and the MS, with ID information unavailable until Level 2. Each decision much be reached within 2 μs due to the limited amount of memory available to the Readout Buffer (ROB) to store each event. The ROB stores the data temporarily and passes a portion of it to L2. Upon receiving the L2 decision it will either discard the data or transmit it to the EF.

Jets, electrons, photons, and τ-lepton identification is performed with the calorimeter. Energy is summed in trigger towers, 0.1×0.1 regions in $\eta \times \phi$ that include both the ECal and HCal. Multiple trigger towers can be combined to perform energy measurements. For example, L1 jet identification uses a wider region in $\eta \times \phi$ to determine E_{T} than does L1 τ identification: 0.4×0.4 in $\eta \times \phi$ for a jet vs 0.2×0.2 in $\eta \times \phi$ for a τ. Muons, on the other hand, are identified in hits in RPC and TGC stations in 0.2×0.2 regions in $\eta \times \phi$. Muon momentum is also estimated from these hits. For the calorimeters and MS, if the energy or momentum+hit thresholds are sufficiently high a Region of Interest (RoI) is identified in $\eta \times \phi$. An event is passed on to Level 2 if the measurement within the RoI exceeds the combined thresholds set by any L1 trigger. Thresholds may use multiple RoIs to require several objects above a certain E_{T} (calorimeter) or p_{T} (MS), or to place cuts on ΣE_{T} or

$E_{\mathrm{T}}^{\mathrm{miss}}$.

The High Level Trigger

Taken together the L2 and EF triggers are called the High Level Trigger (HLT). They are software-based and can therefore be altered without needing to physically alter the electronics. However, adjustments to the trigger that loosen requirements can obviously not be applied retroactively to capture long-since rejected events. As a result, HLT trigger changes are not made very frequently.

The L1 trigger is said to "seed" the L2 trigger. While the L2 trigger performs reconstruction with the normal detector granularity, it does so only in the RoIs identified by the L1 trigger. Inner detector information is first incorporated at this level, allowing the L2 trigger decision to incorporate tracks. Jets, muons, and the electron, photon, and τ reconstruction are of course refined.

The reduction of the event rate at L2 to about 3.5 kHz allows for the reconstruction of full events. Jets and other objects reconstructed at L2 are reconstructed again, using the full detector, to yield the most accurate estimation of their properties. While the algorithms used are not identical to those used *offline*, that is those used on the data which has been saved to disk and can be processed at a *relatively* leisurely pace, they are nonetheless a close approximation.

Chapter 3

OBJECT RECONSTRUCTION

Particles passing through ATLAS interact with its subsystems in several ways (Figure 2.5). Details of the various particle interactions with the detector need to be combined in order to identify and describe the particle producing them. Due to the high multiplicity of particles in a collision event this process is subtle and must utilize multiple algorithms and combinations of detector elements.

3.1 Tracks and the Primary Vertex

Tracks reconstructed from individual particle-detector interactions reveal the passage of charged particles through the ID of ATLAS. They are used both to identify the particles produced in the collision as well as to locate the primary vertex - the proton-proton interaction point - by extrapolating their paths beyond the layers of material into the beam pipe. By convention the geometry dependent parameters used to describe tracks, such as η, ϕ, the transverse component of the momentum p_{T}, and the impact parameters are calculated at the track perigee, the distance of closest approach to the z-axis, and uniquely identify the track.

Tracks are reconstructed from *spacepoints*, which are three-dimensional representations of detector measurements [28]. ATLAS uses two different track reconstruction algorithms: the “inside-out” algorithm and the “outside-in” or “back-tracking” algorithm [28, 8]. Their names refer to the order in which spacepoints are connected to form tracks. The inside-out algorithm runs first and “seeds” the track with silicon hits before extrapolating outwards and finding coincident hits in the TRT. The outside-in algorithm runs afterwards and uses leftover TRT hits to seed tracks which are then extrapolated back towards the IP to locate coincident silicon hits.

3.1.1 Space Point Identification

Pixel spacepoints are simple to determine due to the high granularity of the pixel detector .In contrast a single SCT sensor cannot be used to accurately determine the three-dimensional coordinates of the interaction of the passing particle within the module. As described in Section 2.3.1, two SCT microstrip sensors are glued together back-to-back at a small stero angle to allow determination of the the coordinate orthogonal to the beam direction. A typical particle leaving the interaction point will pass through three pixel modules and four SCT modules, resulting in a maximum of seven unique spacepoints to a track. The intersection of the trajectory of two or more charged particles may result in shared spacepoints. If a particle passes through inert material or dead modules "missing" spacepoints, also called "holes", may result.

Spacepoints cannot be constructed in the TRT. The drift time for ionization electrons to reach the wire is converted into a drift radius for each TRT. Given the direction of the particle a pair of drift circles produces two possible drift segments, referred to as left-right ambiguity. Several TRT hits necessarily need to be combined to determine which side of a wire the particle passed by if the track is not also incorporating hits from the silicon layers.

3.1.2 Track Reconstruction

Spacepoints from the pixel detector and first SCT layer are combined into track seeds for the inside-out algorithm. Tracks candidates are then extrapolated from the seeds into the SCT layer by layer, incorporating SCT hits and recalculating the track goodness of fit χ^2. Any hit resulting in a large χ^2 is removed as an outlier.

Not all seeds result in viable track candidates and not all track candidates result in tracks. Many charged particles are created in most collisions that are considered interesting and they leave many hits within the ID. Fake (not associated with the trajectory of an actual particle) track candidates will be present due to the large hit multiplicity and must be rejected. To rank track candidates by their likelihood to correspond to an actual charged particle the candidates are first refit with a more complex algorithm that includes more detailed detector geometry information. Candidates with many unique hits and few holes will be identified. Refitting can then be performed after shared hits are assigned to these higher quality tracks. Figure 3.1 illustrates an example of track candidates sharing hits and possessing holes in the SCT layers. Candidates with poor quality will be rejected from further processing. Finally, the set of surviving candidates are extended as tracks into the TRT to find associated hits and one more stage of refitting is performed.

After the inside-out track finding is completed, the outside-in track finding algorithms runs first by removing TRT hits matched to inside-out tracks and then using TRT segments to seed tracks. This algorithm is useful for identifying tracks corresponding to particles resulting from the interactions of primary particles in the inner layers of the detector such as tracks resulting from converted photons. Fitting is performed only in the $R-\phi$ plane in the barrel and the $R-z$ plane in the endcap for broad η slices due to the inability of the TRTs to provide coordinate information along their length. Tracks are extended into the SCT and pixel layers to find associated hits which were not assigned to inside-out tracks, refit, and poor quality tracks are removed in a manner similar to that used by the inside-out algorithm.

3.1.3 Primary Vertex Reconstruction

Vertices are located by extrapolating tracks into the beampipe and looking for the intersection of multiple tracks [28, 29, 30]. The primary vertex is the vertex at the location of the proton-proton hard-scatter. Vertex finding is seeded using the z coordinate of the intersection of the beamline and each extrapolated track. The “first” seed is the global maximum in the z coordinate distribution. Tracks within $7\sigma_z$ of the seed are candidates for inclusion in the reconstructed vertex. However, the tracks must satisfy certain quality criteria to be used in vertex reconstruction. Tracks are required to have $p_{\mathrm{T}} > 400$ MeV, 9 silicon hits with no pixel holes, and $|d_0| < 4$ mm. The impact parameter $|d_0|$ is the distance of closest approach

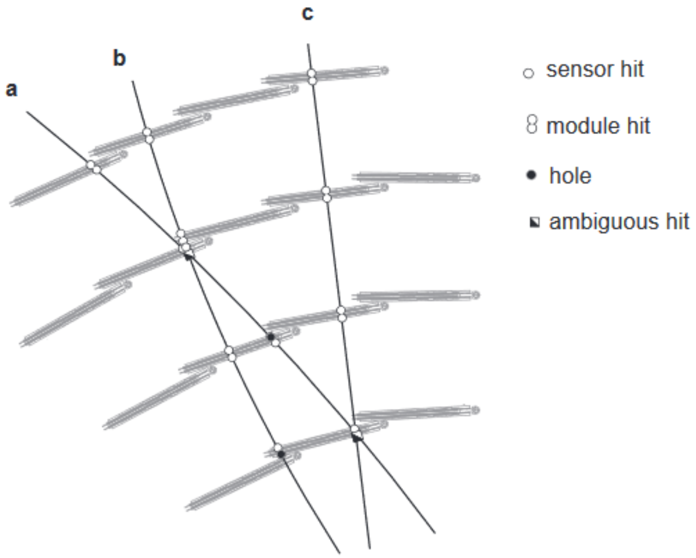

Figure 3.1: An example of various types of hits in the SCT layers. A sensor hit is one within a single SCT strip while a module hit is one in both of the paired strips. An ambiguous hit is one shared by two or more tracks. Track candidates with few holes and ambiguous hits are the first to be considered as actual tracks.

in the xy-plane of the track to the z-axis. The constraint on $|d_0|$ prevents the reconstruction of vertices outside of the beampipe. To determine the vertex position iterative fits are made in which outlying tracks are given lower weights in each iteration to improve the fit χ^2 until a minimum is found. The vertex with the highest sum track p_{T}^2 is taken as the primary vertex, the location of the hard scatter, while the other vertices are assumed to be pile-up vertices. The overall vertex reconstruction efficiency (number of reconstructed vertices over the number of in-time interactions) is above 80% for events with few vertices but falls to 50% for events with 40 or more interactions [31].

3.2 Electrons, Photons, and Muons

Electrons, photons and muons are common particles and are present in many events. Their accurate and efficient reconstruction is therefore fundamental to many analyses. Reconstruction of electrons and photons uses a combination of the inner detector and the electromagnetic calorimeter. Both of these particles are usually stopped by the ECal. Muons, on the other hand, deposit only a fraction of their energy in the calorimeter and their reconstruction, unsurprisingly, incorporates the muon spectrometer. None of these three objects are explicitly used in this analysis but their accurate reconstruction is still important to calculations such as that of the event's missing energy, which is used for identifying non-collision backgrounds [32].

3.2.1 Electron Reconstruction

Electrons are reconstructed using a combination of inner detector and calorimeter requirements [33, 34]. Reconstruction begins from seed clusters in the middle ECal layer using 3×5 cells in $\eta \times \phi$. A valid seed must possess $E_{\mathrm{T}} > 2.5$ GeV in this region. If a suitable track with $p_{\mathrm{T}} > 0.5$ GeV is found near the cluster then reconstruction proceeds using a sliding window algorithm, an algorithm where a window of fixed $\eta \times \phi$ is positioned to maximize the enclosed energy. Reconstruction continues with the identification of the electron's ID track. Candidate tracks are permitted to have at most $\Delta\eta < 0.01$ to the cluster. In the event that multiple candidate tracks are present the track closest to the cluster barycenter is chosen. Tracks are also required to satisfy ID hit requirements which aids in the rejection of converted photons. For forward electrons ($|\eta| > 2.5$), matching to ID tracks are necessarily not performed. However, all candidate electrons are subject to further cuts on the shower shape and leackage into the HCal to reject background electrons and fakes. Due to the small depth of the first layer of the ECal most of the energy of an electron is deposited in the second ECal layer. The width of the shower is affected by the bending of the electron track in the magnetic field. A cut is also placed on the ratio of the cluster energy to the electron momentum, which should be near one due to the electron's low mass.

3.2.2 Photon Reconstruction

Photon reconstruction is designed to identify both converted and unconverted photons [8, 33, 35]. Converted photons undergo pair production within the detector material. Unconverted photons, by contrast, undergo no material interactions prior to reaching the ECal.

Photon reconstruction is seeded in the same way as electron reconstruction. In the case of photons, seeds are selected if they lack associated tracks, or if they posses a track or track pair consistent with a photon conversion. A track pair results when a track is reconstructed for both the electron and positron, the intersection of which defines the conversion vertex. Single tracks are frequently TRT-only tracks while track pairs tend to include Si hits. As with electrons, cuts are made on the shower shape and on leakage into the hadronic calorimeter to reject background and fakes. Photons which reach the calorimeter are not bent by the magnetic field and so will tend to create very narrow showers. Converted photons are reconstructed from the electron showers and tracks left by their decay products. Additional cuts are applied to unconverted photons to discriminate between single photon showers and pairs of photons resulting from neutral meson decays.

3.2.3 Muon Reconstruction

As with ID tracks, the track parameters of muon tracks (p_{T}, η, ϕ) are calculated at the perigee of the extrapolated track. Muons can be reconstructed using only the MS (standalone muons) or by combining MS and ID tracks (combined muons) [36, 37]. ID tracks with corresponding MS segments, but not tracks, result in a third type of muon called the tagged muon. In all three cases MDT hits are combined into segments within single MDT chambers. Within the short distance of a chamber the trajectory may be approximated as a straight line, i.e. the track bending is assumed to be negligible. The segments will incorporate trigger (RPC or TGC) coordinate information, when available, to refine their position resolution.

MS track reconstruction requires at least two muon segments pointing towards the IP which result in a good (low χ^2) fit to a possible track. These tracks are extrapolated towards the beampipe, accounting for both multiple scattering and energy loss to detector material. The typical muon will lose ~ 3 GeV in the calorimetry.

If an extrapolated standalone muon track lies near an ID track, an attempt is made to combine the two. If the χ^2 for the combined fit is low enough, the muon is designated a combined muon. The track parameters for the combined muon may be a reweighted average of the MS and ID tracks or may be derived from the fit parameters of the combined track depending on the algorithm chosen for the combination.

Low p_{T} muons may not produce enough hits in the MS to directly reconstruct an MS track for the muon. However, they will still leave ID hits. If an ID track extrapolated to the MS is associated with one or more track segments, even if those segments were not themselves reconstructed into a track, then the track is designated a tagged muon. The tagged muon's track parameters are identical to those of the ID track.

3.3 Jets

The hadronic collisions in ATLAS produce a variety of particles, including huge numbers of quarks and gluons. These quarks - with the exception of the top quark - and gluons (via their radiated quark pairs) quickly hadronize, producing a collimated shower of particles with a net momentum equal to that of the initiating quark or gluon. Some of these particles, such as the π_0, decay more or less instantaneously while others, such as the K_0 and $\pi^{\pm}$, are more likely to reach the calorimeter without decaying. This shower of particles is termed a "jet" and is an extremely common object in LHC collisions. Figure 3.2 shows, as a function of jet p_{T}, the average fraction of each particle present in a jet by the time they reach the calorimetry. The majority of the energy in the average jet is carried by photons and charged pions while neutral hadrons carry less than 20%. In addition to production in the initial proton-proton collision, jets can also result from hadronic decay modes of particles such as the Z or τ.

Within the terminology of event reconstruction in a detector, "jet" takes on an additional meaning. Track jets are the collection of tracks left in the inner detector by charged particles

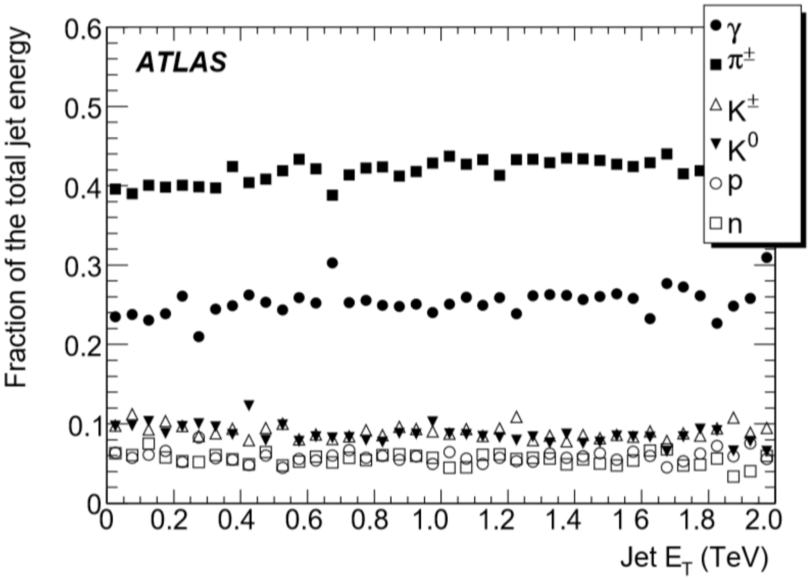

Figure 3.2: The relative fraction of each particle found in jets in ATLAS as a function of jet E_T [8]. The fractions correspond to jet particle content at the inner face of the electromagnetic calorimeter.

that are part of the jet. However, the majority of the time "jet" is used in this analysis it refers to the reconstructed calorimeter object.

Within the calorimeters an attempt to reconstruct a track corresponding to a particle in a jet would be misguided. The calorimeter's purpose is the measure the energy and related properties of the jet. Incoming particles interact with the calorimetry and deposit their energy across many cells both parallel to and perpendicular to the incoming particle's momentum. Instead of tracks, roughly cone-shaped collections of energy deposits are reconstructed and analyzed. These objects are the jets that form the backbone of this analysis.

A jet may have one or more charged tracks in the ID corresponding to the the passage of particles forming the jet. It may have muon tracks or segments associated with it as well if a muon was produced as part of the jet or if the hadronic calorimeter fails to fully absorb the energy of the shower and some particles "punch through" the calorimeter. Ideally, the reconstructed energy of a jet will be well calibrated and include the full shower. To approach this ideal any jet reconstruction algorithm should be both infrared and collinear safe. An infrared safe jet clustering algorithm will reconstruct the same jet in the presence of soft particles. These soft particles are numerous from ISR and the underlying event and should not affect the jet shape or have a significant impact on its final energy. On the other hand, two collinear, hard particles are likely products of the same shower and should not be reconstructed as separate jets. Collinear safe algorithms correctly group hard objects into the same jet.

Jets which result from the decay of a long-lived neutral particle will have properties, such as the spatial extent and distribution of their energy deposits in the calorimeter, or the presence of charged tracks in the inner detector pointing towards those deposits, that depend on how displaced from the primary vertex their decay is. The accuracy and precision of the jet reconstruction determines how well these jets can be separated from showers of particles that originate at the primary vertex.

3.3.1 Clustering and Initial Reconstruction

Offline jet reconstruction begins with the formation of clusters, which is performed by a topological clustering algorithm [38, 39, 40]. Reconstruction begins with a high energy seed cell. Other cells are iteratively added to the seed cell to create a topological cluster, a "topocluster", and these clusters are in turn combined to form jets. Jets in this analysis are reconstructed from topoclusters using the anti-k_t algorithm [41], an infrared and collinear safe sequential recombination algorithm.

Topoclusters group neighboring cells in the $\eta - \phi$ plane with significant (high with respect to noise) energy deposits in order to reconstruct the stages of showering that occur within the calorimeter material. Ideally each cluster contains the energy of a single track jet particle which has survived until the calorimeter. The seed cells are required to possess a signal-to-noise ratio $E_{\text{cell}}/\sigma_{\text{noise}} > 4$, where the noise is the expected RMS of the electronic noise and which includes a pile-up contribution. For each seed cell neighboring cells are iteratively added if the neighbor satisfies the requirements $E_{\text{cell}}/\sigma_{noise} > 2$. Cells satisfying the signal-to-noise threshold but neighboring more than one cluster result in a merging of the clusters. Neighboring cells satisfying only $E_{\mathrm{cell}}/\sigma_{\mathrm{noise}} > 0$ rather than the higher threshold and neighboring multiple cluster do not initiate a merging of clusters and instead are added only to one of the clusters. As a final step after the clustering of cells has been completed the local energy maxima for each cluster are located. A cluster is split into multiple new clusters or more than one local maximum is found. The resulting clusters are then used to reconstruct the event's jets.

Jets in this analysis are reconstructed with the anti-k_{t} algorithm, but several algorithms exist for combining clusters into jets. The principal strategy is to determine if the separation of two clusters is large enough, with respect to their energy, that they are likely to be the result of different showers rather than part of the same jet. The relevant parameters are the distance d_{ij} between clusters i and j, and d_{iB}, the distance between i and the beamline. The algorithm loops over clusters i and j and compares all d_{ij} and d_{iB} to identify the minimum value. If the smallest value is a d_{ij} then clusters i and j are identified as belonging to the same jet and are merged, while if it is a d_{iB} then i is identified as belonging to a separate jet and is removed from the set of clusters.

Jet clustering algorithms differ in how they define d_{ij} and d_{iB}. In general

$$d_{\mathrm{ij}} = min(k_{\mathrm{ti}}^{2p}, k_{\mathrm{tj}}^{2p})\frac{\Delta_{\mathrm{ij}}^2}{R^2} \tag{3.1}$$

$$d_{\mathrm{iB}} = k_{\mathrm{ti}}^{2p} \tag{3.2}$$

and

$$\Delta_{\mathrm{ij}}^2 = (y_{\mathrm{i}} - y_{\mathrm{j}})^2 + (\phi_{\mathrm{i}} - \phi_{\mathrm{j}})^2 \tag{3.3}$$

where k_{ti} is the transverse momentum of i, y_{i} is its rapidity, and ϕ_{i} is its azimuthal angle. The distance parameter R has several common values. Larger R will be less likely to underestimate the energy of wider jets, but will also be more prone to overestimating energies due to incorporating soft jets not originating from the initiating parton. The case $p = 1$ corresponds to the k_{t} jet reconstruction algorithm while $p = -1$ corresponds to the anti-

k_{t} algorithm [41]. The Cambridge/Aachen algorithm uses $p = 0$ [42, 43]. Each final jet's four-vector is the sum of the four-vectors of each of its topoclusters.

This analysis uses anti-k_{t} ($p = -1$) jet reconstruction with R set to 0.4. Note that d_{ij} is large if either both of the clusters are soft or if their spatial separation is very large. This requires particularly hard objects to be close to collinear to be reconstructed as the same jet while softer objects will tend to be merged to harder ones over similar distances. Pairs of soft particles tend not to be combined and the softest are removed as soft jets.

3.3.2 Jet Quality

Not every reconstructed jet is considered of sufficiently good quality be incorporated into an analysis. Jets might be the result of noise or some other source that is not the hard-scatter or they may contain a large number of dead or noisy cells. Most analyses use a definition of good jets defined by a dedicated jet data quality group [44]. Searches for exotic events, such as this one, require modification of the standard criteria.

Common jet parameters for determining the quality of a jet include, with respect to the distribution of energy between calorimeter layers:

- EMF: The fraction of the total jet energy deposited in the ECal layers;
- FMax: The largest fraction of energy deposited in a single layer,

and with respect to calorimeter sections:

- HECf: The fraction of energy deposited in the hadronic end cap;
- TileGap3 fraction: The fraction of energy deposited in the calorimetry covering the transition between the barrel and endcap,

and with respect to the distribution of energy in the cells:

- LArQ: The fraction of LAr cells with a Q-factor greater than 4000, where the Q-factor is a measure of the difference in shape between the measured pulse and the predicted pulse which is used to reconstruct the cell energy;

- HECq: Similar to LArQ, but calculated only in the hadronic end cap;
- Dead fraction: The fraction of the jets energy that needed to be extrapolated from dead cells, which simply use the average of surrounding cells for their energy and are flagged by data quality experts;
- NegativeE: The sum of the energy of cells with negative energy, which results from noise and noise suppression,

and finally:

- CHf: The charge fraction, which is the ratio of the sum of the p_T of tracks associated with the jet over the jet's own calibrated p_T;
- timing: The energy weighted mean of the cell timing, where each cell's timing is calculated with respect to the time of flight of a speed of light particle from the IP to the cell;
- η: The reconstructed jet's η.

Jets are first compared to a list of criteria built from these parameters to determine if they are "bad" or "ugly". A jet that is neither of these is designated a"good" jet. A bad jet satisfies at least one of the following criteria:

Related to HEC noise spikes:

- HECf > 0.50 and HECQ > 0.50;
- HECf $> 1 - |$HECQ$|$;
- NegativeE$>$ 60 GeV,

Suggesting non-collision backgrounds:

- $|$Timing$| > 10$ ns;
- $|\eta < 2.0|$ and FMax > 0.99;

- $|\eta < 2.0|$ and EMF > 0.95 and CHf < 0.05;
- $|\eta < 2.0|$ and EMF < 0.05 and CHf < 0.10;
- $|\eta > 2.0|$ and EMF < 0.05,

Suggesting EM coherent noise:

- $|\eta < 2.8|$ and EMF > 0.90 and LArQ > 0.80.

Ugly jets satisfy at least one of the following related to the the jet lying in a region where accurate reconstruction is less probable:

- TileGap3 fraction > 50% of the jet energy;
- Dead fraction > 50% of the jet energy.

LAr noise can result in a noisy cell being reconstructed as a jet or result in poor reconstruction of a jet from the collision. Jets associated with noise spikes generally have large negative energy or poor signal quality in the readout from the calorimeter. Jets from non-collision background more frequently have larger (and often more negative) timing than a typical collision jet. They often contain fewer high energy cells than a collision jet as well.

For Standard Model jets, showers of purely neutral hadrons are unusual enough that removing low EMF jets will not remove too many collision jets. The search described here, which explicitly seeks low EMF jets as a signal, risks losing a substantial number of events if the low EMF criteria are left in place. The low EMF criteria are therefore removed and other cuts are implemented to remove events resulting from non-collision backgrounds. The treatment of non-collision backgrounds is described in Section 5.3.

3.3.3 Jet Energy Calibration

The purpose of jet calibration is to relate the energy measured by the calorimeters to the true energy of the particles depositing the energy and thus the energy of the initiating parton.

As shown in Figure 3.2, on average only about 60% of a jet's energy is carried by charged particles (generally hadrons) and roughly 25% is carried by photons (many of them from π_0 decays). The hadrons, charged or neutral, deposit most of their energy in the hadronic calorimeter.

The initial reconstruction of jet energy is done at the *electromagnetic scale* (EM scale). The EM scale was developed using test-beam measurements for electrons and muons, the muons being necessary to study the deposition of energy in the HCal. It is so named because at this scale the energy of a jet's electromagnetic shower, which is usually dominated by photons, is correctly calculated. Due to the difference in response of the ECal and HCal, the hadronic component will be inaccurate at the EM scale.

In general, a shower of pure hadrons will be reconstructed with a lower energy compared to a pure electromagnetic shower with the same true energy. This difference in response is due in part to energy lost in hadronic interactions in the production of muons, which escape the calorimeter with most of their energy intact, and energy lost to *invisible energy*, the freeing of nucleons or excitation of nuclei during the nuclear interactions. For this and other reasons jets must be calibrated before they are used in an analysis [39, 45, 46, 47].

Accurate reconstruction of the jet energy is non-trivial, complicated by several factors in addition to the different responses of the HCal and ECal:

- Energy deposited outside the calorimeter: via punchtrough and in material preceding the calorimetry

- Energy deposited outside the jet: the trajectory of soft charged particles may be bent outside of the jet cone

- Energy deposited inert elements in the calorimeter: in dead cells and structural material in the calorimeter

- Calorimeter non-compensation in the HCal: only a portion of deposited energy is measured in active cells

- Pile-up and other effects depositing excess energy in calorimeter cells that are included in the jet
- Noise thresholds resulting in mis-measurement in cells with small energy deposits

An alternative initial energy scale is the local cluster reweighting (LCW) scale. Each cluster is assigned as being either electromagnetic or hadronic in origin based on its shape. Weights are then applied to their energy which are derived from single pion MC simulation. This weighting corrects for the different response of the HCal compared to the EHal. However, as is the case of jets beginning at the ECal the jets still require calibration, but typically have a smaller correction to their energy.

Jet calibration combines several complementary corrections and calibrations:

- A correction to the jet origin
- A pile-up correction
- Energy and η calibration
- A residual in situ calibration applied only to data

The complete set of corrections alter both the energy and the direction of the jet. Initial jet reconstruction is performed using the geometrical center of the detector as the jet origin. The origin correction only changes the jet direction to point to the primary vertex and does not affect the energy of the jet. Jet energy *is* modified by the other corrections. The pile-up correction results in an offset of the jet energy at the EM scale, while the remaining corrections produce a scale factor to be applied to the jet's four-vector.

Pile-up and the underlying event may result in an increase in the reconstructed energy of the event. The LAr cells are specially sensitive to out of time pile-up in addition to in time pile-up - they are affected by collisions in the 12 preceding and 1 following BC. The pile-up correction is derived on MC and is based on the number of primary vertices (N_{PV}), the pile-up (μ), and the bunch spacing and is applied as an offset at the EM scale before any other corrections are applied.

The energy and η calibration is also derived on MC where it is intended to restore the reconstructed energy to the truth value, correcting for effects including energy lost to inert material or deposited outside of the jet cone. The correction depends on both the jet energy and the detector η of the jet.

The final in situ residual calibration is derived using multijet MC and collision data. This last correction is applied to jets in collision data and is determined from collision events by comparing the energy of a reconstructed jet to a reference object such as a photon, Z, or another jet.

3.4 Missing Energy

ATLAS has sufficient coverage in the transverse direction for the calorimeters to capture most particles other than neutrinos and muons. Furthermore, the initial transverse momentum of the colliding protons is near-zero. From this last point, is is expected that the net momentum in the transverse direction of colliding particles will be equal to zero. However, the momenta of all particles cannot be determined, while the energy of most particles can be. To measure the momentum balance in the event the quantity $E_{\mathrm{T}}^{\mathrm{miss}}$ is used [48]. The $E_{\mathrm{T}}^{\mathrm{miss}}$ is defined as the negative vectorial sum of energy in the transverse plane of all objects reconstructed in the event. The $E_{\mathrm{T}}^{\mathrm{miss}}$ also includes the transverse momentum of reconstructed muons due to their tendency to escape the calorimeters.

Were every particle or its decay products captured by the calorimetry the $E_{\mathrm{T}}^{\mathrm{miss}}$ of the event would be zero. Neutrinos, of course, violate this ideal and escape the detector, taking their energy with them. Thus in a Standard Model event a large $E_{\mathrm{T}}^{\mathrm{miss}}$ is a signature of events with one or more high p_{T} neutrinos. However $E_{\mathrm{T}}^{\mathrm{miss}}$ can result from other sources as well.

Non-collision backgrounds are a non-negligible source of $E_{\mathrm{T}}^{\mathrm{miss}}$. Beam halo muons, muons traveling parallel to and roughly in time with the proton bunches, can leave energy deposits in the calorimeters. Likewise cosmic ray muons or showers may deposit energy in the calorimeters. The spatial distribution of the deposited energy will rarely be symmetric around any collision and instead result in reconstructed $E_{\mathrm{T}}^{\mathrm{miss}}$. Other possible sources of $E_{\mathrm{T}}^{\mathrm{miss}}$ arise in various models addressing physics beyond the SM, such as from escaping LLPs.

The $E_{\mathrm{T}}^{\mathrm{miss}}$ from the calorimeters is calculated as:

$$E_x^{miss} = -\sum_{i=1}^{N_{cell}} E_i \sin\theta_i \cos\phi_i \tag{3.4}$$

$$E_y^{miss} = -\sum_{i=1}^{N_{cell}} E_i \sin\theta_i \sin\phi_i \tag{3.5}$$

$$E_{\mathrm{T}}^{\mathrm{miss}} = \sqrt{(E_x^{miss})^2 + (E_y^{miss})^2} \tag{3.6}$$

where E_i, θ_i, and ϕ_i are the cell energy, polar angle, and azimuthal angle respectively. The sum excludes cells flagged as noisy by the ATLAS database and only includes cells belonging to topoclusters in a further effort to suppress noise.

Muons are included in the $E_{\mathrm{T}}^{\mathrm{miss}}$ calculation when they are found with $|\eta| < 2.7$. For $|\eta| < 2.5$ combined muons are used, while standalone muons must be used for $2.5 < |\eta| < 2.7$ where ID tracking is not available. The contributions to $E_{\mathrm{T}}^{\mathrm{miss}}$ from muons are simply:

$$E_x^{miss} = -\sum_{i=1}^{N_{muon}} p_x \tag{3.7}$$

$$E_y^{miss} = -\sum_{i=1}^{N_{muon}} p_y \tag{3.8}$$

where the x and y components are added to the calorimeter contribution before taking the square root.

3.5 Measurements of Luminosity and Pile-up

The luminosity measurement is important for predicting pile-up, measuring cross-sections, and thus predicting the final number of events expected in any analysis [49, 50]. The instantaneous luminosity is given as:

$$L = \frac{\mu n_b f_r}{\sigma_{inel}} \tag{3.9}$$

where μ is the average number of interactions per bunch-crossing, n_b is the number of bunches per beam, f_r is the rotational frequency of the beams, and σ_{inel} is the inelastic proton-proton cross-section. The parameters n_b and f_r are machine parameters while σ_{inel} is measured.

It is necessary to know the pile-up present during collisions, but μ cannot be directly measured due to the non-ideal acceptance and efficiency of the detector. Instead, a coefficient ϵ is used to relate μ to the measured μ_{meas}, i.e. $\mu^{meas} = \epsilon\mu$, where ϵ accounts for the acceptance and efficiency of the luminosity detectors. If one defines $\sigma_{vis} = \epsilon\sigma_{inel}$, then:

$$L = \frac{\mu^{meas} n_b f_r}{\sigma_{vis}} \tag{3.10}$$

This definition and substitution is valid if the luminosity and number of interactions are measured by the same luminosity detector. The value of μ^{meas} is determined based on an extrapolation of the fraction of BCs with a hit in the luminosity detectors above the threshold value. A calibration measurement is needed to determine σ_{vis} from the instantaneous luminosity in terms of machine parameters using:

$$L = \frac{n_b f_r N_1 N_2}{2\pi \Sigma_x \Sigma_y} \tag{3.11}$$

where $N_1(2)$ is the number of protons per bunch in beam 1 (2) and $\Sigma_{x(y)}$ characterizes the profile of the overlap of the bunches in the horizontal (vertical) plane. If the number of protons per bunch, which is provided from LHC measurements, is accurately known then this luminosity can be calculated. The parameters Σ_x and Σ_y are measured using Van der Meers calibration scans. In a Van der Meers scan one beam is displaced incrementally in the horizontal or vertical direction and the interaction rate is recorded. At zero beam displacement separation, μ^{meas} is at a maximum value, μ^{meas}_{Max}, and σ_{vis} can be written as:

$$\sigma_{vis} = \mu^{meas}_{Max} \frac{2\pi \Sigma_x \Sigma_y}{N_1 N_2} \tag{3.12}$$

With this final equation it is possible to determine ϵ and thus the actual μ from the luminosity and μ_{meas} provided by the luminosity detectors.

3.6 Data Quality and Good Events

Not every event selected by a trigger is an appropriate candidate for physics analysis. It is the job of various data quality groups to identify which events (or more accurately which consecutive sets of events, called Lumiblocks (LBs)), should be rejected from a physics analysis. Reasons for rejection include sections of the detector being off, significant detector defects which small offline corrections are unsuitable for fixing, and software problems that may result in some data in the event being lost.

The result of the data quality groups' efforts is a good runs list (GRL) that is applied to every analysis to identify events suitable for analysis as well as a set of data quality recommendations to be applied both at the event level and to physics objects. The good jet criteria are in fact an example of such recommendations. All standard event level DQ requirements, including the GRL, are applied in this analysis. Modified good jet criteria are also applied as described above.

Chapter 4

MONTE CARLO SAMPLES

To properly understand the ways in which theoretical particles will interact with the detector and the signatures they will leave it is necessary to generate simulated data. In general, simulated samples of SM events are also produced. The simulated events can then be studied to determine useful analysis cuts for separating signal from background, as well as to understand the nature of various backgrounds or the impact of different systematic uncertainties. The simulated data used in ATLAS is Monte Carlo (MC) data, created by randomly sampling relevant probability distributions. MC sample creation involves several steps:

- Generation: determination of the hard scatter and initial decays
- Simulation: determination of the particles interactions with the detector elements and fields
- Digitization: determination of the signals produced by the detector elements

The same reconstruction software used on collision data can then be applied to the output from the digitization step.

This analysis uses several MC samples for both signal and background studies. The software used to produce them and the physics parameters used for the samples are described below.

4.1 MC Production

The first step in creating a signal MC sample is the simulation of the *pp* collision. The goal is to describe the initial state of the partons prior to the hard scatter itself, the underlying event, and the multihadronic final state. Event generation involves randomly sampling parton PDFs to determine the initial parton states and randomly sampling cross-sections to determine the particles that will be produced by the collision. Only particles that will decay before reaching the beampipe have their decays simulated in this step. Jets from prompt decays therefore have their particle content already at least partially simulated at this stage. The underlying event is also simulated at this stage, but pile-up is not.

There is one exception to the rule that decays beyond the beampipe are not simulated. If the particle is unknown to the next stage of the sample production process the location of the decay will be determined at this stage based on the decay tables provided to the generator. This will be the case for certain theoretical particles which will not interact with the detector prior to decaying to SM particles. The π_{v} produced in the analysis signal samples falls into this category.

Several event generators exist, but this analysis chose to use PYTHIA [51] for all 8 TeV event generation. PYTHIA contains a library of hard processes as well as models for various parton showers, parton interactions, decays, and elements of the underlying event.

The first stage of production only generates the fragmentation, hadronization, and radiation resulting from the collision. It does not determine how, where, and when the generated particles will interact with ATLAS itself. These interactions are simulated with GEANT4 (G4) [52]. G4 is a toolkit dedicated to the simulation of particles passing through matter. This includes when and where particles will interact with sensitive materials to leave hits. Given the geometry, materials, field information, and environmental information (temperature, etc.) within the detector as well as the relevant parameters (such as interaction lengths and possible decay products) of the particles entering ATLAS G4 will choose which physics processes occur throughout the detector volume. G4 is capable of simulating decays, bremsstrahlung, and other processes which create additional particles within the detector volume. The performance of G4 is validated via the comparison of MC and data for well-studied and understood objects such as photons.

G4 determines how particles will interact with ATLAS, but not what signals the electronics will output. Digitization is the transformation of the output of the simulation (G4) stage, specifically the simulated hits, into an approximation of the output of the detector electronics themselves. This stage produces Raw Data Objects (RDOs) which are the input into the reconstruction algorithms discussed in Section 3. Creation of the RDOs requires simulating charge flow to readout electrodes and the front end electronics, and correct conversion of the resulting electronic signals with respect to voltage or current thresholds. Electronic noise is therefore necessarily simulated. Prior to the reconstruction the event is overlayed with actual min-bias data to model pile-up. This is the final stage of sample generation that differs from the production of actual data samples. After digitization the reconstruction stage proceeds identically on both real and simulated data.

4.2 Signal Samples

The HV signal samples are generated using PYTHIA 8.165. The Φ_{hs} is produced via gluon fusion $gg \rightarrow \Phi$ and decayed to pairs of π_{v}: $\Phi_{\mathrm{hs}} \rightarrow \pi_{\mathrm{v}}\pi_{\mathrm{v}}$. Neither the Φ_{hs} nor the π_{v} are part of the default PYTHIA package, but very similar particles are. The compatible particles are members of the Minimal Supersymmetric Standard Model. For the Φ_{hs} the heavy neutral Higgs H^0, with properties matching that of a same-mass SM Higgs. The π_{v} is simulated with the A^0, a pseudo-scalar which couples to the H^0. Only the decay of the H^0 to A^0 is permitted and the masses and A^0 lifetimes are set as desired.

The analysis created eight samples with around 300,000 events each for various combinations of Φ_{hs} and π_{v} masses for a lower mass range (100-140 GeV) of m_{Φ} and five for a higher m_{Φ} range (300-900 GeV). The higher mass samples were generated late into the analysis and as a result were not used to tune the analyiss cut flow in any way. All samples were generated at $\sqrt{s} = 8$ TeV and had lifetimes chosen to allow for a large number of decays throughout the ATLAS volume. The masses of the Φ and π_{v} along with the process cross-section are shown in Table 4.1 on the left-hand side. The branching ratios of the π_{v} at each mass are shown on the right. In all cases the π_{v} decays via its coupling to the Φ, which couples to mass in the same manner as the Higgs and therefor favors the heaviest kinematically available daughter particles.

Table 4.1: The various m_Φ and $m_{\pi_{\rm v}}$ mass points generated for this analysis.

(a) m_Φ and $m_{\pi_{\rm v}}$ combinations

$m_{\rm H}$ [GeV]	σ [pb]	$\pi_{\rm v}$ Mass [GeV]
126	19.0	10, 25, 40

Φ Mass [GeV]	σ [pb]	$\pi_{\rm v}$ Mass [GeV]
100	29.7	10, 25
140	15.4	10, 20, 40
300	3.59	50
600	0.52	50, 150
900	0.06	50, 150

(b) $\pi_{\rm v}$ branching ratios

$\pi_{\rm v}$ Mass [GeV]	BR $b\bar{b}$ [%]	BR $\tau^+\tau^-$ [%]	BR $c\bar{c}$ [%]
10	70.0	16.4	13.4
20	86.3	8.0	5.6
25	86.6	8.1	5.3
40	86.5	8.5	5.0
50	86.2	8.8	4.9
150	84.8	10.2	4.8

The kinematic distributions of the generated low mass and high Φ samples are shown in Figure 4.1. The colliding protons have little transverse momentum. However, the Φ may gain some momentum in the transverse direction ($p_{\rm T}$) as a result of the particle recoiling off of a jet in the underlying event. The Φ will also tend to have some momentum along the beam direction as a result of an imbalance in the momenta of the colliding gluon pair which creates it. This propagates to the η distribution resulting in the two peaks on either side of $\eta = 0$.

The $\pi_{\rm v}$ kinematic distributions are shown in Figure 4.2. The η distribution of the Φ affects the η distributions of the $\pi_{\rm v}$. As a result of the Φ carrying little $p_{\rm T}$ the $\pi_{\rm v}$ are generally back to back (Figure 4.3) in ϕ and may have high $p_{\rm T}$ if the mass difference between the Φ and $\pi_{\rm v}$ pairs is large. Greater boosts from the mass difference correspond to narrower η distributions because the any longitudinal contribution to the boost from the Φ is relatively smaller.

The $E_{\mathrm{T}}^{\mathrm{miss}}$ distributions are of interest to many analyses considering long lived particles, this one included. By considering only events in which both long lived particles decay within the calorimetery it is possible to eliminate events with high $E_{\mathrm{T}}^{\mathrm{miss}}$, a sign in signal that one of the long lived particles has escaped the detector. Figure 4.4 shows the $E_{\mathrm{T}}^{\mathrm{miss}}$ distribution of the signal samples along with the ϕ distribution of the $E_{\mathrm{T}}^{\mathrm{miss}}$. In the high mass samples the π_{v} are quite massive and result in punch-through jets at a significantly higher rate than in the low mass samples.

4.3 Background Samples

In addition to the simulated signal samples simulated QCD multijet samples were also produced. These samples were used in part to develop the multijet background prediction as well as to study various systematic uncertainties relevant to the analysis. The samples are part of a set of official ATLAS samples and were produced centrally. Samples were generated using PYTHIA 8.165 and are separated by the p_{T} of the leading jet. Each of the eight p_{T} slices includes the weighting information required to combine the samples into one representative sample. The weighting depends on a PYTHIA assigned weight, the sample cross-section, the efficiency of the p_{T} filter used to isolate each p_{T} slice, and a pile-up weight also used in the signal samples which accounts for the discrepancy between the pile-up distribution used at the time of the creation of the samples and that which was actually observed in data.

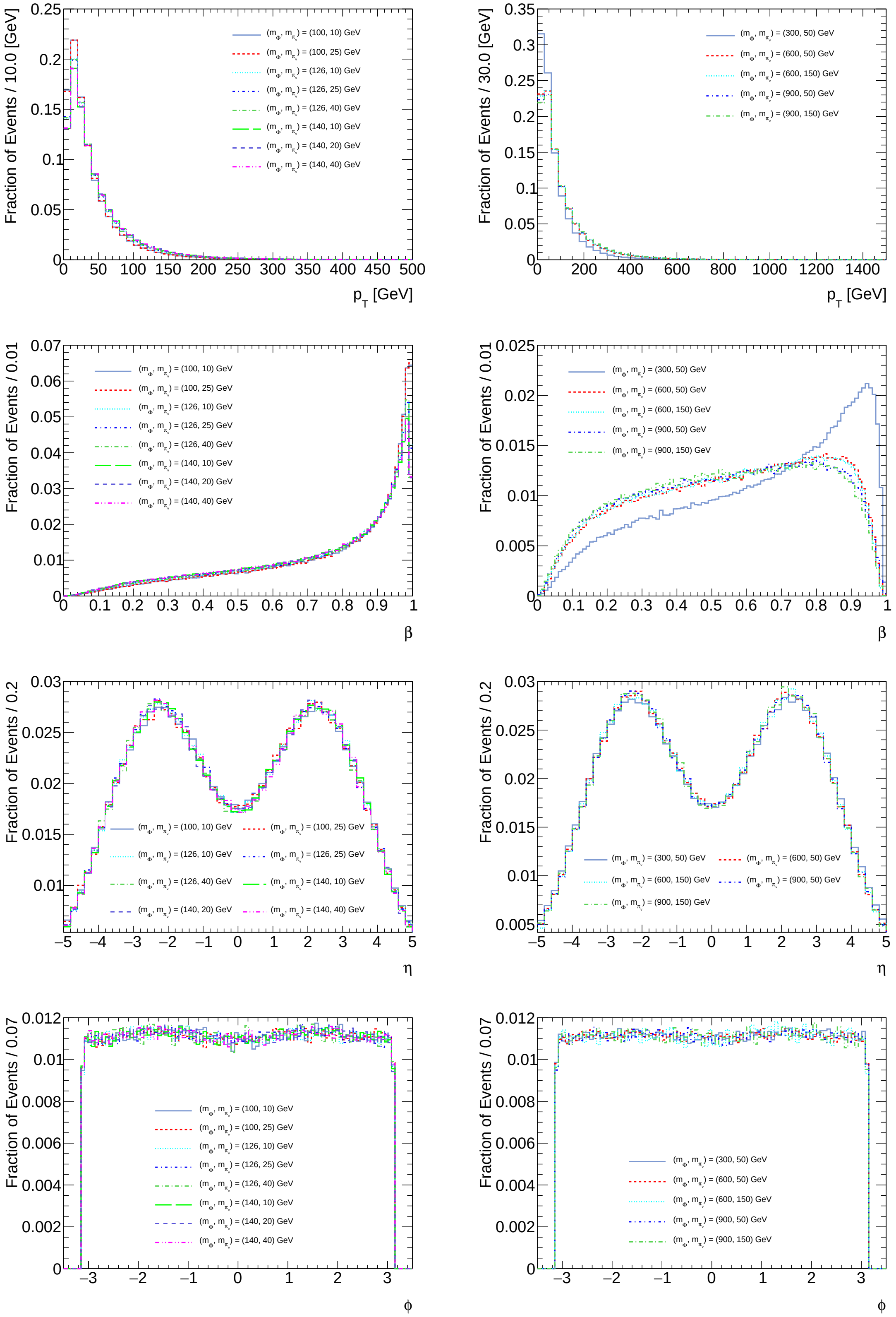

Figure 4.1: The kinematic parameters of the low mass (left) and high mass (right) Φ in the generated signal samples.

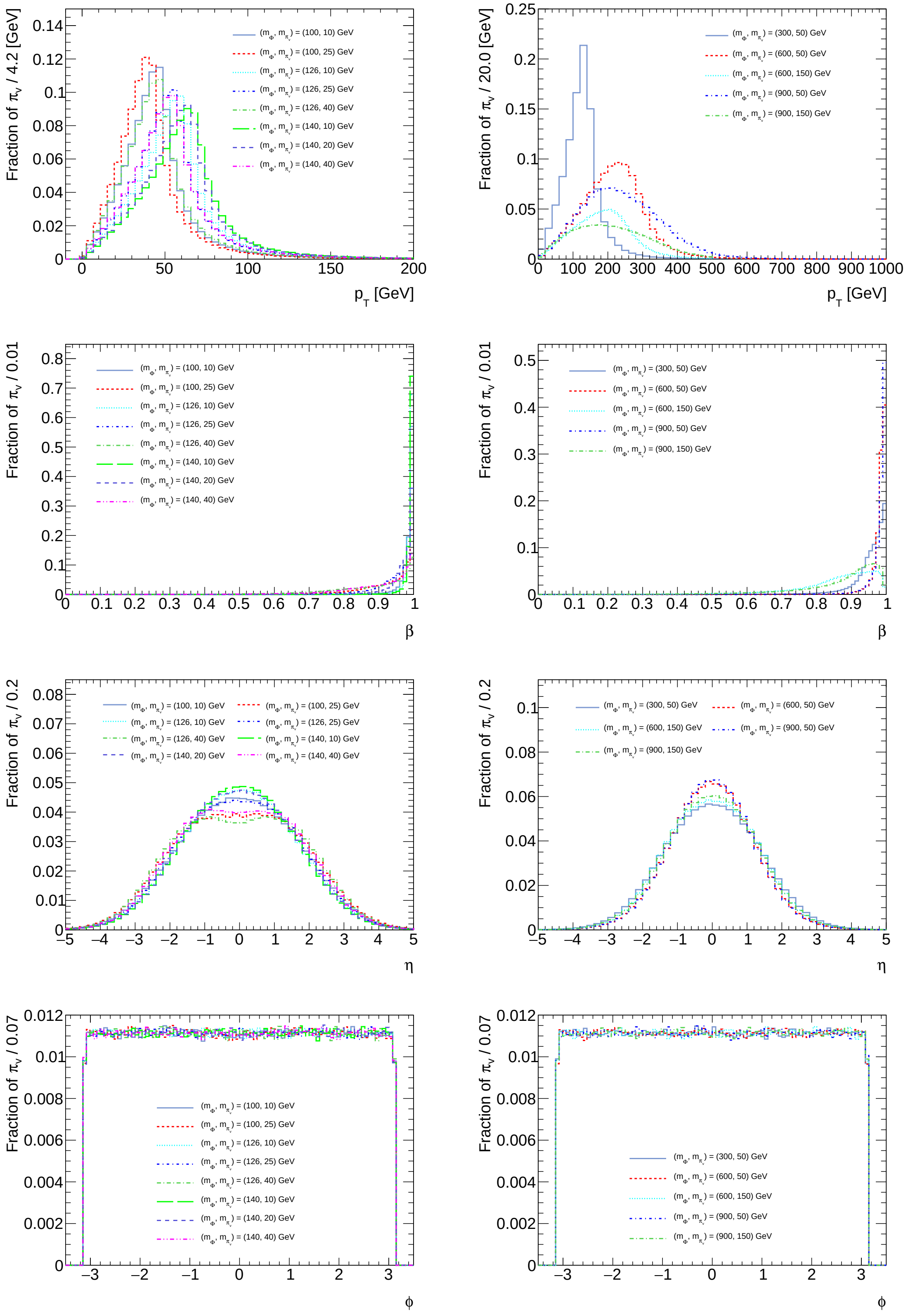

Figure 4.2: Kinematic distributions of the π_{v} produced in the low mass (left) and high mass (right) Φ samples.

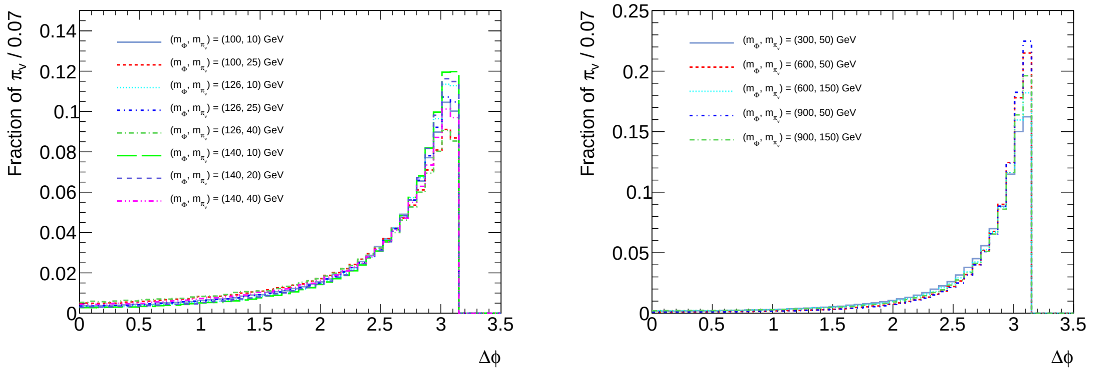

Figure 4.3: The distributions of $\Delta\phi$ of the π_{v} pairs in the low mass (left) and high mass (right) samples.

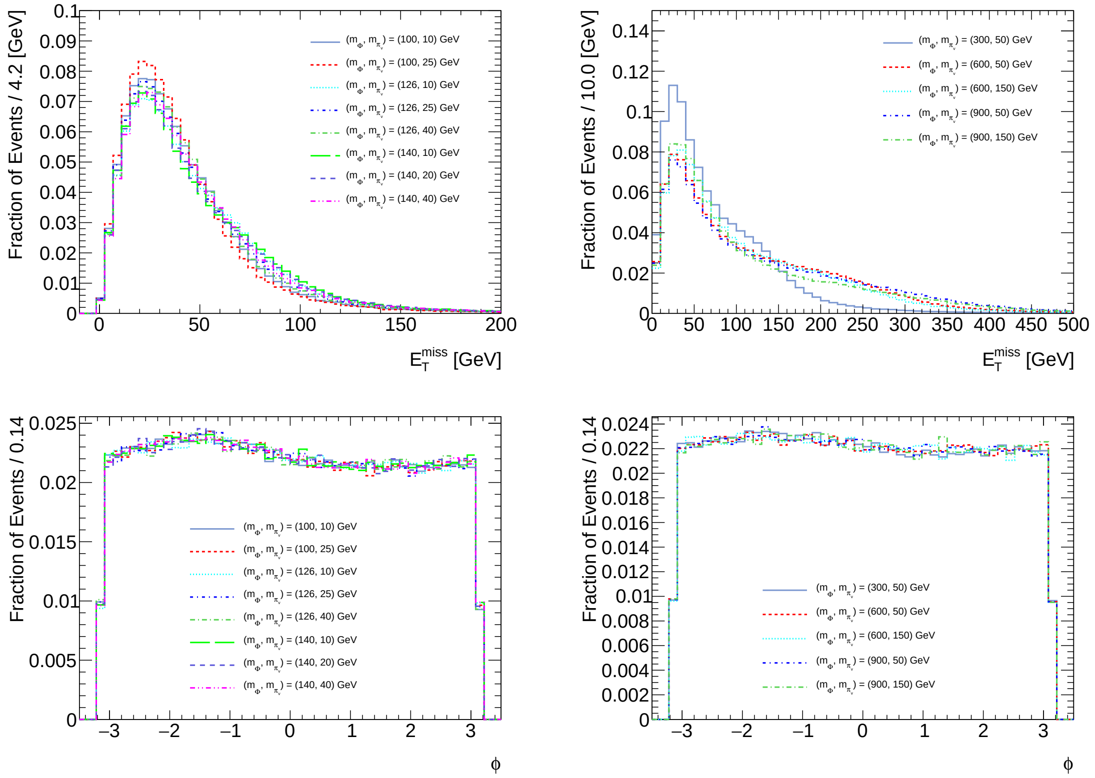

Figure 4.4: The $E_{\mathrm{T}}^{\mathrm{miss}}$and $E_{\mathrm{T}}^{\mathrm{miss}}$ ϕ distributions of the low mass (left) and high mass (right) Φ samples.

Chapter 5

ANALYSIS

The MC samples produced as described in Section 4.2 contain events which may be similar to those produced in a collision, but which are only one theoretical possibility. An analysis searching for theoretical particles must develop a set of *cuts*, a set of requirements, on the parameters of the various reconstructed objects in simulated signal events. The purpose of these cuts is to isolate the signal from various sources of background in order to either identify new physics, if the former is not possible, to set limits on the phase space associated with the signal model. This also requires the careful analysis of backgrounds which can fake signal events.

This analysis [53, 54] is interested in decays of long-lived neutral particles decaying to hadronic states. Such particles produce a variety of unusual signatures depending on which subdetector of ATLAS each LLP decays in. The analysis focuses on the signature resulting from the decay of both LLPs within the HCal, which produces pairs of relatively unusual jets. For example, these jets have abnormally high $\log_{10}(E_{\mathrm{H}}/E_{\mathrm{EM}})$ compared to jets from SM multijet events because SM jets tend to carry a large fraction of their energy in photons and charged particles. Figure 5.1 shows, on the left, the $\log_{10}(E_{\mathrm{H}}/E_{\mathrm{EM}})$ distribution of π_{v} which decay in the HCal, those decaying in the ECal, and the same distribution for QCD jets in the QCD multijet MC sample. The large hadronic component of jet energy compared to the EM component is usually associated with non-collision backgrounds or detector problems such as noise. In these cases the energy comes not from hadrons associated with a collision jet but from some other source. Most analyses will therefore reject such jets for possessing poor quality (Section 3.3.2). As a result, such jets from LLP decays may be present but overlooked by most analyses. The cuts chosen to isolate these events and the relevant backgrounds are discussed in this section.

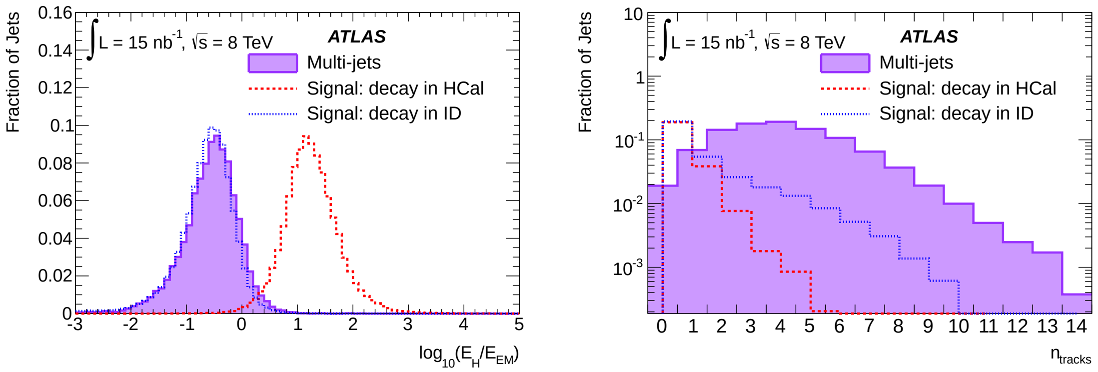

(a) (b)

Figure 5.1: Distribution of (a) $\log_{10}(E_{\mathrm{H}}/E_{\mathrm{EM}})$ and (b) the number of ID tracks associated ($\Delta R < 0.2$) for a SM multijet MC sample and a sample of jets from the signal sample where the π_{v} decays in either the ID or the HCal.

5.1 *Event Selection*

The initial cuts applied by the analysis in order to isolate signal are applied at the event level rather than to individual jets. First and foremost, events are only considered if they passed the CalRatio trigger, described below. The events are then required to pass standard data quality cuts (Section 3.6). Additionally, a special analysis cut to reject beam induced background events, called Line of Fire events and described below, is also applied here. Finally, a cut on $E_{\mathrm{T}}^{\mathrm{miss}}$ is applied to discriminate against non-collision backgrounds.

5.1.1 CalRatio Trigger

The typical SM jet almost always has some fraction of charged particles and photons and so will generally be accompanied by tracks in the ID and posses energy deposits in the ECal. The unusual $\log_{10}(E_{\mathrm{H}}/E_{\mathrm{EM}})$ of the jets sought by this analysis make them rare in events gathered with standard jet triggers. These triggers are also highly prescaled, limiting the total number of events saved for all events, including ones with unusual signatures. To insure a large supply of events with candidate-signal jets this analysis uses a dedicated trigger to select events containing jets lacking large ECal energy deposits and ID tracks. This trigger is called the CalRatio trigger [9].

There are a number of characteristics of π_{v} decays that can be taken advantage of to identify events more likely to contain signal jets. The daughters resulting from a π_{v} decay in the HCal will have little time to separate. This results in a narrow width for the reconstructed jet, even if the opening angle is fairly wide, because jet reconstruction assumes the shower originates at the interaction point. The triggers used to find τ decays, which produce calorimeter objects typically narrower than those produced by hadronic jets, use a narrower window than jet triggers to sum energy. This allows the L1 τ triggers to be unprescaled at lower energies that L1 jet triggers. The CalRatio trigger takes advantage of the narrow π_{v} showers and by seeding the trigger with L1TAU40, the lowest energy unprescaled L1 τ trigger. This L1 trigger requires at least 40 GeV be present in 0.2×0.2 window in $\Delta\eta \times \Delta\phi$. At Level 2 the trigger requires that a jet be reconstructed with at least 30 GeV in $|\eta| < 2.5$. The η criteria insure that the jet is reconstructed in a region in which tracking is available. The jet is then required to have $\log_{10}(E_{\mathrm{H}}/E_{\mathrm{EM}}) > 1.2$ and possess no reconstructed tracks with $p_{\mathrm{T}} > 1$ GeV within a window of 0.2×0.2 in $\Delta\eta \times \Delta\phi$ around the jet axis. The cut on $\log_{10}(E_{\mathrm{H}}/E_{\mathrm{EM}})$ is higher than is necessary to eliminate most SM QCD events, but was set at this level to keep the trigger rate in data at an acceptable level.

At the EF level the jet is reconstructed again and the requirement $E_{\mathrm{T}} > 35$ GeV is made. This is also the stage where the Line of Fire online cuts, detailed below, are applied.

Figure 5.2 shows the probability that a π_{v} decaying in the HCal will fire the CalRatio trigger for various signal samples. The trigger's E_{T} threshold is more easily met by jets from the decay of the high mass samples, which accounts for their significantly higher trigger efficiency. The efficiency falls at larger decay lengths due to leakage of jet energy from the HCal into the MS. It is additionally lower in the endcaps compared to the barrrel as a result of the busy nature of forward events, which tend to include more low energy jets that can, if coincident in $\eta \times \phi$ with a π_{v} decay, result in tracks or ECal energy deposits that result in the jet's rejection by the trigger.

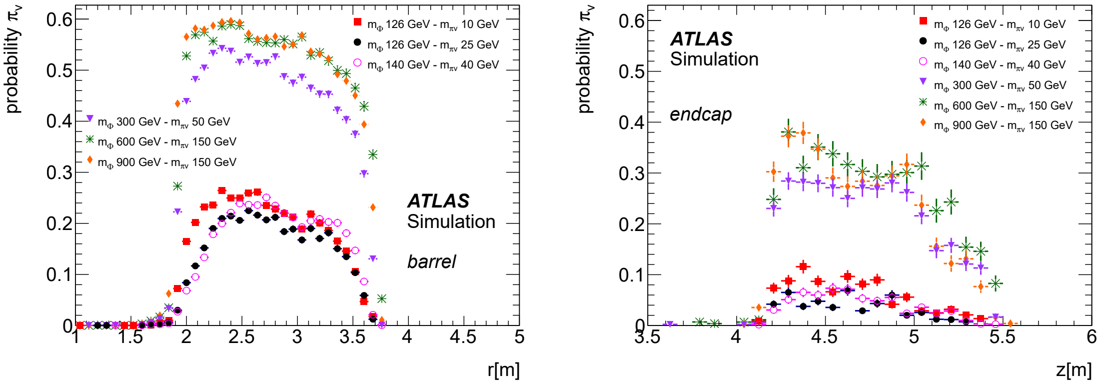

(a)

(b)

Figure 5.2: Distribution of the probability that a π_v decaying in the HCal will fire the CalRatio trigger for decays in (a) the barrel (b) the endcaps.

The trigger was developed on the signal samples at lower mass points. However, as shown in Figure 5.3, the probability that a π_v will satisfy the trigger requirements is higher for the higher mass points. This is due to the greater probability of a higher energy jet satisfying the Level 1 trigger criteria, which could not be lowered due to limits placed on trigger rates.

5.1.2 Line of Fire

Protons in the bunches may scatter inelastically with residual gases in the vacuum chambers or with components such as the collimators, resulting in the production of pions and thus muons. These *beam induced background* (BIB) muons travel parallel to the beam pipe and roughly in time with proton bunches. At the calorimeter level the BIB muons are preferentially, although not entirely, at $\phi \approx 0$ and $\phi \approx \pi$. When one of these muons passes through the calorimeter it can undergo bremmstraulung and leave behind energy deposits. Due to the muon's trajectory these deposits will tend to be a line of cells at constant ϕ (hence the term "Line of Fire" to describe such events [55]) and, if one or more of these deposits is large enough, may result in the reconstruction of a jet (Figure 5.4). If this "jet" is in the

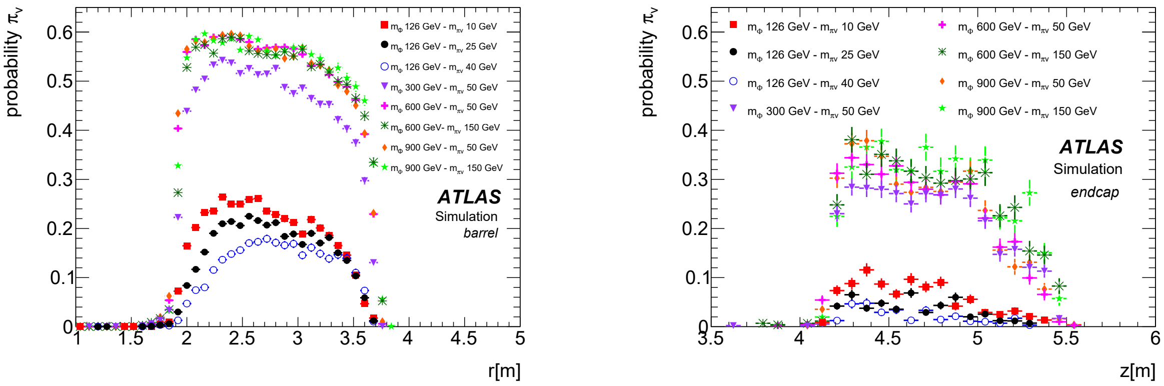

Figure 5.3: Distribution of the probability that a π_v decaying in the HCal will fire the CalRatio trigger for decays in (a) the barrel (b) the endcaps for the high mass signal samples. The $m_\Phi = 126$ GeV samples are shown for comparison.

HCal, then it will naturally lack ECal energy deposits and ID tracks. An early version of the CalRatio trigger lacked any algorithm for the removal of such events and was found to be especially adept at triggering on them. Thankfully, the distinct signature left by BIB muons allows for cuts to be placed both in the trigger and offline to remove such events.

The trigger level Line of Fire (LoF) cut takes advantage of timing. A BIB muon at a calorimeter radius and in time with a bunch crossing will leave energy deposits in cells out of time with what is expected from a particle traveling from the IP to the cell. A row of out of time cells at the same ϕ is suggestive of a BIB event. The trigger vetos any jet and at least four tile cells satisfying:

- Cell $E > 0.24$ GeV
- $\Delta\Phi < 0.2$ between the cell and jet axis
- $\Delta R > 0.3$ between the cell and the jet (to isolate cells along the potential LoF that are not too close to the jet)
- $t < -2$ ns to help isolate cells with early enegy depositions
- $|t - \delta t| < 5$ ns

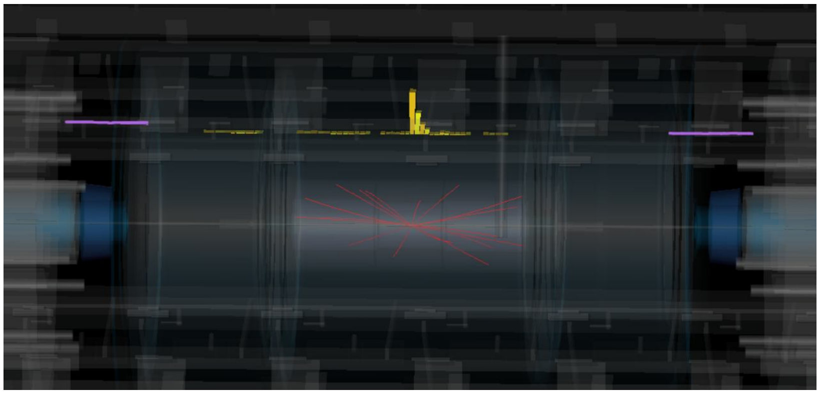

Figure 5.4: A typical Line of Fire event. The purple segments are muon segments while the yellow towers are energy deposits in the tile cells. The hight of a tower corresponds to the magnitude of deposited energy. The red lines represent tracks from the collision [9].

The metric for the timing compares the cell time t to the expected time of a $\beta = 1$ particle. The expected time δt is the timing of hit from a BIB muon traveling in time with the bunch:

$$\delta t = \frac{\pm z - \sqrt{z^2 + R^2}}{c} \tag{5.1}$$

Where R is as defined usually and z is the z coordinate.

These cuts were developed on 2011 7 TeV data and were found to reject $91.0 \pm 0.2\%$ of events identified as being BIB events via a set of offline cuts.

The offline LoF cuts include a cut which duplicates the online LoF algorithm and an additional set of cuts that makes use of muon segments. Muon segments parallel to the beampipe and at the same ϕ as a jet are another signature of LoF events. A triangle cut on the opening angle in ϕ between the the jet and a candidate muon segment, $\delta\phi$, and the fraction of muon momentum along the z-axis γ_{MS} ($\gamma_{\mathrm{MS}} = p_{\mathrm{z}}/|p|$) is used to eliminate these events. The former isolates muon segments in line with the jet and the latter identifies horizontal segments. In the barrel the cut requires two muon segments, one on either side of the calorimeter, and the triangle cuts cover $-0.98 < \delta\phi < 0.98$ and $-1.0 < \gamma_{\mathrm{MS}} < -0.4$ for negative η segments and $0.4 < \gamma_{\mathrm{MS}} < 1.0$ for positive ones. In the endcap jets are given the additional criteria require that the difference in radius between the jet's leading cell and the muon segment, δr, satisfy $\delta r < 120$ mm. The other cuts applied to endcap jets require $|\delta\phi| < 0.2$ and $|\gamma_{\mathrm{MS}}| < 0.98$.

Events identified offline as LoF events are rejected from the pool of events to be analyzed. On the 2011 7 TeV data, the offline cell timing cut alone was found to remove $91.0 \pm 0.2)\%$ events while the muon segment cut was similarly found to remove $80.1 \pm 0.2\%$ of the identified LoF events. The combination of trigger cut and paired offline cuts reduce BIB events to a near-negligible level as verified by the background estimation in Section 5.3.

5.1.3 $E_{\mathrm{T}}^{\mathrm{miss}}$ Cut

In the benchmark model used by this analysis the only source of significant $E_{\mathrm{T}}^{\mathrm{miss}}$ comes from an LLP decaying beyond the calorimeters or from especially energetic jets punching through the calorimeter. To reduce the background contribution from cosmic ray muon and BIB events events are required to satisfy $E_{\mathrm{T}}^{\mathrm{miss}} < 50$ GeV. Figure 5.5 shows a comparison of the $E_{\mathrm{T}}^{\mathrm{miss}}$ distribution of a signal sample, events triggered on empty bunch crossings (cosmic events), and events from the QCD multijet MC sample. This requirement on the $E_{\mathrm{T}}^{\mathrm{miss}}$ was chosen when only the low mass distributions were available and so is non-ideal for the high mass samples. The samples generated with a high Φ mass have high $E_{\mathrm{T}}^{\mathrm{miss}}$ (Section 4.2) due to jets punching through the calorimeter, allowing some of their energy to escape.

5.2 Jet Selection

Cuts on individual jets are applied to events passing all event-level cuts. The 2012 cut flow was developed using the low Φ mass signal samples and, as will be shown, is less efficient on signal samples with higher mass points despite their superior trigger efficiency. As an initial step the CalRatio trigger objects (jets) were matched in $\eta - \phi$ to the JES calibrated jets reconstructed by the full offline algorithm. Any offline jet matching a trigger object is termed a *triggering jet* and the corresponding π_{v} is termed the *triggering* π_{v}. Jets and their corresponding π_{v} which do not match a trigger object are termed *non-triggering*. Most

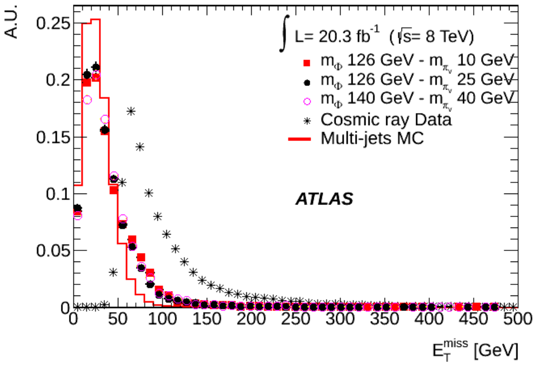

Figure 5.5: A comparison of the $E_{\mathrm{T}}^{\mathrm{miss}}$ distribution in a signal sample, the SM multijet sample, and the cosmic muon sample.

events passing the trigger have a single triggering jet. In signal samples this almost always corresponds to an LLP decaying within the HCal, as shown in Figure 5.6.

The analysis searches for two jets consistent with the decay of neutral LLPs in order to suppress the background. Most cuts are identical for the triggering and non-triggering jet in the pair. Cuts are applied sequentially, first to the triggering jet and then to the non-triggering jet. Each jet is required to first satisfy $-1 < t < 5$ ns, a cut present to suppress non-collision background and which will be discussed in further detail in the next section. Jets are then required to satisfy a minimum cut on their E_{T}, $E_{\mathrm{T}} > 60$ GeV for the triggering jet and $E_{\mathrm{T}} > 40$ GeV for the non-triggering jet. In the event that two or more trigger jets are present in the event only one jet is required to satisfy the higher cut. The cut values are determined primarily by the E_{T} distribution for triggering and non-triggering jets in signal samples, which in turn depend on the E_{T} distribution of the triggering π_{v}, as shown in Figure 5.7 and Figure 5.8.

After the cut on transverse energy the jets are required to satisfy cuts placed on their $\log_{10}(E_{\mathrm{H}}/E_{\mathrm{EM}})$ and the number of ID tracks associated with them. Jets must satisfy $\log_{10}(E_{\mathrm{H}}/E_{\mathrm{EM}}) > 1.2$ and have no tracks with $p_{\mathrm{T}} > 2$ GeV within $\Delta R < 0.2$ of the jet axis. As shown in Figures 5.9 and 5.10, non-triggering π_{v} tend to produce trackless jets a

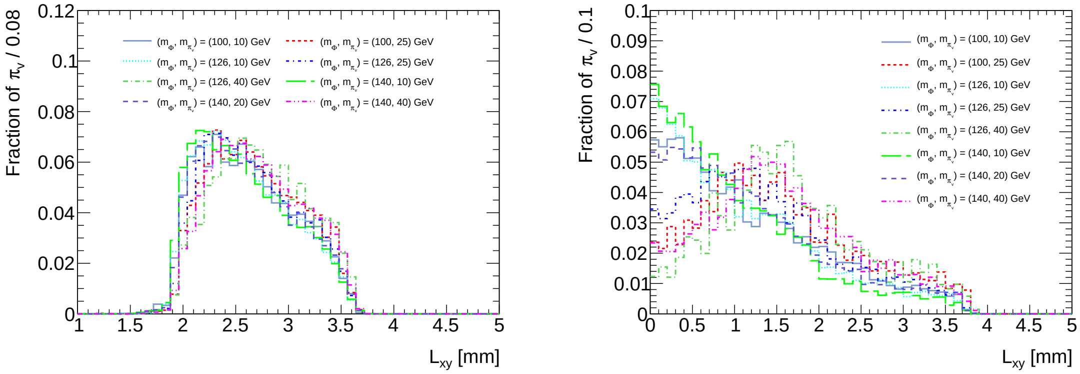

(a) Low Φ masses, triggering π_v (b) Low Φ masses, non-triggering π_v

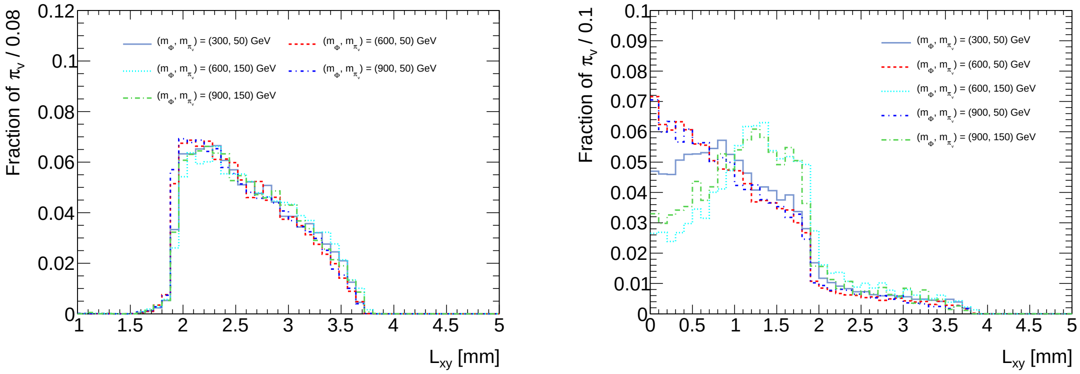

(c) High Φ masses, triggering π_v (d) High Φ masses, non-triggering π_v

Figure 5.6: Transverse decay position of the triggering and non-triggering π_v in the generated signal samples.

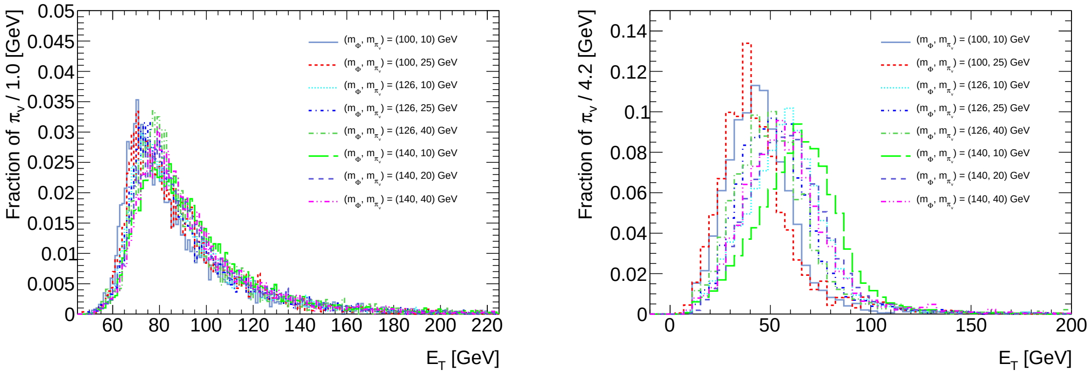

(a) Low Φ masses, triggering π_{v}

(b) Low Φ masses, non-triggering π_{v}

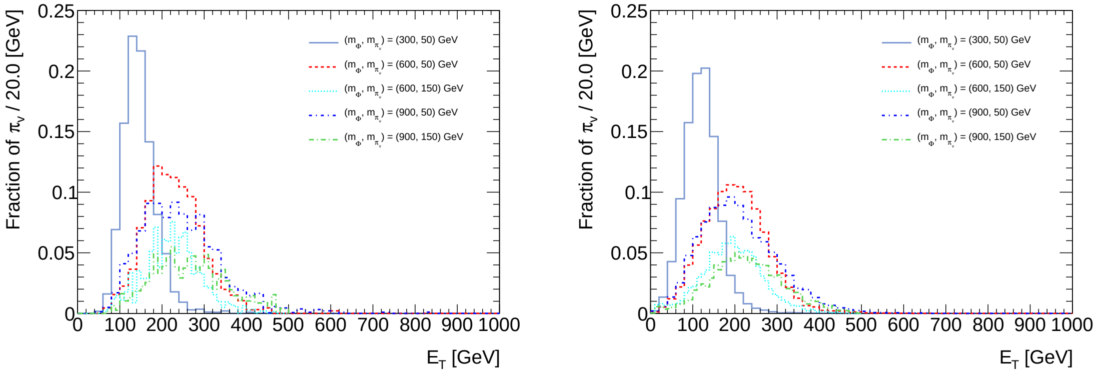

(c) High Φ masses, triggering π_{v}

(d) High Φ masses, non-triggering π_{v}

Figure 5.7: E_{T} for jets matched to the triggering and non-triggering π_{v} in the generated signal samples.

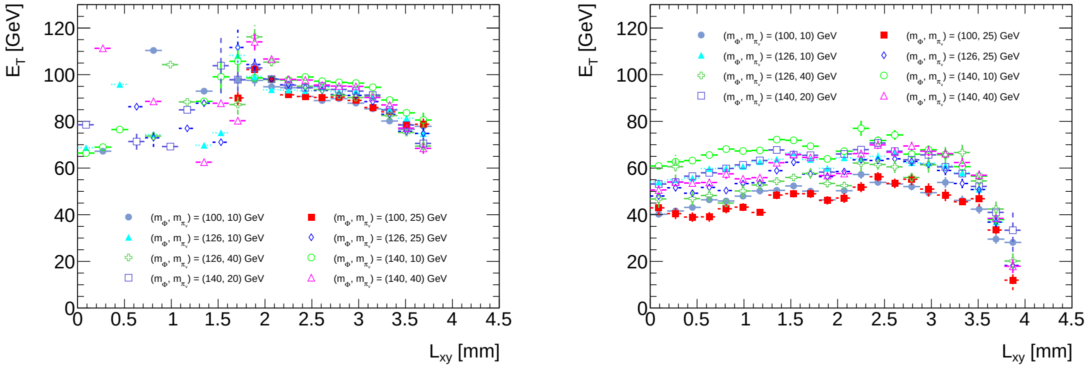

(a) Low Φ masses, triggering π_v

(b) Low Φ masses, non-triggering π_v

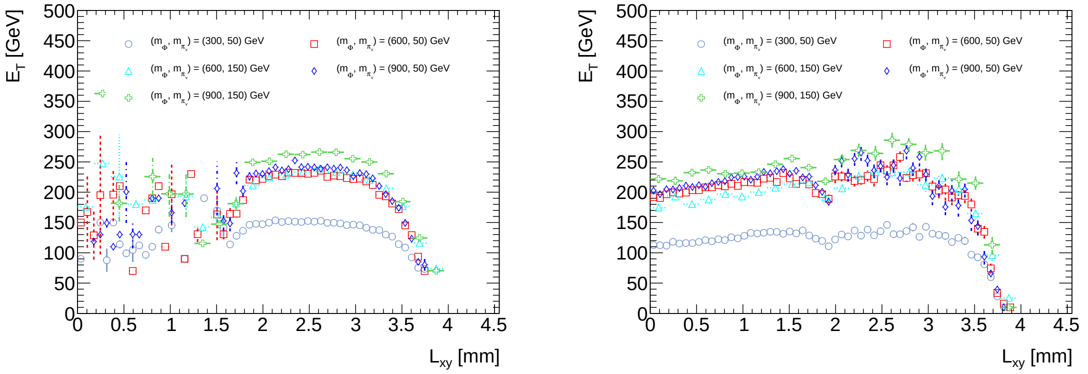

(c) High Φ masses, triggering π_v

(d) High Φ masses, non-triggering π_v

Figure 5.8: Average E_T as a function of π_v decay position for triggering and non-triggering π_v in the generated signal samples.

majority or near-majority of the time due to the neutral nature of the LLP, but because many decay before the HCal the majority produce jets with ECal energy deposits and thus low $\log_{10}(E_{\mathrm{H}}/E_{\mathrm{EM}})$. Triggering jets in general are more likely to pass these cuts given that the CalRatio trigger already contained the same cuts but applied to the HLT tracks and jets. In the case of the track cut, recommended quality criteria are used offline. To be considered, a track must satisfy Pixel hits ≥ 2 and Pixel + SCT hits ≥ 9. The final cut applied to the jets, $|\eta| < 2.5$ exists to limit the search to the fiducial region of the inner detector. The full cut flow on all signal samples are shown in Tables 5.2 and 5.2 for low mass samples and Table 5.2 for high mass samples.

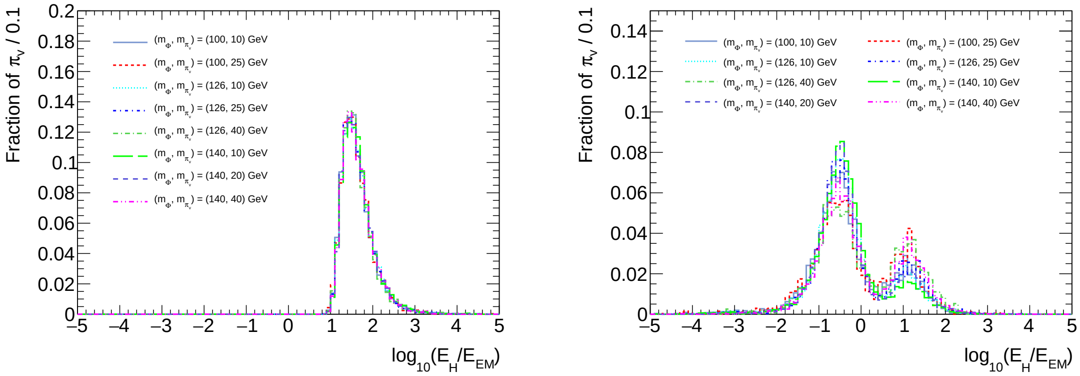

(a) Low Φ masses, triggering π_{v}

(b) Low Φ masses, non-triggering π_{v}

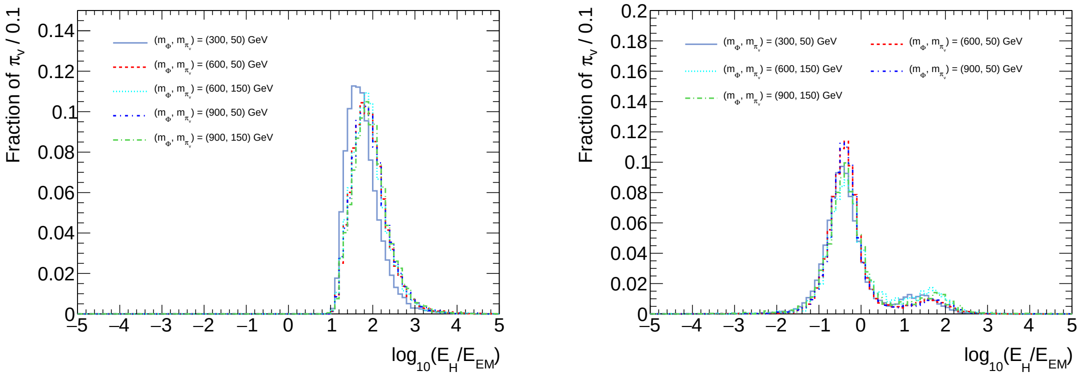

(c) High Φ masses, triggering π_{v}

(d) High Φ masses, non-triggering π_{v}

Figure 5.9: The $\log_{10}(E_{\mathrm{H}}/E_{\mathrm{EM}})$ of jets matched to triggering and non-triggering π_{v} in the generated signal samples.

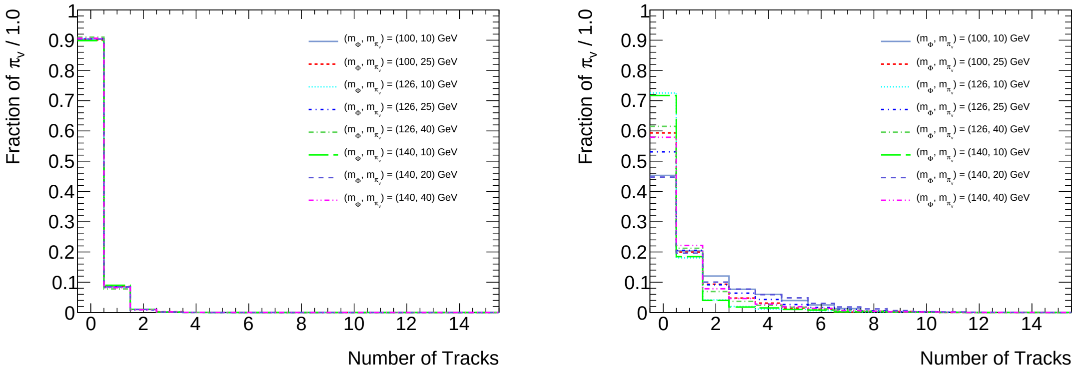

(a) Low Φ masses, triggering π_v

(b) Low Φ masses, non-triggering π_v

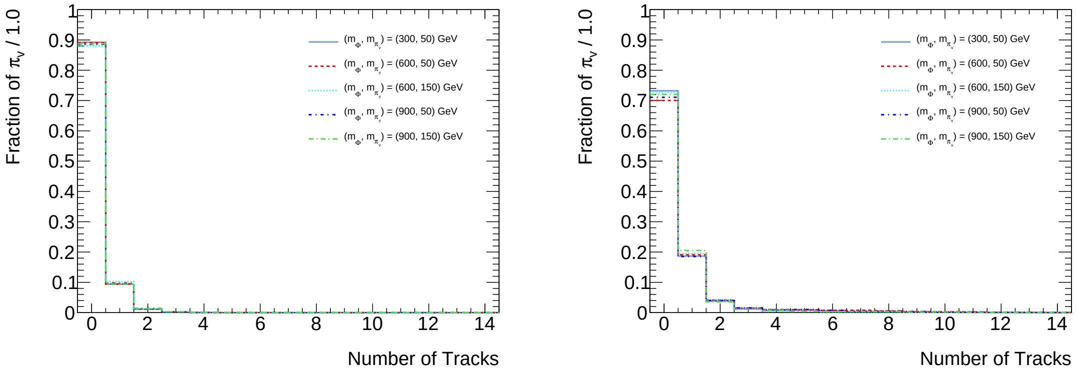

(c) High Φ masses, triggering π_v

(d) High Φ masses, non-triggering π_v

Figure 5.10: Number of ID tracks with transverse momentum higher than 1 GeV in a $\Delta R<0.2$ cone around jets matching the triggering and non-triggering π_v in the generated signal samples.

Event Selection	Events	Events	Events	Events
Signal Sample	$m_{\Phi} = 100$ GeV $m_{\pi_{\rm v}} = 10$ GeV $\pi_{\rm v}$ proper decay length = 450 mm	$m_{\Phi} = 100$ GeV $m_{\pi_{\rm v}} = 25$ GeV $\pi_{\rm v}$ proper decay length = 1250 mm	$m_{\rm H} = 126$ GeV $m_{\pi_{\rm v}} = 10$ GeV $\pi_{\rm v}$ proper decay length = 350 mm	$m_{\rm H} = 126$ GeV $m_{\pi_{\rm v}} = 25$ GeV $\pi_{\rm v}$ proper decay length = 900 mm
Processed Events	294697	295399	298899	299600
HV Trigger	9310	6185	17748	13596
Quality Requirements	9009	5949	17103	13050
$E_{\rm T}^{\rm miss}(< 50$ GeV)	6971	4694	12500	9950
Requirement on first jet				
jet with timing in (-1; 5) ns	6804	4616	12182	9783
Et > 60 GeV	6668	4538	12038	9649
Log Ratio>1.2	6231	4229	11287	9061
no track pt > 1 GeV	6054	4080	10941	8767
$\lvert\eta\rvert < 2.5$	6054	4080	10941	8767
Requirement on second jet				
jet with timing in (-1; 5) ns	5956	4043	10763	8659
Et > 40 GeV	4473	2836	9145	6726
Log Ratio>1.2	402	215	956	760
no track pt > 1 GeV	337	186	804	645
$\lvert\eta\rvert < 2.5$	334	186	794	642
Two jet topology **expected at 20.3 fb^{-1}**	**683 ± 37**	**380 ± 28**	**1022 ± 36**	**826 ± 33**

Table 5.1: Selection flow for several lower mass MC samples. The row labeled *expected* are expected number of events in 20.3 fb^{-1}, including effects due to pile-up re-weighting.

Event Selection	Events	Events	Events	Events
Signal Sample	$m_{\mathrm{H}} = 126$ GeV $m_{\pi_{\mathrm{v}}} = 40$ GeV π_{v} proper decay length = 1850 mm	$m_{\Phi} = 140$ GeV $m_{\pi_{\mathrm{v}}} = 10$ GeV π_{v} proper decay length = 275 mm	$m_{\Phi} = 140$ GeV $m_{\pi_{\mathrm{v}}} = 20$ GeV π_{v} proper decay length = 630 mm	$m_{\Phi} = 140$ GeV $m_{\pi_{\mathrm{v}}} = 40$ GeV π_{v} proper decay length = 1500 mm
Processed Events	184500	290599	281900	299699
HV Trigger	6166	21372	17929	14522
Quality Requirements	5933	20602	17299	13973
$E_{\mathrm{T}}^{\mathrm{miss}}(< 50$ GeV)	4394	15076	12810	10283
Requirement on first jet				
jet with timing in (-1; 5) ns	4281	14704	12590	10080
Et > 60 GeV	4226	14563	12448	9980
Log Ratio>1.2	3953	13729	11768	9423
no track pt > 1 GeV	3815	13246	11365	9104
$\|\eta\| < 2.5$	3815	13246	11365	9104
Requirement on second jet				
jet with timing in (-1; 5) ns	3760	13059	11211	9018
Et > 40 GeV	2722	11670	9454	7002
Log Ratio>1.2	252	1196	1070	773
no track pt > 1 GeV	206	970	882	624
$\|\eta\| < 2.5$	206	943	867	617
Two jet topology **expected at 20.3 fb^{-1}**	**430 ± 30**	**1015 ± 33**	**963 ± 33**	**645 ± 30**

Table 5.2: Selection flow for several lower mass MC samples. The row labeled *expected* are expected number of events in 20.3 fb^{-1}, including effects due to pile-up re-weighting.

Event Selection	Events	Events	Events	Events	Events
Signal Sample	m_{Φ} = 300 GeV $m_{\pi_{\mathrm{v}}}$ = 50 GeV π_{v} proper decay length = 800 mm	m_{Φ} = 600 GeV $m_{\pi_{\mathrm{v}}}$ = 50 GeV π_{v} proper decay length = 500 mm	m_{Φ} = 600 GeV $m_{\pi_{\mathrm{v}}}$ = 150 GeV π_{v} proper decay length = 1700 mm	m_{Φ} = 900 GeV $m_{\pi_{\mathrm{v}}}$ = 50 GeV π_{v} proper decay length = 500 mm	m_{Φ} = 900 GeV $m_{\pi_{\mathrm{v}}}$ = 150 GeV π_{v} proper decay length = 1300 mm
Processed Events	374173	375024	226406	372684	230111
HV Trigger	58344	73281	40405	72599	39234
Quality Requirements	55664	69400	38123	68691	36933
$E_{\mathrm{T}}^{\mathrm{miss}}$(< 50 GeV)	25676	20796	10945	18834	10178
Requirement on first jet					
jet with timing in (-1; 5) ns	25171	20176	9593	18328	9148
Et > 60 GeV	25125	20169	9589	18307	9143
Log Ratio>1.2	24633	19957	9493	18135	9060
no track pt > 1 GeV	23730	19181	9125	17445	8712
$\lvert\eta\rvert < 2.5$	23730	19181	9125	17445	8712
Requirement on second jet					
jet with timing in (-1; 5) ns	23522	19039	9048	17283	8635
Et > 40 GeV	22251	18228	8686	16394	8331
Log Ratio>1.2	3028	2661	1249	2475	1148
no track pt > 1 GeV	2335	1945	939	1822	879
$\lvert\eta\rvert < 2.5$	2263	1876	920	1769	854
Two jet topology **expected at 20.3 fb^{-1}**	**441 ± 9**	**53 ± 1**	**43 ± 1**	**6 ± 1**	**4 ± 1**

Table 5.3: Selection flow for the high mass MC samples. The row labeled *expected* are expected number of events in 20.3 fb^{-1}, including effects due to pile-up re-weighting.

5.3 Backgrounds

The two jet final state is chosen for this analysis in order to suppress background events, but does not eliminate them. Three primary contributions to the background are considered, two sources of non-collision background (NCB) and the background resulting from SM multijet events. Of these, the SM multijet background has the largest contribution to the final background estimate. Each background is separately estimated with a different method, each of which will be describe in this section.

5.3.1 Cosmic Ray Muon Background

Cosmic ray muons reaching ATLAS tend to travel in the downward direction, primarily arriving via the two access shafts (Figure 5.11). The muons are minimum-ionizing particles which traverse the detector that may bypass the ECal and ID while passing through the HCal volume. Reconstruction software is unaware of their origins and will reconstruct jets from the energy deposits they leave as if the deposits originated from the IP. These jets are therefore a background to a high $\log_{10}(E_{\mathrm{H}}/E_{\mathrm{EM}})$ jet search. As they are created independently of any proton-proton collision in the detector they arrive at a constant rate. The background estimate is determined by applying the analysis cut flow to a cosmic-specific dataset and then scaling it proportionally by luminosity to estimate the cosmic contribution to the final dataset.

The background trigger $EF\_j35\_a4tcem\_L1TAU\_LOF\_HV\_EMPTY$, which is live during empty BCs, was used to study cosmic events in isolation. This trigger is functionally identical to the collision trigger despite its lower L1 threshold because the HLT chain runs only if a $L1\_TAU40$ item is present in the event. The analysis cutflow was applied to events passing this trigger with the exception of the cut requiring a good PV and the timing cuts applied to the two jets. No PV will be present during an empty BC due to the lack of collisions. The timing cut was removed, as described below, in order to increase statistics. The cut flow for these events is shown in Table 5.4 and 5.5. The removal of the timing cut

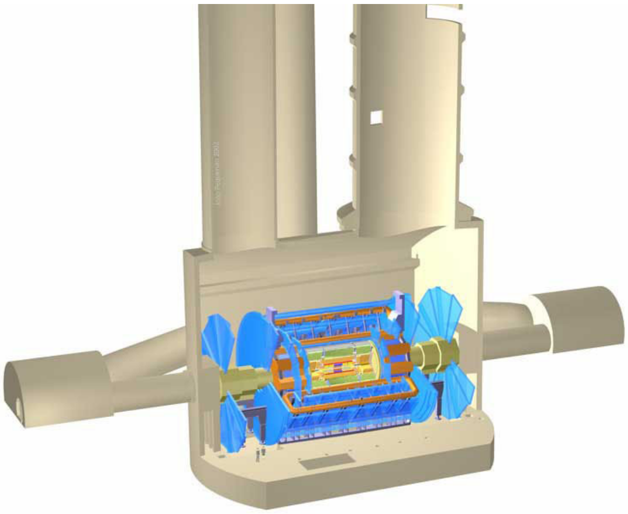

Figure 5.11: ATLAS detector and surrounding cavern [10]. Cosmic ray muons are expected to arrive through the two large access shafts.

requires an application of a correction to rescale the estimate to the narrow timing window. Further corrections are needed in order to account for differences in the numbers of empty and filled BCs during runs and to account for the lack of a collision during an empty BC cosmic event.

Cut	Number of Events
CalRatio Triggered Events	138678
No Line Of Fire Jets	130578
No DQ Flags	130394
MET ($<$ 50 GeV)	4425

Table 5.4: Event level cut flow for events firing the empty bunch crossings CalRatio trigger.

As expected, the cut on $E_{\mathrm{T}}^{\mathrm{miss}}$ results in a severe reduction in the number of remaining events in the dataset. The two jet requirement also has a severe effect on the number of pure cosmic events surviving the cut flow. Events possibly containing a single cosmic jet and a

Cut	Number of Events
Look for a Trigger Jet (first π_{v})	
Trigger object matches offline jet	3077
Jet $E_{\mathrm{T}} > 60$ GeV	2386
$\log_{10}(E_{\mathrm{H}}/E_{\mathrm{EM}}) > 1.2$	2386
No tracks with $p_{\mathrm{T}} > 1.0$	2386
Jet $\eta < 2.5$	2386
Second Jet (second π_{v})	
Jet $E_{\mathrm{T}} > 40$ GeV	6
$\log_{10}(E_{\mathrm{H}}/E_{\mathrm{EM}}) > 1.2$	4
No tracks with $p_{\mathrm{T}} > 1.0$ GeV	4
$\eta < 2.5$	4

Table 5.5: Jet selection cut flow for events firing the CalRatio empty bunch crossing trigger.

jet from another source are addressed later in this section.

Timing Correction

Timing, along with $E_{\mathrm{T}}^{\mathrm{miss}}$, have the most power in reducing NCB. Cosmic ray muons arrive at a constant rate in time, so are as likely to be present at the time of a collision as they are to arrive earlier or later. The result is a relatively flat timing distribution, as shown in Figure 5.12, shaped only by the data-taking infrastructure and the electronics of ATLAS. Signal and the SM multijet background, by contrast, are the result of the collision and have a peaked timing distribution with a slightly positive mean. The $-1 < t < 5$ ns window was chosen so as the contain most of the signal in the low mass samples while eliminating a large amount of the cosmic background.

A pure cosmic event producing two jets passing the analysis cuts will either be the result

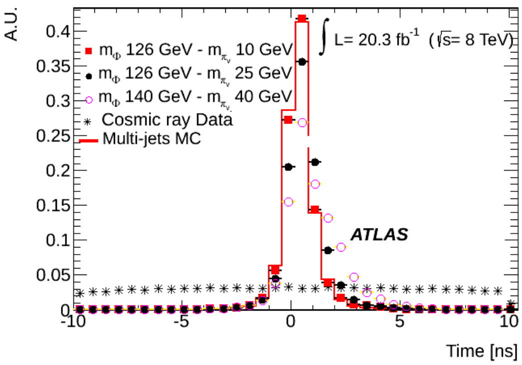

Figure 5.12: The jet timing distributions of several low mass Φ samples compared to those of the SM multijet background and the CalRatio triggered cosmic ray dataset.

of a single muon leaving jets at two different times or will result from a cosmic shower. The probability that both jets will lie within the $-1 < t < 5$ ns window is low (Figure 5.13 left-hand side). Removing the timing cut to improve the background estimate is appropriate if the other variables used in the analysis are independent of the jet's timing. This was determined to be the case and an example distribution in five time slices is shown in Figure 5.13 on the right-hand side.

Due to the uncorrelated nature of the other jet parameters to the timing in the cosmic events the scale factor to account for the lack of the timing cut in the background estimate is simply the fraction of the analyzed events with both jets in the timing window. This corresponds to 5% (147 out of 2937 events) of cosmic dijet events, or a scale factor of 0.050. Only 5% of dijet events have both jets within this region.

BC Rescaling

The next correction that needs to be applied accounts for the difference in the number of empty and filled BCs in 2012. Framed differently, this correction accounts for the different live times of the background trigger to the main CalRatio trigger. To scale the number of events from the empty BC dataset passing the cut flow to the number expected in collision

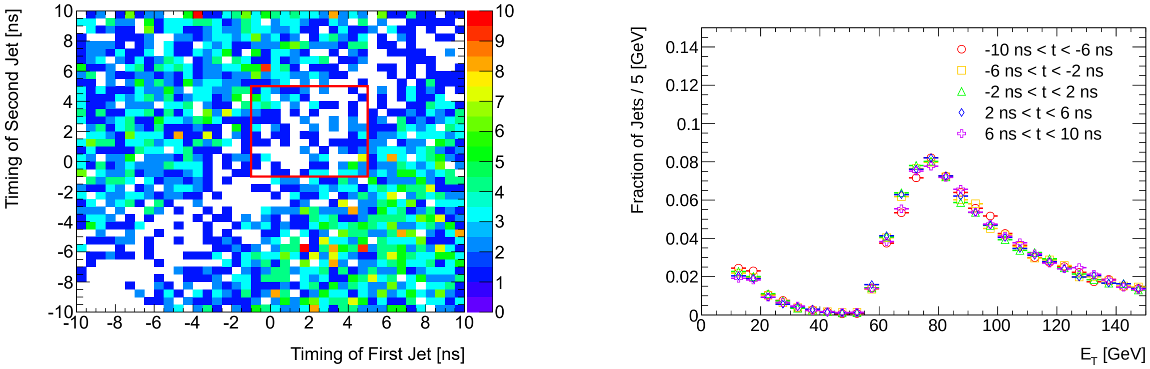

Figure 5.13: Left: The jet timing distribution of the leading and sub-leading jets in cosmic dijet events. The red square marks the boundaries of the timing cuts on the first and second jets in analysis cut flow. Right: The E_{T} distributions of jets in cosmic dijet events when partitioned into timing intervals. The jet properties were found to be independent of their jet timing.

data the ratio of the number of empty BCs with the CalRatio trigger active to the number of filled BCs with the CalRatio trigger active was calculated. To do so both the bunch group set and the prescales of the tirgger during each lumiblock is taken into account.

A typical run in 2012 several times as many filled BCs as empty ones. Figure 5.14 shows a typical bunch group set (BGS) used in 2012. Period A was an exception and contained about three times as many empty to filled BCs as other periods.

Prescaling was negligible for the primary CalRatio trigger - the trigger was prescaled for only 13 lumiblocks (less than 0.02% of 2012 total). The empty BC trigger, in contrast, was prescaled for about 5% of lumiblocks. Both the LB by LB prescaling and BGS information were extracted from the COOL database to determine the number of lumiblocks during which each trigger was active. The scale factor is determined by the ratio of active empty BCs to active filled BCs:

$$SF = \frac{Number\ of\ Filled\ Bunch\ Crossings}{Number\ of\ Empty\ Bunch\ Crossings} \tag{5.2}$$

The empty CalRatio Trigger was active for a total of 45.4×10^6 BCs, while the main

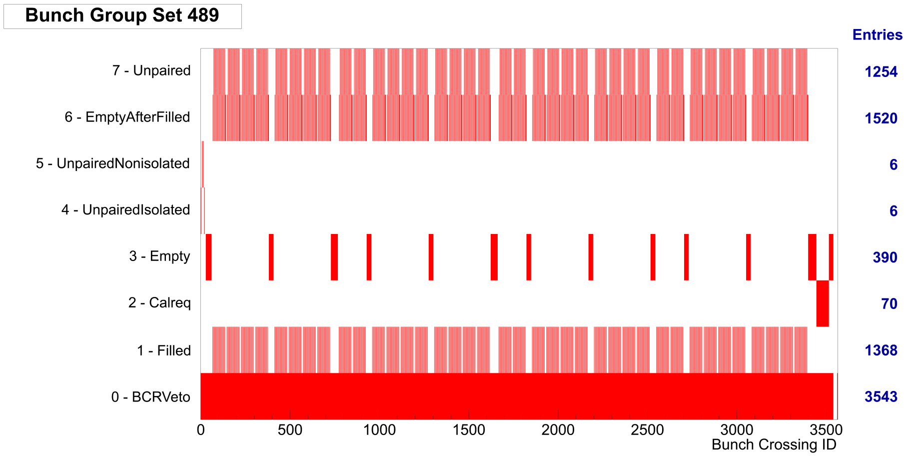

Figure 5.14: BGS 489, the typical bunch structure for LBs in which the surviving events are found. There are 390 empty BCs for every 1368 filled ones.

trigger was active for 129.7×10^6. The corresponding scale factor is 2.851.

Track Coincidence

An actual cosmic event firing the trigger during a collision and passing all cuts will necessarily have to have a collision vertex present due to the data quality criteria that events are required to pass. Such events will therefore have tracks present from the collision. One of these tracks will occasionally overlap with the cosmic jet, resulting in a failure for the jet to satisfy the tracklessness requirement.

The correction due to track coincidence was estimated using events selected by a random trigger, $EF\_J15\_passthrough{=}L1\_RD0\_FILLED$, to determine the track distribution expected from random collisions. This highly prescaled trigger passes events with at least one very low (15 GeV) energy jet and makes no other requirements. The probability of a track lying within a $\Delta R < 0.2$ cone was calculated as a function of η using the events selected by this trigger. This probability was separately calculated for each period of data taking to better account for different run conditions over the full data taking period. An example of such a probability distribution is displayed in Figure 5.15. The η values of the two jets in

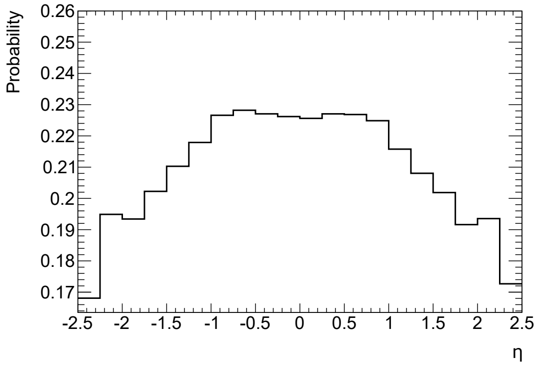

Figure 5.15: The probability as a function of η of a random track resulting in a jet failing the track isolation criteria in period C.

each event passing the full cut flow, as well as the event's period, were used to extract an event weight from the probability distributions. Only four events survived the full cut flow and their weights are listed in Table 5.6.

Event	Weight
1	0.583
2	0.626
3	0.573
4	0.545

Table 5.6: Event weights due to the η dependent probability of track coincidence with the jet.

The final estimate for the cosmic ray background, weighting each event by the track coincidence weight and applying the two scale factors, in 2012 collisions is 0.33±0.22(stat) events.

5.3.2 Beam Induced Background

Proton bunches circulating in the LHC are accompanied by a halo of muons resulting from the interactions of protons with detector elements and gas. Muons reaching the hadronic calorimeter do so traveling parallel to the beampipe and are primarily found in the horizontal plane. These muons emit bremsstrahlung radiation while passing through the calorimeter, leaving energy deposits which may be reconstructed as jets. As energy is deposited only in the HCal while the muon does not pass through the ECal or ID a large energy deposit may be reconstructed as a trackless, low EMF jet. This topology of this Beam Induced Background (BIB) was discussed in more detail in Section 5.1.2.

Both the $E_{\mathrm{T}}^{\mathrm{miss}}$ cut and the dedicated Line of Fire cuts dramatically reduce the amount of BIB surviving the cut flow. Pure BIB events passing the $E_{\mathrm{T}}^{\mathrm{miss}}$ cut are unlikely to be the result of a single BIB muon. Such events normally result from a pair of BIB muons on opposite sides of the detector.

A sample of BIB events were gathered using the dedicated trigger running on unpaired isolated BCs: $EF\_j35\_a4tcem\_L1TAU\_LOF\_HV\_UNPAIRED\_ISO$. When the full analysis cut flow is applied to these events none pass the full set of cuts. This is partially due to the very small number of unpaired isolated BCs in each BGS (Figure 5.14) and partially due to the effectiveness of the Line of Fire and $E_{\mathrm{T}}^{\mathrm{miss}}$ cuts. Only 80 of the 3046 triggering events pass the $E_{\mathrm{T}}^{\mathrm{miss}}$ cut.

The background estimate cannot be taken as 0 given the very large size of the scale factor that would account for the difference in the number of unpaired isolated to filled BCs in 2012 as well as the smaller scale factor accounted for cosmic contamination of the unpaired isolated CalRatio triggered events. Instead, an alternative method was developed to account for these obstacles by assembling a library of single jets from the dataset and building possible events from these jets. The procedure is summarized as follows:

- Determine the probability per bunch crossing for a single BIB jet to fire the trigger and satisfy the data quality cuts, including not being identified by the LoF cuts as a

BIB event. The jet must pass all cuts applied to first jet in the cut flow.

- Square the probability to determine the probability per bunch crossing that two such jets will independently exist in any event. Scale that by the number of filled bunch-crossings in 2012.
- Apply a correction based on the probability that an event with two such jets will pass the $E_{\mathrm{T}}^{\mathrm{miss}}$ cut.
- Apply a correction based on the probability that no tracks in a collision event will ruin the isolation criteria for either jet.

Probability That a Single BIB Jet Passes Jet Cuts

The probability per BC for a BIB jet to fire the trigger and pass all jet requirements, P_{BHJet}, is determined by applying the analysis cut flow for only the first jet, without the event level $E_{\mathrm{T}}^{\mathrm{miss}}$ cut, to the unpaired isolated CalRatio triggered events. The probability can naively be expressed as:

$$P_{\mathrm{BIBJet}} = \frac{N_{\mathrm{BIBJetsPass}}}{N_{\mathrm{UnIso}}}. \tag{5.3}$$

Here $N_{\mathrm{BIBJetsPass}}$ is the number of jets passing these cuts while N_{UnIso} is the number of events in which the CalRatio background trigger was active. This is a naive expression because it fails to account for the presence of cosmic ray induced events in the unpaired isolated sample. The contamination is actually very large but straightforward to estimate.

The cosmic contamination is estimated by first determining the analogous P_{CosJet} and then applying it to the number of unpaired isolated BCs, N_{UnIso}. For P_{CosJet} we have:

$$P_{\mathrm{CosJet}} = \frac{N_{\mathrm{CosJetsPass}}}{N_{\mathrm{Empty}}}. \tag{5.4}$$

Following the template of the analogous BIB variable, $N_{\mathrm{CosJetsPass}}$ is the number of jets form the empty BC dataset passing the cut flow through the cuts on the triggering jet and without the event level $E_{\mathrm{T}}^{\mathrm{miss}}$ cut. N_{Empty} is the number of BCs in which the empty BC CalRatio trigger was active. The number of events surviving each stage of this cut flow for both triggers is summarized in Table 5.7. The resulting probabilities for cosmic ray induced jets is $P_{\mathrm{CosmicJet}} = (4.97 \pm 0.03) \times 10^{-4}$. When the number of expected cosmic events is subtracted from the BIB P_{BHJet} can be more accurately determined: $P_{\mathrm{BHJet}} = (6.3 \pm 2.9) \times 10^{-5}$.

Cut	Unpaired Isolated Events	Empty Events
Triggered Events	3046	138678
No Line Of Fire Jets	2480	130578
No DQ Flags	2476	130394
Trigger object matches offline jet	1451	83129
$-1ns < t < 5ns$	440	26346
Jet $E_{\mathrm{T}} > 60$ GeV	435	25920
$\log_{10}(E_{\mathrm{H}}/E_{\mathrm{EM}})$ >1.2	431	25898
No tracks with $p_{\mathrm{T}} > 1.0$	431	25894
Jet $\eta < 2.5$	431	25894
Single Jet Event	374	22581

Table 5.7: Modified cut-flow used to determine single jet probabilities. Unpaired isolated bunch-crossings contain both BIB and cosmic ray events while empty bunch-crossings are isolated from beam backgrounds.

Probability of a Two BIB Jets Satisfying $E_{\mathrm{T}}^{\mathrm{miss}} < 50$ GeV *in Same Event*

Squaring P_{BHJet} gives the probability of two BIB muons independently leaving jets passing the full cut flow in absence of the $E_{\mathrm{T}}^{\mathrm{miss}}$ cut. To estimate the frequency such an event would also pass the $E_{\mathrm{T}}^{\mathrm{miss}}$ cut, pairs of jets passing the modified cut flow are combined to create toy events and the resulting $E_{\mathrm{T}}^{\mathrm{miss}}$ due to the jet pair is reconstructed. To avoid the high level of cosmic contamination when studying the $E_{\mathrm{T}}^{\mathrm{miss}}$ cut the probability P_{PassMET} is determined with a library of jets composed of those from the unpaired isolated triggered events that *fail* the LoF cut.

This library of jets is collected with the same modified cut flow, except for the removal of the LoF cut, as was used to determine P_{BHJet} and $P_{\mathrm{CosmicJet}}$. The probability for a toy event to pass the $E_{\mathrm{T}}^{\mathrm{miss}}$ cut is:

$$P_{\mathrm{PassMET}} = \frac{N_{\mathrm{PassMET}}}{N_{\mathrm{ToyEvents}}} \tag{5.5}$$

Here, $N_{\mathrm{ToyEvents}}$ is the total number of toy events created from the library of jets and N_{PassMET} is the number that satisfy $E_{\mathrm{T}}^{\mathrm{miss}} < 50$ GeV. The resulting probability is found to be: $P_{\mathrm{PassMET}} = 0.24 \pm 0.02$ (stat).

There is a mismeasurement in this $E_{\mathrm{T}}^{\mathrm{miss}}$ because it only considers the combined p_{T} of the jet pair. This introduces a systematic error into the calculation. To calculate the systematic the p_{T} of the jets in the toy event was shifted upwards and downward by the mean difference between the $E_{\mathrm{T}}^{\mathrm{miss}}$ and jet p_{T} in a single-jet events firing the primary CalRatio trigger. The systematic is half the difference in the resulting probability when all jets' p_{T} are shifted upward and when all are shifted upwards, resulting in a 7% systematic: $P_{\mathrm{PassMET}} = 0.24 \pm 0.03$ (stat+sys).

Combining Probabilities

The probability that a random track will ruin the track isolation criteria, P_{PassIso}, is also calculated. A precise determination is tedious and unnecessary given the small size of the expected background. Instead, the average value of the track isolation weights from the cosmic events is taken as the probability: $P_{\mathrm{PassIso}} = 0.6$.

The final probability is:

$$N_{\mathrm{BH}} = P_{\mathrm{BHJet}}^{2} * N_{\mathrm{Filled}} * P_{\mathrm{PassMET}} * P_{\mathrm{PassIso}} \tag{5.6}$$

The background prediction is determined to be 0.07 ± 0.07 events.

5.3.3 SM Multijet Background

The analysis cut flow was developed primarily to isolate signal from the SM multijet background. It is nonetheless possible for a SM jet to fluctuate to contain only neutral hadrons, mimicking a signal jet. The SM multijet cross-section is large enough that even if such jets have a low probability of resulting from a collision they will be seen at a high enough rate to affect the background. The SM multijet background results in the majority contribution to the multijet background due to this fact.

It is not possible to estimate the background on the MC sample due to the low statistics for signal-like jets. The background estimate uses a data driven tag-and-probe method using the full 2012 SM multijet dataset. Probabilities for single jets to pass the analysis cuts are determined and in turn combined into event probabilities to determine the full background prediction. The procedure can be summarized as follows:

- The probability of a single Standard Model QCD jet to pass the analysis and trigger cuts, as a function of jet E_{T} and jet η, is derived.
- The single jet probabilities are combined into an event probability using a simple combinatoric calculation.
- The events in the QCD data sample are weighted by their event probability and prescale and are summed to determine the the uncorrelated background prediction.
- A scale factor, determined in data is applied to the uncorrelated background prediction in order to account for 2-jet correlations.

Calculation of Single-Jet Probabilities

The full analysis cut flow (Section 5.2) requires two jets to pass a series of analysis cuts. Most cuts are the identical between jets but one jet is required to match the CalRatio trigger object

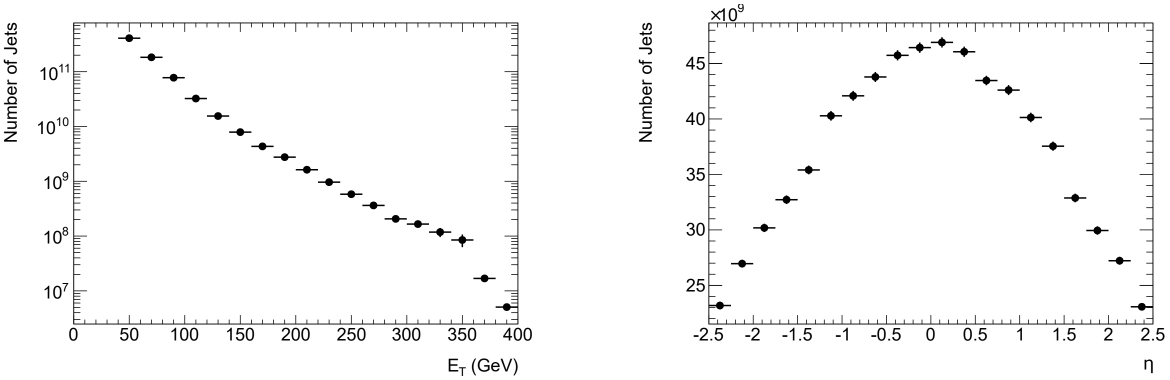

Figure 5.16: Probe jet E_{T} (left) and η (right) after application of the event prescales.

and pass a 60 GeV E_{T} cut while the other has no trigger requirement and need pass only a 40 GeV E_{T} cut. Two different single jet probabilities are determined:

- P - the probability for a jet to pass all jets cuts including the trigger and 60 GeV E_{T} cut

- Q - the probability for a jet to pass all jets cuts including the 40 GeV E_{T} cut but with no trigger requirement

These probabilities are determined with data collected using the single-jet triggers EF_j15 through EF_j460. All event level cuts are applied and the highest E_{T} jet in each event is identified as the *tag* jet while the second highest E_{T} jet identified as the *probe* jet. Additionally $\Delta\phi(\text{tag jet}, \text{probe jet}) > 2.0$ is required to increase the purity of the dijet sample. Jets must also satisfy the GoodHVMedium quality jet criteria as well as have $E_{\mathrm{T}} > 40$ GeV, $|\eta| < 2.5$, and $|timing| < 5$ ns. To improve statistics and account for the contribution to probabilities from leading jets the tag and probe jets are then swapped. The E_{T} and η distributions of the full set of probe jets is shown in Figure 5.16. Prescales weights have been applied for the single jet triggers.

The probability P is the fraction (as a function jet E_{T} and η) of probe jets satisfying firing the CalRatio trigger and passing all cuts placed on the triggering jet. Q is the fraction of probe jets passing all cuts placed on the second jet. A jet that is included in the numerator when calculating P is necessarily included for Q as well. Determining simultaneously the E_{T} and η dependence of P or Q is not possible due to the low statistics present in the dataset. Instead, the dependence on E_{T} is calculated by averaging over jet η and vice versa. It is assumed that E_{T} and η are uncorrelated, allowing Equation 5.7 to be used to determine the combined dependence. A systematic corresponding to the assumption that the two variables are uncorrelated is calculated and is discussed later in this section.

$$\begin{aligned} P(E_{\mathrm{T}},\eta) &= P(E_{\mathrm{T}})P(\eta)/ < P > \\ Q(E_{\mathrm{T}},\eta) &= Q(E_{\mathrm{T}})Q(\eta)/ < Q > \end{aligned} \tag{5.7}$$

The probability $P(E_{\mathrm{T}})$ is additionally calculated separately for leading and sub-leading jets. Studies on MC suggest that this is at least partially due to differences between quark initiated and gluon initiated jets, the former of which is more likely to be the leading jet in a mixed dijet event. $P(\eta)$ is not determined separately for leading and sub-leading jets as no substantial difference was observed for η distributions. The separation is furthermore not performed for Q because a correction developed to address an additional correlation between jet pairs simultaneously corrects for the leaving and sub-leading jet correlation. The calculated distributions for P and Q are shown in Figure 5.17.

The turn on in $P(E_{\mathrm{T}})$ is a result of the CalRatio trigger requirement, which turns on around 60 GeV. Both P and Q fall off at higher E_{T} as the isolation criteria are less likely to be satisfied. Landau distributions are used to fit the $P(E_{\mathrm{T}})$ distributions while Q is fit to a decaying exponential. These fits can be seen in Figure 5.18 and Figure 5.19. The fit for $P(E_{\mathrm{T}})$ is permitted to use jets with $E_{\mathrm{T}} < 60$ GeV to improve the fit, although the applied P is still equal to zero for such low E_{T} jets. No fits are preformed for the η distributions as their shape is largely determined by the geometry of ATLAS.

Statistical errors must be propagated when the P and Q functions are used. In the case of the η component, where no fit is performed, the errors are taken directly from the

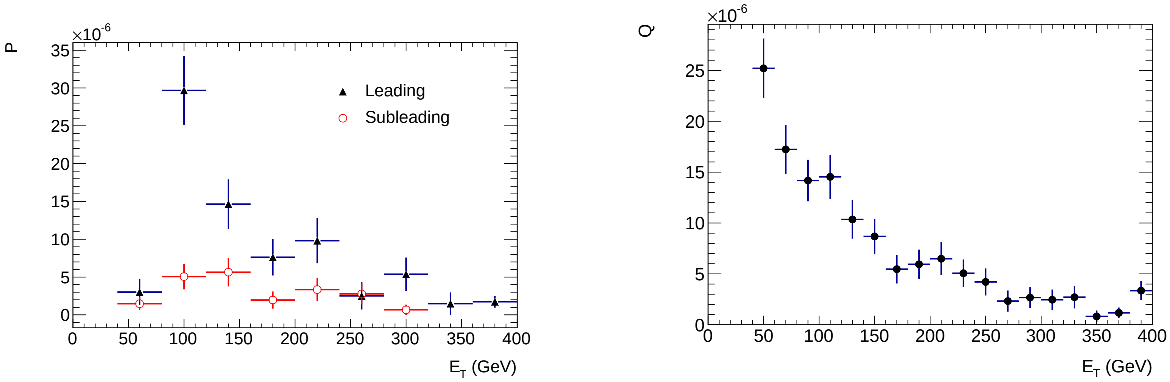

(a) P_{Leading} and $P_{\text{Subleading}}$ as functions of E_{T}

(b) Q as a function of E_{T}

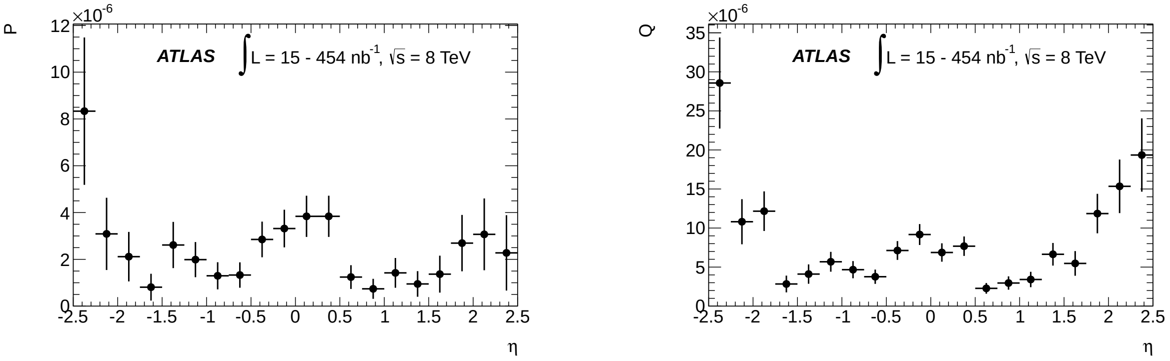

(c) P as a function of η

(d) Q as a function of η

Figure 5.17: P (left) and Q (right) plotted as a function of jet E_{T} (top) and jet η (bottom).

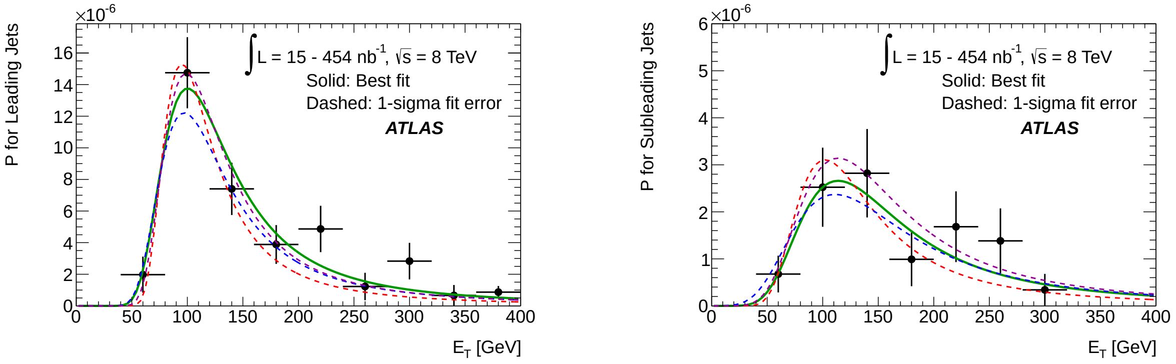

Figure 5.18: P_{Leading} (left) and $P_{\text{Subleading}}$ (right) are plotted as a function of jet E_{T} and fit to Landau distributions. P's fit function is allowed to extend below the offline cut of 60 GeV in order to include more data points in the fit. Errors on the fit parameters are used to derive new fit functions (dotted lines), which are used to determine the error in the prediction due to the fit error.

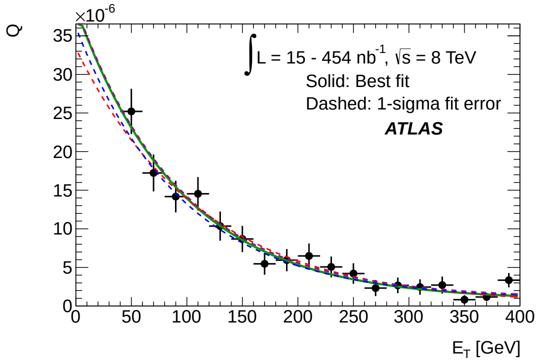

Figure 5.19: Q is plotted as a function of jet E_{T} and fit to a decaying exponential. Errors on the fit parameters are used to derive new fit functions (dotted lines), which are used to determine the error in the prediction due to the fit error.

histogram statistics. For the E_{T} components the fit errors are used to derive one-*sigma envelope* functions. These functions are the dashed lines seen in Figure 5.18.

The procedure for determining the envelope functions uses the eigenvector method to obtain one envelope function per fit parameter. The original fit parameters are correlated - shifting one by one-σ will affect the others. To simplify the procedure, the covariance matrix associated with the fit function is diagonalized, yielding a set of uncorrelated fit parameters related to the originals by the eigen vectors. To obtain each envelope function a single uncorrelated fit parameter is shifted by its uncertainty and the new envelope function is calculated.

The separate component distributions and their uncertainties are then used to determine a single jet probability P and single jet probability Q for every jet in an event. This probability is a measure of how likely such a jet is, given only its E_{T}, η, and leading jet status, to pass the CalRatio analysis cuts. To determine the likelihood of the whole event satisfying the CalRatio analysis cuts the single jet probabilities must be combined into an event probability.

Event Probability

To the determine the probability of any given SM multijet event to pass all the analysis criteria the single jet probabilities are combined event by event using Equation 5.8:

$$Prob(N_{\mathrm{j}}) = \sum_{m=1}^{N_{\mathrm{j}}} \sum_{n=m+1}^{N_{\mathrm{j}}} [P(j_m)Q(j_n) + P(j_n)Q(j_m) - P(j_m)P(j_n)] \prod_{\substack{k=1\\k\neq n\\k\neq m}}^{N_{\mathrm{j}}} (1 - Q(j_k)) \tag{5.8}$$

In this equation N_{j} is the number of jets passing the probe jet criteria (used to determine the denominator of P and Q) and the labels j_m and j_n refer to pairs of jets in the event and their E_{T}, η, and whether the jet is a leading jet in the case of P. The term $-P(j_m)P(j_n)$ is added to prevent the double counting of jet pairs when both jets satisfy the criteria for P. Finally, the $\prod$ term enforces the requirement that precisely two jets satisfy the criteria.

The number of events due to the SM multijet background is then:

$$N_{QCD} = \sum_{\text{Each event passing EF\_j15}} Prob(N_{\text{j}}) \times Prescale \tag{5.9}$$

Here events are summed which satisfy the requirements applied for the denominator of P and Q and prescales are applied to properly weight events. The full 2012 multijet dataset is used to perform the sum.

Scale Factor due to Jet-Jet Correlations

In the method used to calculate P and Q, the two probabilities are determined independently of one another. It was found, however, that a correlation in jet properties exists between two jets in the same event. This is at least partially due to the parton flavor of the initiating jet. In SM dijet events in the jet E_{T} containing the majority of events contributing to the background estimate, the breakdown of the flavors of the jet pairs is roughly ∼10% $q\bar{q}$, ∼40% qg, and ∼50% gg. The CalRatio trigger possess different pass rates for quark and gluon initiated jets, biasing the the flavor composition of the second jet (it will select $q\bar{q}$ and qg events more often than gg events). The bias of the trigger is a result of correlations between $\log_{10}(E_{\text{H}}/E_{\text{EM}})$, the number of tracks associated with the jet, and jet flavor for quark versus gluon jets. This means that altering the distribution, or failing to alter the flavor composition in this case, of jets in which Q is calculated will result in an incorrect value for Q.

Low statistics for signal-like jets in data prevent the possibility of calculating P and Q simultaneously. Instead, a scale factor, SF, is calculated to correct for this correlation. SF is calculated by determining its value outside of the signal region and extrapolating to determine the appropriate scale factor within the signal region.

The calculation of SF makes use of two variables, the number of tracks associated with the jet and the jet EMF. EMF is used rather than $\log_{10}(E_{\text{H}}/E_{\text{EM}})$ because it ranges between 0 and 1, allowing for easy binning. The analysis cut of $\log_{10}(E_{\text{H}}/E_{\text{EM}}) > 1.2$ corresponds to $EMF < 0.056$. The track quality cuts applied for the normal analysis track veto are also applied when determining nTracks. The EMF-nTracks plane is binned into multiple regions to allow the calculation of the scale factor in several regions. Each bin corresponds to a pair of cuts: an upper and lower limit EMF and the precise number of tracks counted for nTracks. These are the cuts to be applied to the second jet in an event with the first jet still being determined by trigger matching.

In each bin the standard analysis cutflow is applied to the main CalRatio dataset, but with the EMF ($\log_{10}(E_{\mathrm{H}}/E_{\mathrm{EM}})$) and track cut replaced with that corresponding to the cuts indicated by the bin. This determines N_{data}, the number of events observed in the CalRatio triggered data. The SM multijet background estimation described above is also performed, with the modified cuts used to determine that bin's Q. This new Q is used to calculate N_{QCD}, the number of background events expected from QCD process, i.e. the SM multijet background. The ratio of these two is the SF needed in that bin to correct the SM multijet background prediction to fit that observed in the the CalRatio triggered dataset.

The SF trend is determined as a function of both EMF and nTracks. First, the EMF cut on the second jet is held at $0.55 < \mathrm{EMF} < 0.65$ while a series of nTracks cuts are performed. Then, the nTracks cut is held at $5 \leq \mathrm{nTracks} \leq 6$ while a series of EMF cuts are performed. The EMF bin in which to place the nTracks axis was chosen by determining in MC the EMF bin in which a quark-initiated jet had the same probability of occupying as a gluon-initiated jet. The nTracks bin intersected by the EMF axis was chosen the same way. Each "axis" is then extrapolated into the signal region.

This method includes an obvious cross check - the combined SF can be calculated in various off-axis bins and compared to the one that is found by taking the ratio as was cone of the on-axis bins. A ratio of the probability distributions is shown in black in Figure 5.20. The same figure shows in red the ratio of observed to predicted events, which gives the scale factor for that region. When a quark jet is just as likely as a gluon jet to satisfy the cuts in the bin, the correction needed is very small (the ratio is nearly equal to 1). The greater the deviation between quark and gluon jets, the larger the local SF will need to be to correct the prediction.

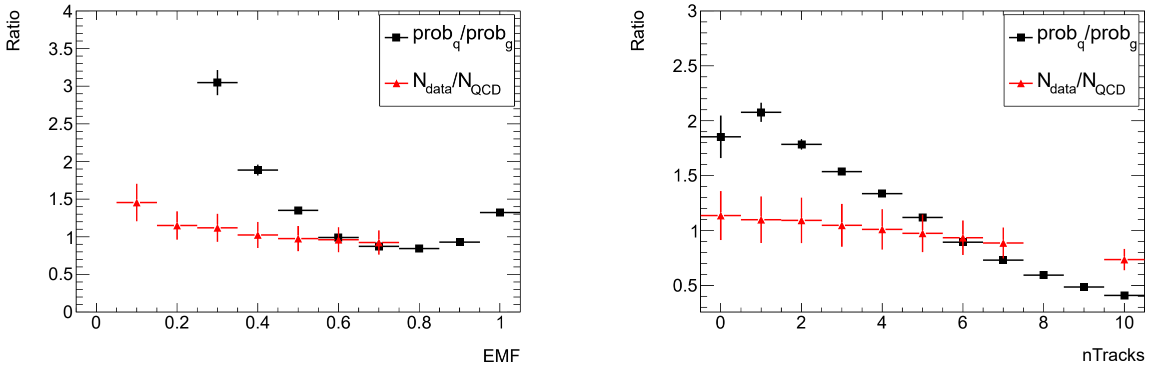

Figure 5.20: The ratio of the number of events observed in data versus the number predicted for the QCD background, $N_{\mathrm{data}}/N_{\mathrm{QCD}}$, overlayed with $\mathrm{prob_q}/\mathrm{prob_g}$ for EMF (left) and nTracks (right). An increasing deviation in the q-g ratio from a value of 1 predicts an increasing in the ratio $N_{\mathrm{data}}/N_{\mathrm{QCD}}$. $N_{\mathrm{data}}/N_{\mathrm{QCD}}$ was not calculated for all bins, but for only those between the signal region and where $\mathrm{prob_q}/\mathrm{prob_g}$ is close to 1. These bins are sufficient to fit and extrapolate into the signal region. An additional point for nTracks= 10 was added to observe the trend in $N_{\mathrm{data}}/N_{\mathrm{QCD}}$ for a value of nTracks above those where $\mathrm{prob_q}/\mathrm{prob_g}$ is near 1.

This method assumes there is no correlation between the EMF and nTracks axes when calculating the scale factor. A correlation does exist between the EMF and nTracks of a jet in general, as shown in Figure 5.21. Low EMF jets are more likely to have a small number of tracks. However, this correlation is taken into account when Q is calculated in each bin. N_{QCD} therefore implicitly accounts for this single-jet EMF and nTracks correlation. Any residual correlation would result in a failure of the cross-check described below.

In the absence of a correlation between axes the SF for any EMF-nTracks bin is simply the product of the two contributions:

$$SF(EMF, nTracks) = SF(EMF)|_{nTracks==5||nTracks==6} * SF(nTracks)|_{0.55<EMF<0.65} \tag{5.10}$$

The extrapolation into the signal region is performed independently along the two axes. The EMF, unlike nTracks, is not discrete. The reference value used for the EMF if instead

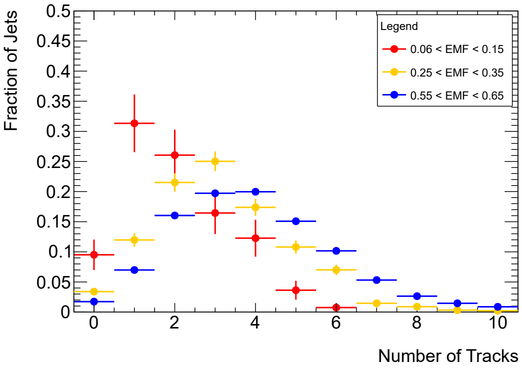

Figure 5.21: The number of tracks for different ranges of EMF. The usual data quality, MET, and $E_{\mathrm{T}} > 40$ GeV, $|\eta| < 2.5$, and $|timing| < 5$ ns jet cuts were applied and all events pass the EF_j15 trigger.

taken as the mean EMF of the tag and probe jets in that bin, $EMF = 0.04138$. The value for SF(EMF) and SF(nTracks) is taken from a quadratic fit on the $N_{\mathrm{data}}/N_{\mathrm{QCD}}$ histograms shown in Figure 5.20. The calculated scale factors are:

- SF(EMF=0.04138) = 1.503 ± 0.377

- SF(nTracks=0) = 1.168 ± 0.110

The combined scale factor is 1.76 ± 0.47. The large errors in both SF and the fits result mostly from the errors in the fits performed during the SM multijet background estimation in each bin. The Landau fits result in the largest contribution at each data point.

Applying the SM multijet background method, before application of the scale factor, to the full 20.3 fb^{-1} 2012 datasets yields a predicted background of 13.23 events. The majority of the contribution to this estimate comes from events with lower jet multiplicity, as can be seen on the right in Figure 5.23. Low multiplicity events are more numerous, as can be seen on the left of the same figure, but are also cleaner, making the track isolation more likely to be met.

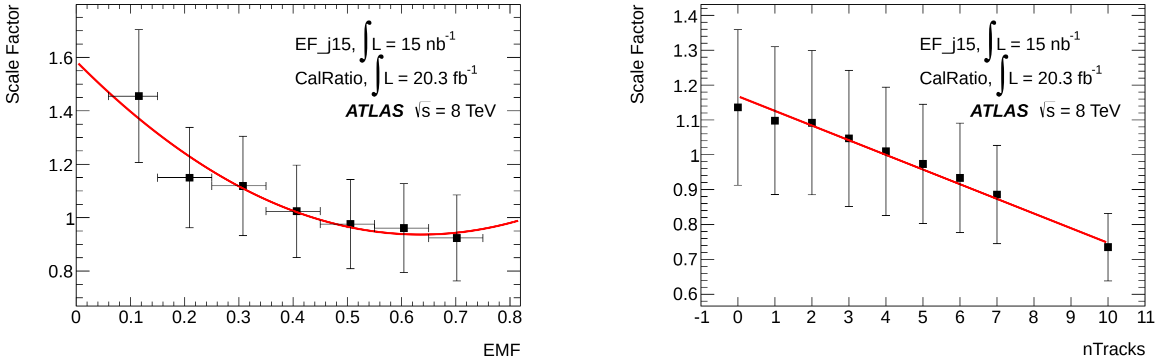

Figure 5.22: The ratio of the number of events observed in data versus the number predicted for the QCD background, $N_{\rm data}/N_{\rm QCD}$, is fitted to allow the determination of the scale factor contributions from EMF (left) and number of tracks (right). The datapoints in the EMF histogram are located in EMF at the mean value of each bin as determined from the EMF profile in that bin.

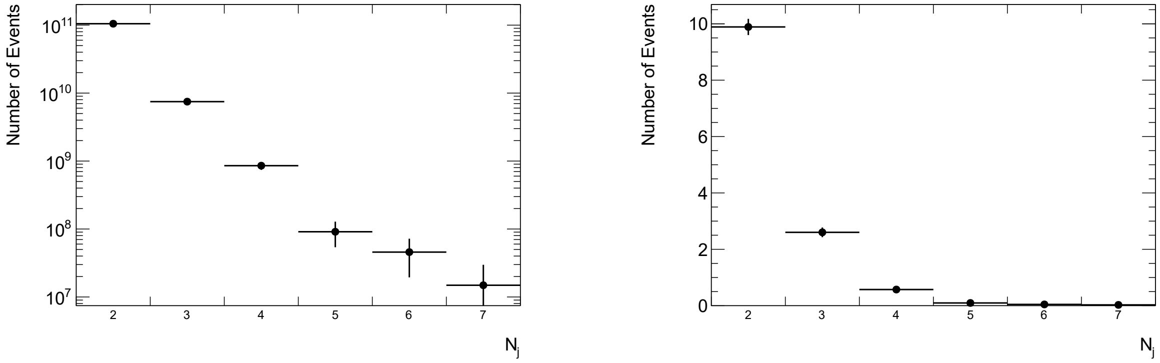

Figure 5.23: The number of predicted SM multijet events per $N_{\rm j}$ bin (left) containing $N_{\rm j}$ jets passing $E_{\rm T} > 40$ GeV, $|\eta| < 2.5$, and $|timing| < 5$ ns, and the predicted SM multijet background per $N_{\rm j}$ bin (right). The errors shown are those associated with $\sqrt{N}$ statistics. The EF_j15 trigger was used to select events.

There are three statistical uncertainties associated with the background prediction. The first is due to the uncertainty in the fits for P and Q. This is the dominant component at 2.71 events. The second uncertainty, the contribution from $P(\eta)$ and $Q(\eta)$, is only 0.23 events. It is determined by varying the value in each bin in Figure 5.17 according to normal distributions with widths equal to the bin's error and observing the variance in the final prediction. The final error is due to the number of predicted events in each bin, seen in Figure 5.23 on the left, and is determined to be 0.13 events.

The statistical and systematic errors are separately added in quadrature, yielding a prediction (before application of SF) of 13.23 ± 2.72 (stat) ± 0.95 (syst) events. Application of the scale factor brings this to 23.24 ± 8.03 (stat+syst) events. Several cross-checks are applied to test the validity of various stages of the SM multijet background prediction procedure and thus the final prediction.

Events passing the EF_j15 trigger were used when applying P and Q. To cross-check the estimate of number of events per N_{j} bin which contain N_{j} jets passing the tag and probe cuts the procedure was repeated using several other triggers: EF_j15, EF_j25, EF_j35, and EF_j55. The integrated luminosity of the EF_j15, EF_j25, EF_j35 and EF_j55 triggers is, respectively, 14.78, 78.70, 454.11, and 443.24 nb^{-1}, increasing with decreasing average prescale. These numbers are heavily dependent upon the proper application of the trigger prescales. The results are shown in Figure 5.24. The three lowest triggers, EF_j15, EF_j25, EF_j35, all have E_{T} thresholds sufficiently below that for the tag-and-probe definition that the results are in good agreement. The EF_j55 is also included in Figure 5.24 is also included for comparison despite its higher E_{T} threshold.

Figure 5.24 also shows the predicted background for each of these triggers, before application of the scale factor, on the right-hand side. All triggers are sufficiently below the 60 GeV analysis cut used on the triggering jet that the predicted number of events should be in agreement. Were agreement found between triggers in the case of the first plot but not the second would suggest a problem in the calculation or application of P and Q. Agreement is found within less than 0.5 events.

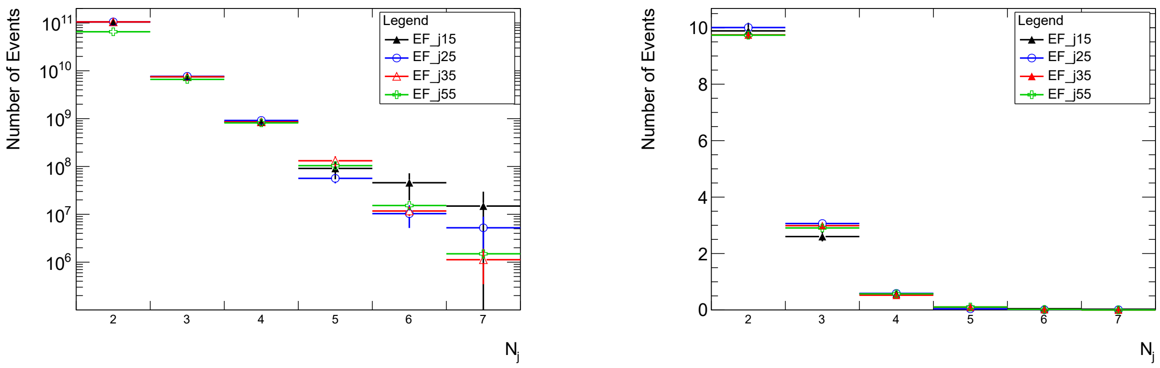

Figure 5.24: The number of predicted SM multijet events per N_j bin (left) containing N_j jets passing the looser offline cuts, and the predicted SM multijet background per N_j bin (right). The errors shown are those associated with $\sqrt{N}$ statistics. Results for events selected using different triggers are compared.

As a second cross-check on P a series of closure and similar tests are performed. Applying P to the same dataset on which is was calculated should return the exact number of events with a jet firing the CalRatio trigger and passing the analysis cuts applied to that jet. Increasing the complexity of the P calculation away from closure test can be used to test the robustness of the calculation of P. The following tests were performed:

- Using the raw P histograms rather than the fits, estimating the degree to which the fits effect the prediction. In this test the $P(E_\mathrm{T})$ histograms are used without fitting, just as the $P(\eta)$ histograms already are in the normal background calculation. However the η histograms are not used at all and no averaging is performed. Applying P to the original tag-and-probe dataset it was calculated from returns almost exactly the actual number of events passing P's requirements, as it should.

- The same test is repeated with the η histograms and averaging procedure included. The leading jet estimate is less than 3% off the actual value while the sub-leading jet estimate is less than 2% off.

- In the next test $P_\mathrm{subleading}$ is applied to jets that are neither the leading or sub-leading jets. These jets are excluded from the calculation of $P_{\text{subleading}}$ because they are never taken as probe jets. In this case the estimation is off by 24%. The discrepancy is large, but in the full analysis the number of jets used in the estimation which are neither leading nor sub-leading is very small, so this discrepancy has a minimal impact on the actual analysis.

- For the next test the fit was again applied for P. For both the leading and sub-leading jet this resulted in a discrepancy around 7-8.5% towards lower values. However, the fits are retained because they make the error prediction much more efficient.

- The final test removes the requirement that a tag and probe jet be present in the events P is applied to and replaces it with the general requirement that the event have at least two jets total passing $E_{\mathrm{T}} > 40$ GeV, $|\eta| < 2.5$, and $|timing| < 5$ ns, as is the general requirement when P and Q are applied for the full background estimate. This results in a 3% discrepancy for leading jets and a 12% discrepancy for sub-leading jets.

The next cross-check used P to predict the number of CalRatio triggered events in the official dataset. In principle, P should predict the number of events firing the CalRatio trigger and passing all cuts applied to the triggering jet which also contain a second jet satisfying $E_{\mathrm{T}} > 40$ GeV, $|\eta| < 2.5$, and $|\text{timing}| < 5$ ns, i.e. the conditions under which P was calculated. A discrepancy in the two numbers could suggest signal contamination or a problem with the calculation of P. If the predicted background is very large, however, the relative signal contamination should be small.

When P is applied alone to the EF_j15 QCD sample under the same conditions that both P and Q are applied in the full background prediction it is predicted that 512500 ± 93800. In the full CalRatio triggered dataset a total of 501387 triggering events satisfying the required criteria for P exist.

The breakdown for the prediction is:

- 474600 ± 93200 jets will be leading jets.

- 36100 ± 10100 jets will be sub-leading jets.
- 1700 ± 500 jets will be neither.

While the breakdown within the actual dataset is:

- 429273 triggered jets are the leading jet in the event.
- 67568 triggered jets are the sub-leading jet in the event.
- 4546 triggered jets are neither.

The prediction for leading jets is in good agreement with the observation. The prediction for sub-leading jets is over 3σ below the observation while the prediction for lower E_{T} is even worse. In over 85% of cases the triggering jet is the leading jet, so while the the predictive power of P for non-leading triggering jets is poor the overall prediction from P is within 1σ. When this test is repeated using different triggers (EF_j25, EF_j35, and EF_j55) the results are within 4% of the above.

The final cross-check verifies that the SF can be correctly calculated and applied. The scale factor almost doubles the prediction, so it is necessary to establish that it performs its function accurately. As SF was developed using a grid, with its two components (EMF and nTracks) being calculated along two axes and combined multiplicatively it is possible to validate the scale factor in various off-axis bins. Several non-signal, off-axis bins were chosen and their scale factor was calculated using the method previously described. However, for simplicity's sake the scale factors multiplied the raw scale factors from the axes rather than using the fit functions shown in Figure 5.22. Then, the full cut flow was applied to the CalRatio triggered dataset using the cuts indicated by the bin for the non-triggering jet in the event. The number of events predicted by applying this predicted SF to the raw SM multijet background prediction is then compared to the number of events counted in the CalRatio triggered dataset.

A total of 9 off-axis bins were chosen covering a range of predicted scale factor from 0.82 to 1.26. The bins chosen for the cross-check and their predicted scale factors are marked in purple in Figure 5.25. The red and blue bands indicate the axes along with the EMF and nTracks components of SF were calculated for both the main background prediction and this test. The orange bin marks the signal region. Both the predicted and observed number of events are displaced in Figure 5.26. The predicted value is on the right while the observed is on the left of each cross-check bin. Statistical errors are included with predicted and observed values in Table 5.8. The observation is consistently within 1σ of the prediction, ranging from a 0.34σ under-prediction to a 0.03σ over-prediction. This small variation over a range of EMF and nTracks values provides a clear cross-check of the critical final step of the SM multijet background prediction.

nTracks	EMF	N Predicted	Error	Data	Nσ Diff
2	0.15-0.25	926	289	935	0.03
2	0.25-0.35	1746	549	1729	0.03
3	0.15-0.25	1025	315	1069	0.14
3	0.25-0.35	2219	1406	2253	0.02
4	0.35-0.45	4029	1236	4223	0.16
5	0.45-0.55	6286	1894	6417	0.07
7	0.35-0.45	1297	382	1426	0.34
7	0.65-0.75	8430	2394	8995	0.24

Table 5.8: The number of predicted SM multijet background events and the number found in the CalRatio triggered data sample for the various cross-check squares. The nTracks and EMF columns specify the grid square, N predicted is the number of events that are predicted, and Error is the statistical error on the prediction. The next column, Data, is the number of actual events found in with the grid's cuts on the second jet. The final column is the number of σ difference between the predicted and the observed values.

Several possible systematics are associated with the SM multijet background prediction:

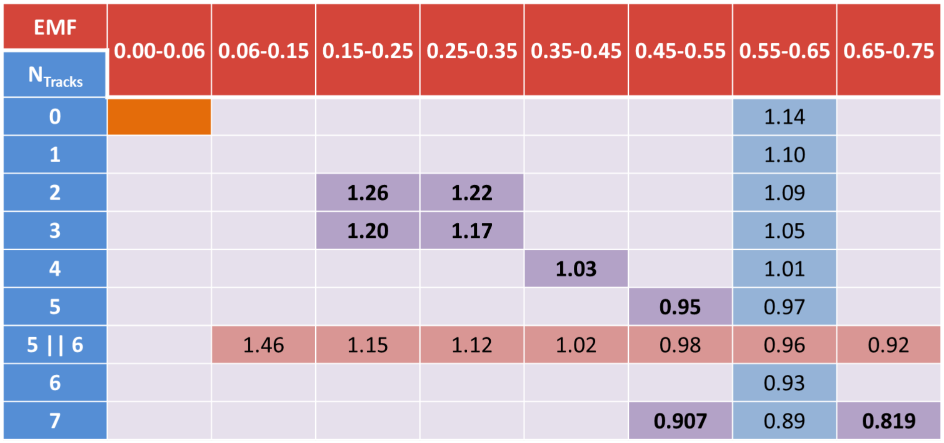

EMF N_{Tracks}	0.00-0.06	0.06-0.15	0.15-0.25	0.25-0.35	0.35-0.45	0.45-0.55	0.55-0.65	0.65-0.75
0	🟧						1.14	
1							1.10	
2			**1.26**	**1.22**			1.09	
3			**1.20**	**1.17**			1.05	
4					**1.03**		1.01	
5						**0.95**	0.97	
5 || 6		1.46	1.15	1.12	1.02	0.98	0.96	0.92
6							0.93	
7						**0.907**	0.89	**0.819**

Figure 5.25: The scale factors for off-axis grid squares. The horizontally arranged, red-shaded squares indicate the values of $N_{\text{data}}/N_{\text{QCD}}$ for the EMF band, when the number of tracks was required to be 5 or 6. The vertically arranged, blue-shaded squares indicate the values $N_{\text{data}}/N_{\text{QCD}}$ for the nTracks band, when the EMF was required to be between 0.55 and 0.65. The bold purple squares are those chosen for the cross-check and their values are equal to the product of the two (red-shaded and blue-shaded) scale factors corresponding to their position on the grid. The orange square indicates the signal region.

- A systematic associated with the assumption that jet E_{T} and η are uncorrelated.
- A systematic concerning the inclusion of the $\Delta\phi > 2.0$ cut in the tag-and-probe method but not the main analysis cut flow.
- A systematic addressing possible cosmic contamination in the background sample.
- A systematic addressing possible signal contamination in the background sample.

These systematics are described below and summarized in Table 5.9.

The E_{T} and η components of both P and Q are calculated separately and are assumed to be uncorrelated when combing them in Equation 5.7. In actuality a small correlation exists between the two jet parameters. To measure the systematic the maximum variation in average jet E_{T} during a scan of η, and vice versa, was measured using the SM multijet sample. This resulted in a 2% variation in both cases. Next the E_{T} and η of each jet was

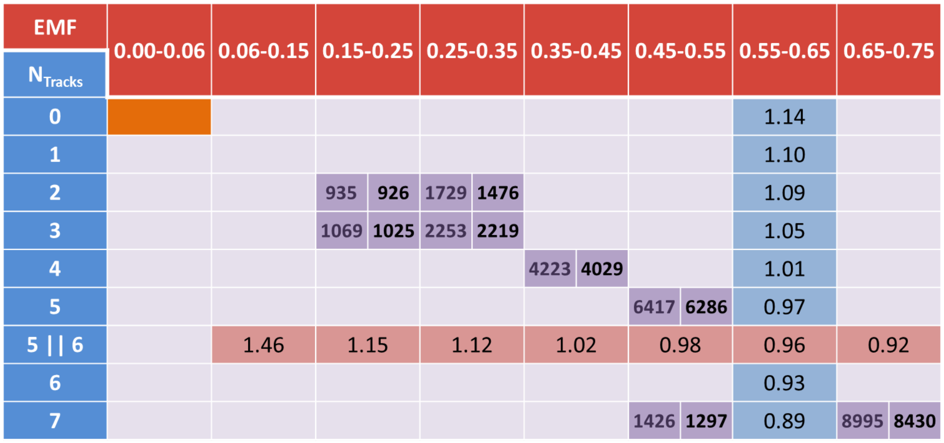

EMF N_{Tracks}	0.00-0.06	0.06-0.15	0.15-0.25	0.25-0.35	0.35-0.45	0.45-0.55	0.55-0.65	0.65-0.75
0							1.14	
1							1.10	
2			935 **926**	1729 **1476**			1.09	
3			1069 **1025**	2253 **2219**			1.05	
4					4223 **4029**		1.01	
5						6417 **6286**	0.97	
5 || 6		1.46	1.15	1.12	1.02	0.98	0.96	0.92
6							0.93	
7						1426 **1297**	0.89	8995 **8430**

Figure 5.26: The observed and predicted number of events for off-axis grid squares. The bold purple squares are those for which a prediction was determined. The left-hand value in each square is the number of events observed in the CalRatio triggered data sample. The right-hand value is the predicted number of events. The prediction is simply the combined scale factor multiplied by the raw SM multijet prediction determined using the methods discussed earlier in this section. The horizontally arranged, red-shaded squares indicate the values of $N_{\text{data}}/N_{\text{QCD}}$ for the EMF band, when the number of tracks was required to be 5 or 6. The vertically arranged, blue-shaded squares indicate the values $N_{\text{data}}/N_{\text{QCD}}$ for the nTracks band, when the EMF was required to be between 0.55 and 0.65.

shifted upwards and downwards by 2% in P and Q. The systematic was taken to be half the difference between the maximum change in the final result before application of SF. This corresponds to a 6% systematic, or 0.79 events.

The $\Delta\phi > 2.0$ cut was included in the tag-and-probe method to select good dijet events, but this cut was not included in the full analysis cut flow. The systematic associated with the inclusion of this cut was calculated by first re-deriving P and Q with the cut removed. The 4% difference in the predicted background (before application of the SF), 0.53 events, is taken as the systematic.

Cosmic ray events present in the tag-and-probe sample could contaminate P and Q. An upper bound can be placed on the contamination by predicting from the the empty BC dataset the number of cosmic jets that satisfy the P criteria and pass one of the single-jet triggers used to form the tag-and-probe sample. This prediction can be compared to the number of events satisfying this criteria in the CalRatio triggered data sample to estimate the multiplicity of cosmic events as compared to SM multijet events. It is not possible to do this with the Q criteria because the empty BC dataset contains only events selected by the CalRatio trigger. However, most jets in cosmic events that were collected have $E_{\mathrm{T}} >$ 60 GeV (Figure 5.13 and would therefore satisfy both the P and Q criteria). While a portion of events would in general contaminate Q only, its much larger numerator should reduce the relative effect of this contamination. Applying the criteria for calculating P to the empty BC dataset results in less than 10 qualifying events. The high prescales ($\sim$1000) of the single jet triggers in the E_{T} range typical of these events makes it highly unlikely such an event would be randomly included. The cosmic contamination is determined to be negligible.

Signal present in the tag-and-probe dataset would contaminate both P and Q. Signal contamination can be estimated by comparing the number of signal events predicted to satisfy the P criteria in the signal samples to the number which do so in the CalRatio triggered data sample (where "contamination" can be assumed to be highest, by design). About 11000 events satisfy the criteria in the sample with a $\Phi = 140$ GeV mass, the sample with the largest observed in any of the low-mass signal samples. A larger number of events satisfy the criteria in some high-mass samples, but not by more than a factor of 2. By contrast, there over 500,000 such events in the CalRatio triggered data sample. This suggests that less than 1% of jets contributing to P could be signal jets. The signal contamination is taken as negligible and is not included in the table. If present, it would inflate the prediction and thus lower the sensitivity to signal, reducing rather than increasing any limits set.

Origin	Systematic Error
Correlation of E_{T} and η	0.69
$\Delta\phi$ cut	0.46
Cosmic contamination	0.0
Signal contamination	0.0

Table 5.9: Systematic errors (absolute) in the QCD background estimate for the 20.3 fb^{-1} data range

5.3.4 Mixed Backgrounds

The possibility of a cosmic ray muon and a BIB event coincidentally creating signal-like jets was also estimated. This probability is actually larger than that for two independent BIB events due to the higher probability of a cosmic ray event. The background may be estimated using a formula similar to Equation 5.6 by replacing the square of P_{BHJet} with $P_{\mathrm{BHJet}} * P_{\mathrm{CosmicJet}}$. The resulting prediction is 0.24 ± 0.09 events. This value does not incorporate any cut on $E_{\mathrm{T}}^{\mathrm{miss}}$, which should lower such a background prediction substantially.

The possibility of a mixed event containing a signal-like jet from the SM multijet background coincident with one from NCB must also be considered. Events triggered by the non-NCB jet while containing an NCB jet are included implicitly as contamination in the SM multijet background estimation. An upper limit can be set on the opposite case where the triggering jet is an NCB jet while the second jet failed to fire the trigger but passes the offline analysis cuts.

This estimation is performed by approximating a P_{SMJet} analogous to P_{BHJet} but containing no trigger requirement and using the lower 40 GeV cut on E_{T}. This P_{SMJet} is very similar to Q, but is an event probability rather than a single jet probability. If the single jet probability Q is multiplied by the average number of jets in a SM multijet event that satisfy the conditions to be included in the denominator of Q the result is an event probability. This event probability is an upper limit for P_{SMJet}, which is taken as a per-BC quantity, but not every event will contain a jet passing at least the EF_j15 trigger (and thus enter into the calculation of Q. To simplify the calculation only the maximum value of $Q(E_{\mathrm{T}})$, 2.5×10^{-6}, was used. The resulting P_{SMJet} is $P_{\mathrm{SMJet}} = 4.7 \times 10^{-7}$.

The product of P_{SMJet} with P_{BHJet} and P_{CosJet} indicated the predicted background is smaller than 0.04 events. This is a upper estimate which ignores the impact of the $E_{\mathrm{T}}^{\mathrm{miss}}$ cut, track coincidence, and the already mentioned BC versus EF_j15 event probability. As a result, both of these backgrounds are taken to be negligible.

5.4 Systematics

Various systematic uncertainties on both MC-based and data-based calculations must be taken into account when evaluating the results. The systematics associated with the background calculations have already been detailed in the previous section. The remaining systematics are those associated with the production of the MC signal samples, uncertainties address how well the MC simulates the collision and its environment.

5.4.1 Φ Production Cross-Section

The Φ production cross-section is taken as the gluon-gluon production cross-section the Higgs would possess if it had the mass of the Φ. The uncertainty on the production is therefore also taken as the uncertainty on the production cross-section of a Higgs of that mass. These uncertainties are shown in the first column of Table 5.14.

5.4.2 PDF Uncertainty

The uncertainty associated with the use of a particular PDF for modeling the parton's initial state is calculated using a standard procedure developed by the Top group. Each MC signal event is reweighted with three different PDFs and their corresponding error sets: MSTW2008nlo68cl, CT10, and NNPDF2.3. Each error set is created by varying the error-relevant parameters of the PDF. The weight of an event for a new PDF or error set is calculated as in Equation 5.11.

$$w = \frac{PDF(x_1, f_1, Q) \times PDF(x_2, f_2, Q)}{PDF_0(x_1, f_1, Q) \times PDF_0(x_2, f_2, Q)} \tag{5.11}$$

PDF_0 represents the original PDF the sample was generated with, x is the momentum fraction of a parton, f its flavor, and Q is the root of the energy resolution scale.

After reweighting the analysis cut flow is reapplied for both the default PDF and each error set, resulting in a distribution of the number of events passing the cut flow. The RMS width of the distribution is the intra-PDF uncertainty for that PDF. An inter-PDF uncertainty is the separation of the means of the distributions for two different PDFs. The final, full-PDF uncertainty combines the intra- and inter-PDF uncertainties using half the difference between the highest mean plus its width and the lowest mean less its width. This procedure was applied to two signal samples, the $m_\Phi = 140$ GeV, $m_{\pi_\mathrm{v}} = 10$ GeV sample and the $m_\Phi = 126$ GeV, $m_{\pi_\mathrm{v}} = 40$ GeV sample resulting respectively in an uncertainties of 2.1% and 2.0%. The larger of the two values, 2.1%, is applied to all samples.

5.4.3 Pile-up uncertainty

Pile-up has the ability to spoil signal jets by depositing extra energy in the ECal or creating tracks that overlap with a jet. Pile-up is added to signal samples using a overlay method with a minimum bias pile-up sample. This is generally done before the full data taking period has completing. As a result, the pile-up distribution used to generate the signal samples will not accurately represent the pile-up distribution from the full data taking period. To correct for

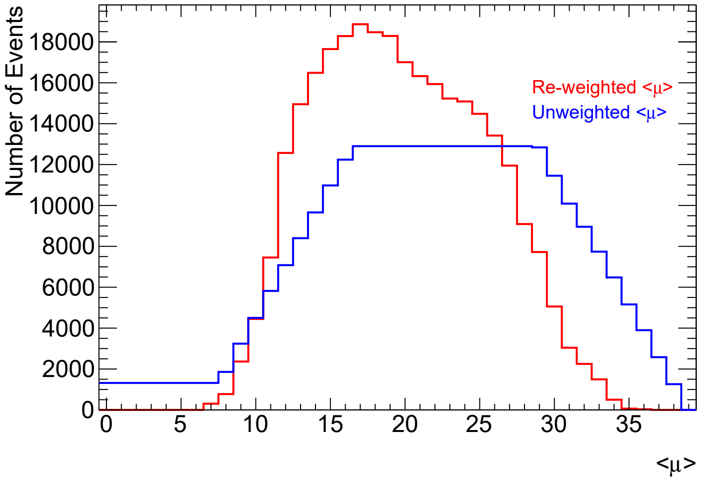

Figure 5.27: Unweighted (blue) and re-weighted (red) distributions of the average number of pile-up interactions $< \mu >$ for the $m_{\mathrm{H}} = 126$ GeV, $m_{\pi_{\mathrm{v}}} = 25$ GeV sample.

this discrepancy events are reweighted to give them the same pile-up distribution as is seen in data [56]. The distribution of the mean number of pile-up interactions $< \mu >$ before and after reweighting is shown in Figure 5.27. This reweighting and well as the overlay introduce an uncertainty to the analysis.

The uncertainty is evaluated through a data-MC comparison with the SM multijet data sample. A tag-and-probe method is used to select events with the following requirements for both MC and data:

- Event: passes EF_b55_NoCut_J55 trigger, passes all standard analysis event DQ cuts, passes $E_{\mathrm{T}}^{\mathrm{miss}}$ cut
- Tag jet: ATLAS Good Medium jet, $p_{\mathrm{T}} > 40$ GeV, $|\eta| < 2.5$
- Probe jet: HV Good Medium jet, $p_{\mathrm{T}} > 40$ GeV, $|\eta| < 2.5$, $\Delta\phi(\mathrm{Tag}, \mathrm{Probe}) > 2.0$

The trigger was chosen so that the dataset might also be used to evaluate the trigger uncertainties. It ensures that the same trigger-level tracking container is available as is used

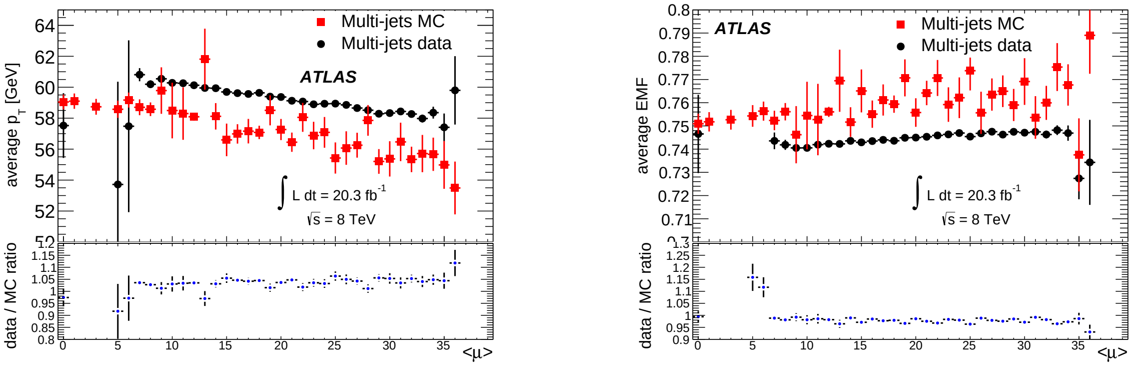

Figure 5.28: The pielup dependence of jet p_{T} (left) and jet EMF (right). A linear fit is made to the ratio of data to MC and its slope used to propagate the variation of the parameter in the MC samples.

by the CalRatio trigger.

The distributions of probe jet p_{T}, η, ϕ, EMF, timing, and number of associated tracks are plotted as a function of $< \mu >$. Figure 5.28 shows example distributions for the jet p_{T} and EMF. A linear fit is applied to the data to MC ratio and the slopes are taken as the variation for each parameter to be propagated through in the MC samples. The corresponding variations on the jet parameters are:

- p_{T}: $5.8 * 10^{-4}$
- η: $1.8 * 10^{-4}$ GeV
- ϕ: $4.1 * 10^{-4}$
- EMF: $2.7 * 10^{-4}$
- timing: $2.2 * 10^{-3}$ ns

The corresponding systematics for this procedure are displayed in Table 5.10 for the low mass signal samples. However, it was requested by an analysis review board that a flat systematic of 10% be used. Many analyses determine that a similarly large systematic is appropriate and the analysis is one that, due to the nature of its signal jets, would be strongly affected by the effects of pile-up. The larger 10% uncertainty also has little effect on the limits set by the analysis because the uncertainties are dominated by those from the SM multijet background. Due to the study performed, it can be assumed that 10% is a conservative value for the systematics.

MC sample	systematic (%)
m_Φ = 100 GeV, m_{π_v} = 10 GeV	+0.2; -0.7
m_Φ = 100 GeV, m_{π_v} = 25 GeV	+0.0; -0.3
m_H = 126 GeV, m_{π_v} = 10 GeV	-0.1; -0.2
m_H = 126 GeV, m_{π_v} = 25 GeV	+1.8; -0.2
m_H = 126 GeV, m_{π_v} = 40 GeV	+1.5; -1.0
m_Φ = 140 GeV, m_{π_v} = 10 GeV	+0.6; -0.1
m_Φ = 140 GeV, m_{π_v} = 20 GeV	+0.9; +0.1
m_Φ = 140 GeV, m_{π_v} = 40 GeV	+0.8; -0.4

Table 5.10: Variation in Monte Carlo signal samples due to pile-up effects.

5.4.4 E_T^{miss} Cut

The analysis includes a 50 GeV cut on E_T^{miss} in order to remove NCB events. A systematic is therefore necessarily determined to account for any mismodeling of the E_T^{miss} in the MC samples. Previous studies have shown that the error on the E_T^{miss} near 50 GeV is about 10%. The E_T^{miss} of each event is smeared by 10% and the analysis cut flow is reapplied. This results in a variation of less than 6% for low mass samples and less than 13% for high mass samples, where the E_T^{miss} cut removes a larger fraction of events. The results are summarized in Table 5.14 and Table 5.15.

5.4.5 Timing Cut

The analysis requires that jets satisfy $-1 < t < 5$ ns. As with the $E_{\mathrm{T}}^{\mathrm{miss}}$ cut this provides a powerful tool for discriminating against NCB, but does require an assessment of any uncertainty associated with the inclusion of the cut. The peak positions of the SM multijet events and MC events are within 0.5 ns of one another. To evaluate the systematic the timing of jets was smeared by this amount and the variation in the expected number of signal events was taken as the systematic. The results, less than 10% for each signal sample, are displayed in Table 5.14 and Table 5.15.

5.4.6 ISR and FSR

Signal jets are "vulnerable" to ISR. ISR may leave energy deposits which lower the $\log_{10}(E_{\mathrm{H}}/E_{\mathrm{EM}})$ of a signal jet, or produce a track that lies coincident with a jet. It may also affect the E_{T} of the Φ, and thus the E_{T} of the jets it produces upon decay. The analysis evaluates the ISR systematic using a toy MC to simulate an increase or decrease in the presence of ISR in the samples. FSR will occur within the HCal for signal jets and so is not evaluated. It may affect the overall shape of a jet but was verified to not affect the overall acceptance of the jet when the analysis cuts are applied.

To increase or decrease ISR two libraries of jets are assembled from the $m_{\Phi} = 126$ GeV, $m_{\pi_{\mathrm{v}}} = 10$ GeV MC sample: one of jets with a $p_{\mathrm{T}} > 2$ GeV ISR gluon within $\Delta R < 0.1$ of a signal jet (ISR contaminated jets) and one of all other signal jets. The overall ISR contamination is halved or doubled by selecting pairs jets at random from the libraries. The analysis cuts are then applied to the resulting event with the exclusion of the $E_{\mathrm{T}}^{\mathrm{miss}}$ cut. A change in acceptance of -0.6% (+1.6%) is observed when the number of ISR contaminated jets is doubled (halved).

An additional uncertainty is calculated related to the boost given to the jets by the Φ. The ISR gluon E_{T} peaks at around 5% of the Φ E_{T} mass. To evaluate a systematic the E_{T} of ISR contaminated jet in signal events is varied by this amount and the resulting change in the acceptance is measured. The resulting uncertainty is -0.6% and +1.3%.

5.4.7 Jet Energy Scale Uncertainty

The Jet Energy Scale is usually determined via the use of the JESUncertaintyProvider tool. This uncertainty is naive with respect to the EMF of jets and determines the uncertainty based on the p_{T} and η of each jet and the number of primary vertices in each event [11]. While this is sufficient for most analyses, for this analysis it was prudent to determine what dependence the uncertainty has on the jet EMF. The procedure used to develop the JESUncertaintyProvider tool was adapted to include an EMF dependence. This allows for the calculation of an additional uncertainty resulting from the application of the standard JES calibration to jets resulting from the decay of LLPs.

The procedure studies the jet calorimeter response by balancing jet momenta in dijet events. The balance in data and MC are compared in various η and EMF regions. The variation is propagated to the signal MC to determine its affect on the acceptance of the jets.

Events from the data and MC multijets samples are selected using the EF_55, EF_80, EF_110, and EF_145 triggers. Events are required to satisfy:

- Leading jet: HV Good Medium, $p_{\mathrm{T}} > 40$ GeV, $|\eta| < 2.5$
- Sub-leading jet: HV Good Medium, $p_{\mathrm{T}} > 40$ GeV, $|\eta| < 2.5$, $\Delta\phi$(Leading, Subleading) > 2.5
- Third jet: $p_{\mathrm{T}} < 0.25 * p_{\mathrm{T}}^{\mathrm{average}}$ (average p_{T} of the Leading and Sub-leading jets).

The cuts on the highest p_{T} jet that is neither the leading nor sub-leading jet helps to select clean dijet events.

One jet in each pair is taken as the *reference* jet. This reference jet is required to be in a well studied region of phase space while the other jet, the probe jet, may be in any $EMF-\eta$

region. For an event to enter the study the reference jet must satisfy $0.7 < \mathrm{EMF} < 0.9$. No additional cut is placed on η - the full η range included is well studied. The response of the probe jet to the reference jet depends on their *asymmetry* A, is defined in Equation 5.12. It is measured with respect to $p_{\mathrm{T}}^{\mathrm{average}}$, the average p_{T} of the reference and probe jets. The response is then calculated for each probe jet as in Equation 5.13

$$\begin{aligned} A &= \frac{p_{\mathrm{T}}^{\mathrm{Probe}} - p_{\mathrm{T}}^{\mathrm{Ref}}}{p_{\mathrm{T}}^{\mathrm{average}}} \\ p_{\mathrm{T}}^{\mathrm{average}} &= (p_{\mathrm{T}}^{\mathrm{Probe}} + p_{\mathrm{T}}^{\mathrm{Ref}})/2 \end{aligned} \tag{5.12}$$

$$R = \frac{2+A}{2-A} = \frac{p_{\mathrm{T}}^{\mathrm{Probe}}}{p_{\mathrm{T}}^{\mathrm{Ref}}} \tag{5.13}$$

These measurements are made in four different η regions:

- $\eta_{\mathrm{det}} < 0.8$;
- $0.8 < \eta_{\mathrm{det}} < 1.35$;
- $1.35 < \eta_{\mathrm{det}} < 1.70$;
- $1.70 < \eta_{\mathrm{det}} < 2.50$;

This is done to account for changes in calorimeter geometry and composition in different regions of the detector (Figure 5.29).

The overall asymmetry for each EMF bin is taken as the mean of a gaussian fit to all events with a probe jet falling within that bin. The ratio of data to MC is taken in each bin for each η region. The results are displayed in Figure 5.30.

The ratios are fit with a linear fit to allow extrapolation into the signal region, $0 < EMF < 0.05$, where statistics are low. The fit is performed only for the range $0.05 < EMF < 0.7$, which excludes the reference bins but also higher EMF bins, where the behavior

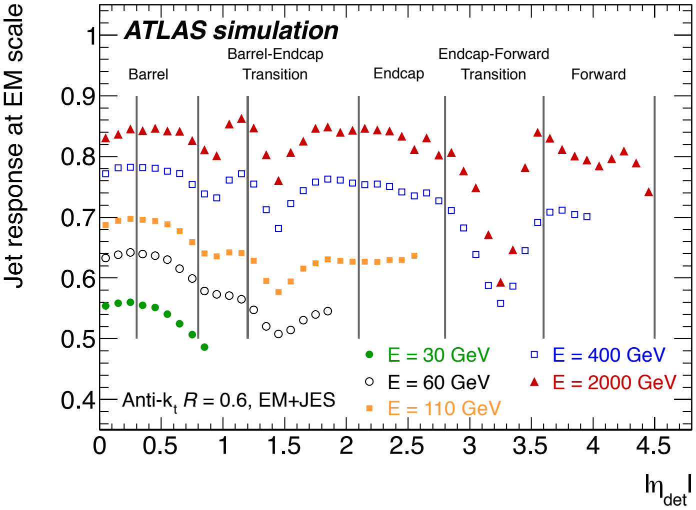

Figure 5.29: Ratio of the average jet energy at the EM scale with to the truth jet energy (the jet response) in Monte Carlo simulation as a function of the jet η [11]. The inverse of the response shown in each bin is equal to the average jet energy scale correction. This result is based on PYTHIA inclusive jet sample.

Detector Eta Region	Assigned Systematics @ EMF =0.0125 (%)
$\eta_{\text{det}} < 0.8$	3.1
$0.8 < \eta_{\text{det}} < 1.35$	1.9
$1.35 < \eta_{\text{det}} < 1.70$	8.3
$1.70 < \eta_{\text{det}} < 2.50$	3.9

Table 5.11: Values of the assigned systematics to the very low EMF bin (EMF=0.0125) for each detector eta region.

may differ from low EMF bins. Figure 5.31 shows the final systematics in each η region. The assigned systematic for a low EMF jet is summarized in Table 5.11.

These values represent a variation on the jet transverse momentum. They are used to smear jet p_{T} in the MC samples to evaluate the impact on the acceptance. The standard JES systematic due to jet p_{T} and an additional systematic for b-jets (when the π_{v} decays

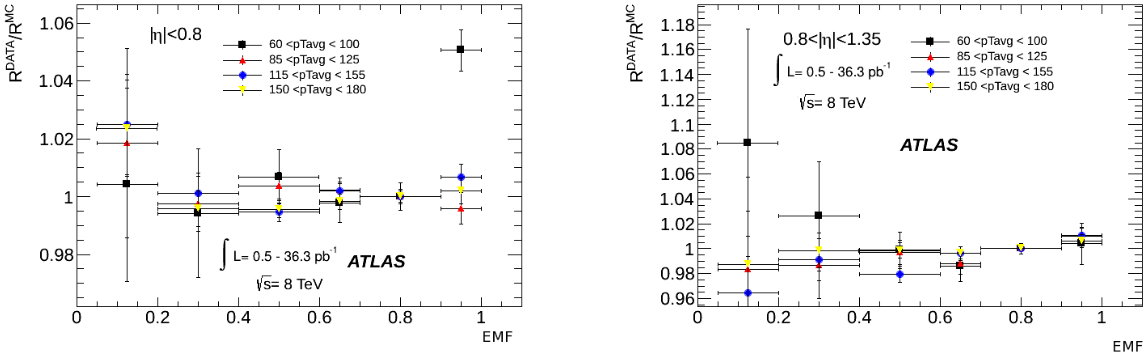

(a) $\frac{R^{\rm DATA}}{R^{\rm MC}}$ for $\eta < 0.8$

(b) $\frac{R^{\rm DATA}}{R^{\rm MC}}$ for $0.8 < \eta < 1.35$

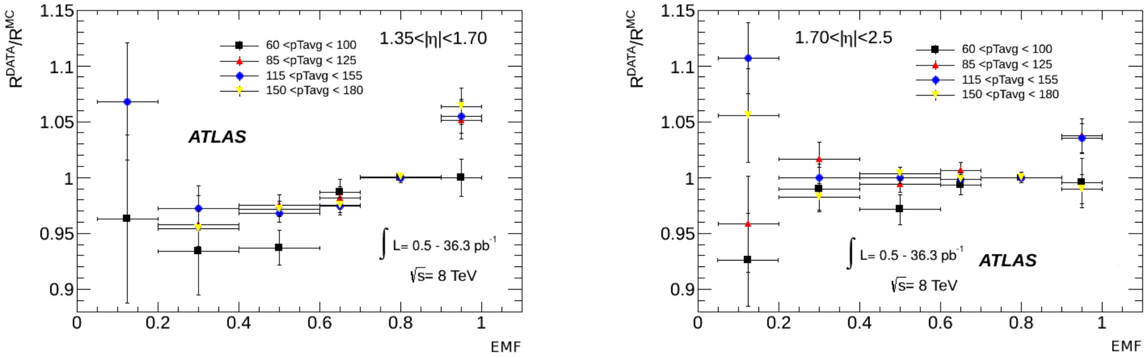

(c) $\frac{R^{\rm DATA}}{R^{\rm MC}}$ for $1.35 < \eta < 1.70$

(d) $\frac{R^{\rm DATA}}{R^{\rm MC}}$ for $1.70 < \eta < 2.50$

Figure 5.30: Ratio data over MC of the response for each EMF bin in the four η regions.

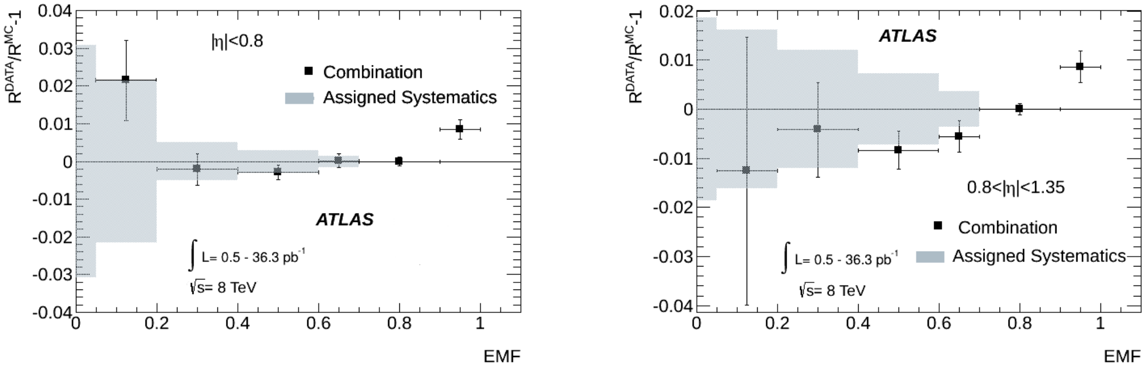

(a) $\frac{R^{\mathrm{DATA}}}{R^{\mathrm{MC}}}$ for $\eta < 0.8$

(b) $\frac{R^{\mathrm{DATA}}}{R^{\mathrm{MC}}}$ for $0.8 < \eta < 1.35$

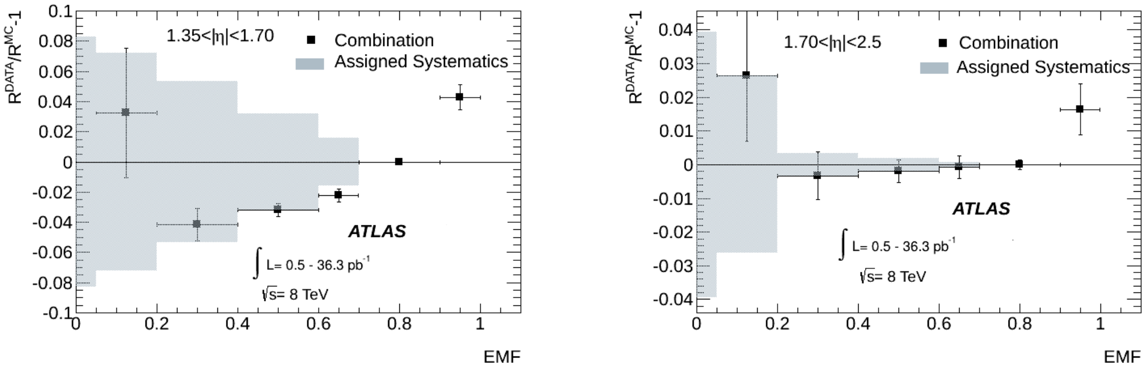

(c) $\frac{R^{\mathrm{DATA}}}{R^{\mathrm{MC}}}$ for $1.35 < \eta < 1.70$

(d) $\frac{R^{\mathrm{DATA}}}{R^{\mathrm{MC}}}$ for $1.70 < \eta < 2.50$

Figure 5.31: Assigned Systematics to the response ratio data over MC (i.e. R $= \frac{p_{\mathrm{T}}^{\mathrm{PROBE}}}{p_{\mathrm{T}}^{\mathrm{REF}}}$) for each eta region.

to bottom quarks) are also evaluated. The results are shown in Table 5.12 for the low mass samples. The combined results for all samples are shown in Table 5.14 and Table 5.15.

5.4.8 Trigger

The accurate modeling of the trigger's performance is crucial. An over- or underestimate for trigger performance will result in an inaccurate prediction for not only the expected number of signal events. Its uncertainty must be taken into accounts when setting limits or declaring a discovery. This is done in this analysis by using a tag-and-probe method to compare the

MC sample	Acceptance variation (%) due to low EMF	Acceptance variation (%) due to b-jet	Total (%)
m_{Φ} = 100 GeV, $m_{\pi_{\rm v}}$ = 10 GeV	+2.1; -3.9	+0.9; -0.8	+2.3; -4.0
m_{Φ} = 100 GeV, $m_{\pi_{\rm v}}$ = 25 GeV	+5.0; -3.7	+2.2; -0.0	+5.5; -3.7
$m_{\rm H}$ = 126 GeV, $m_{\pi_{\rm v}}$ = 10 GeV	+2.0; -2.7	+0.8; -0.4	+2.2; -2.7
$m_{\rm H}$ = 126 GeV, $m_{\pi_{\rm v}}$ = 25 GeV	+1.5; -1.6	+0.2; -0.0	+1.5; -1.6
$m_{\rm H}$ = 126 GeV, $m_{\pi_{\rm v}}$ = 40 GeV	+2.6; -6.0	+0.0; -0.8	+2.6; -6.2
m_{Φ} = 140 GeV, $m_{\pi_{\rm v}}$ = 10 GeV	+0.6; -1.1	+0.0; -0.3	+0.6; -1.1
m_{Φ} = 140 GeV, $m_{\pi_{\rm v}}$ = 20 GeV	+1.0; -1.5	+0.7; -0.6	+1.2; -1.6
m_{Φ} = 140 GeV, $m_{\pi_{\rm v}}$ = 40 GeV	+1.3; -1.6	+0.0; -0.0	+1.3; -1.6

Table 5.12: Variation in Monte Carlo signal acceptance due to JES systematics.

efficiency of each cut in MC and data samples.

The trigger performance is evaluated using the same events selected for the evaluation of the pile-up systematics. Each of the primary cuts on $E_{\rm T}$, $\log_{10}(E_{\rm H}/E_{\rm EM})$, and track isolation, is studied independently. This requires use of the same Level-2 objects that the CalRatio trigger evaluates when running on actual events. For this reason the $EF\_b55\_NoCut\_J55$ trigger is used to select events. Most jet triggers do not perform tracking, but b-jet triggers do with the same tracking algorithm as is used by the CalRatio trigger.

The efficiency is evaluated by creating a turn-on curve for each variable. The probe jet is required to have an associated L2 jet. For any given variable, the fraction of offline probe jets with an L2 jet passing the trigger cut is plotted. This gives the trigger efficiency ϵ per bin. Equation 5.14 gives the equation corresponding to the $E_{\rm T}$ cut. The turnon curves for the $E_{\rm T}$ and $\log_{10}(E_{\rm H}/E_{\rm EM})$ cuts are shown in Figure 5.32. Figure 5.33 shows the curve for track isolation. In the case of the track isolation the curve was created with respect to the highest $p_{\rm T}$ L2 track with $\Delta R < 0.2$ of the jet axis. The efficiency in this case shows the

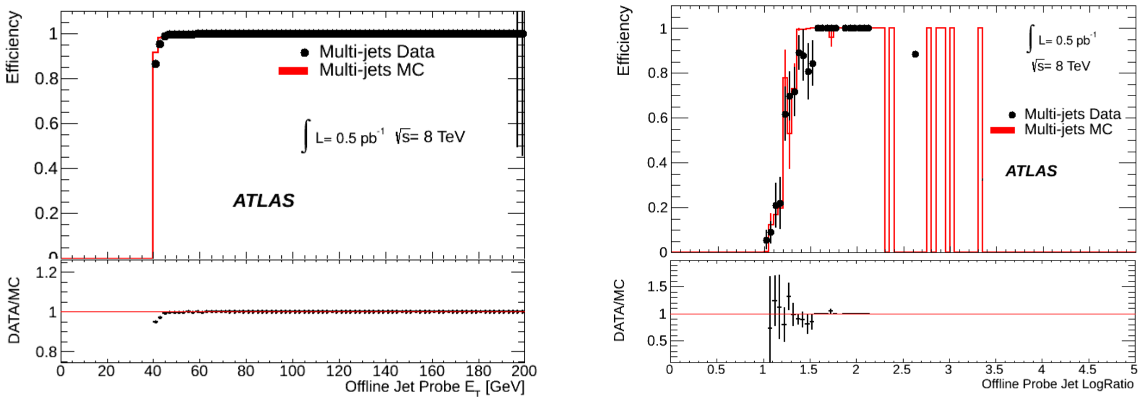

Figure 5.32: Turnon curves for the E_{T} cut (left) and $\log_{10}(E_{\mathrm{H}}/E_{\mathrm{EM}})$ cut (right). The x-axis indicates the offline bin of the probe jet. The trigger cut was applied to the L2 jet matched to the offline jet.

fraction of probe jets that would pass a track isolation cut set at that p_{T}.

$$\epsilon_{\mathrm{E_T}} = \frac{Probe|_{\mathrm{L2}\ E_{\mathrm{T}}>35\ \mathrm{GeV}}}{Probe|_{\mathrm{has\ L2\ jet}}} \tag{5.14}$$

The offline E_{T} cut applied to the triggering jet is at 60 GeV. Figure 5.32 indicates that at this value the trigger is already fully “on”, with respect to E_{T}. For this reason the systematic associated with the E_{T} cut is 0. For the $\log_{10}(E_{\mathrm{H}}/E_{\mathrm{EM}})$ cut a difference of about 11% exists between the data and MC for a $\log_{10}(E_{\mathrm{H}}/E_{\mathrm{EM}}) > 1.2$ offline cut. For the track cut, this difference is about 1%.

The systematic is found by smearing individually the L2 jet parameters and simulating the trigger before reapplying the analysis cut flow and observing the effect on the final acceptance. The track p_{T} is smeared by 10%. This is the amount that the MC value would have to be shifted, according to Figure 5.33, to correct for the 1% discrepancy between MC and data. The amount the L2 $\log_{10}(E_{\mathrm{H}}/E_{\mathrm{EM}})$ must be shifted by is determined by first applying a linear fit to the region near the working point for the MC curve. From this fit it is determined that a shift of 1.7% is needed for the MC and data efficiencies to agree. The variations due to each individual cuts are added in quadrature to determine the total

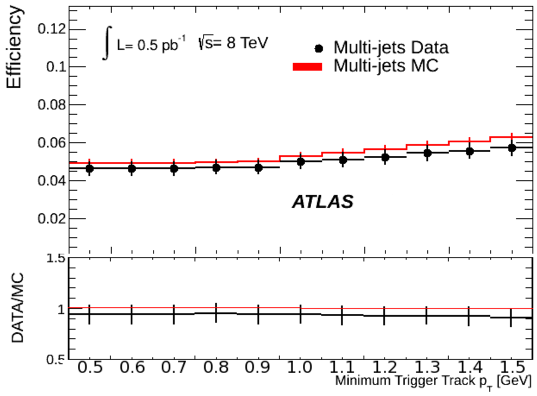

Figure 5.33: Turnon curve for the track isolation cut. The $p_{\rm T}$ cut on the x-axis is online Level-2 value.

systematic. These are summarized in Table 5.13 for the low mass samples. Both the high and the low mass totals are included in the summary tables.

MC sample	Acceptance variation (%) due to $\log_{10}(E_{\rm H}/E_{\rm EM})$ ± 1.7%	Acceptance variation (%) due to ID track $p_{\rm T}$± 10%	Total (%)
m_Φ = 100 GeV, $m_{\pi_{\rm v}}$ = 10 GeV	-0.1; +0.0	+0.0; -0.0	0.1
m_Φ = 100 GeV, $m_{\pi_{\rm v}}$ = 25 GeV	-0.8; +0.0	+0.0; -0.9	1.2
$m_{\rm H}$ = 126 GeV, $m_{\pi_{\rm v}}$ = 10 GeV	-0.6; +0.0	+0.0; -0.9	1.1
$m_{\rm H}$ = 126 GeV, $m_{\pi_{\rm v}}$ = 25 GeV	-1.3; +0.0	+0.0; -0.3	1.3
$m_{\rm H}$ = 126 GeV, $m_{\pi_{\rm v}}$ = 40 GeV	-0.8; +0.0	+0,0; -0.0	1.1
m_Φ = 140 GeV, $m_{\pi_{\rm v}}$ = 10 GeV	-0.4; +0.0	+0.0; -0.3	0.5
m_Φ = 140 GeV, $m_{\pi_{\rm v}}$ = 20 GeV	-0.6; +0.0	+0.0; -0.8	1.0
m_Φ = 140 GeV, $m_{\pi_{\rm v}}$ = 40 GeV	-1.4; +0.0	+0.0; -0.4	1.5

Table 5.13: Variation in global acceptance for Monte Carlo signal samples when ±1.7% is applied on the Level-2 $\log_{10}(E_{\rm H}/E_{\rm EM})$ cut and ±10% is applied on the Level-2 isolation cut. Last column shows the sum in quadrature of the two largest variations.

MC sample m_{Φ}, $m_{\pi_{\mathrm{v}}}$ [GeV]	Higgs σ (%)	JES (%)	Pile-up (%)	Trigger (%)	ISR (%)	PDF (%)	MET (%)	timing (%)	overall (%)
100, 10	$^{+11.1}_{-10.6}$	$^{+2.3}_{-4.0}$	10	0.1	$^{+2.9}_{-1.2}$	2.1	$^{+4.6}_{-3.4}$	$^{+2.7}_{-9.5}$	$^{+16.7}_{-18.5}$
100, 25	$^{+11.1}_{-10.6}$	$^{+5.5}_{-3.7}$	10	1.2	$^{+2.9}_{-1.2}$	2.1	$^{+3.4}_{-2.5}$	$^{+1.7}_{-0.7}$	$^{+17.0}_{-15.8}$
126, 10	$^{+10.4}_{-10.4}$	$^{+2.2}_{-2.7}$	10	1.1	$^{+2.9}_{-1.2}$	2.1	$^{+5.5}_{-2.4}$	$^{+1.6}_{-6.6}$	$^{+16.4}_{-16.7}$
126, 25	$^{+10.4}_{-10.4}$	$^{+1.5}_{-1.6}$	10	1.3	$^{+2.9}_{-1.2}$	2.1	$^{+3.1}_{-1.8}$	$^{+0.8}_{-3.3}$	$^{+15.6}_{-15.5}$
126, 40	$^{+10.4}_{-10.4}$	$^{+2.6}_{-6.2}$	10	1.1	$^{+2.9}_{-1.2}$	2.1	$^{+7.7}_{-4.6}$	$^{+1.9}_{-5.9}$	$^{+18.2}_{-16.9}$
140, 10	$^{+10.1}_{-10.3}$	$^{+0.6}_{-1.1}$	10	0.5	$^{+2.9}_{-1.2}$	2.1	$^{+4.0}_{-5.6}$	$^{+1.9}_{-6.6}$	$^{+15.6}_{-17.2}$
140, 20	$^{+10.1}_{-10.3}$	$^{+1.2}_{-1.6}$	10	1.0	$^{+2.9}_{-1.2}$	2.1	$^{+4.0}_{-3.9}$	$^{+0.4}_{-5.0}$	$^{+15.5}_{-16.2}$
140, 40	$^{+10.1}_{-10.3}$	$^{+1.3}_{-1.6}$	10	1.5	$^{+2.9}_{-1.2}$	2.1	$^{+6.3}_{-4.6}$	$^{+1.8}_{-2.4}$	$^{+16.5}_{-15.8}$

Table 5.14: Summary of systematic uncertainties for the Higgs production cross-section, jet energy scale, pile-up, trigger, initial state radiation, choice of parton distribution function, missing transverse energy, and timing as a percentage of the signal yield. The last column reports the overall systematic uncertainty (including the luminosity [49]).

MC sample m_{Φ}, $m_{\pi_{\rm v}}$ [GeV]	Production σ (%)	JES (%)	Pile-up (%)	Trigger (%)	ISR (%)	PDF (%)	MET (%)	timing (%)	overall
300, 50	$^{+9.6}_{-10.0}$	$^{+0.1}_{-0.3}$	10	0.3	$^{+2.9}_{-1.2}$	2.1	$^{+9.0}_{-7.4}$	$^{+0.5}_{-3.0}$	$^{+13.9}_{-13.3}$
600, 50	$^{+11.2}_{-10.1}$	$^{+0.0}_{-0.1}$	10	0.2	$^{+2.9}_{-1.2}$	2.1	$^{+11.7}_{-11.3}$	$^{+2.2}_{-4.4}$	$^{+17.0}_{-16.2}$
600, 150	$^{+11.2}_{-10.1}$	$^{+0.2}_{-0.2}$	10	0.3	$^{+2.9}_{-1.2}$	2.1	$^{+11.5}_{-10.2}$	$^{+2.7}_{-5.3}$	$^{+17.5}_{-15.1}$
900, 50	$^{+12.8}_{-11.5}$	$^{+0.0}_{-0.1}$	10	0.1	$^{+2.9}_{-1.2}$	2.1	$^{+12.6}_{-9.7}$	$^{+1.0}_{-3.7}$	$^{+18.5}_{-15.9}$
900, 150	$^{+12.8}_{-11.5}$	$^{+0.2}_{-0.3}$	10	0.2	$^{+2.9}_{-1.2}$	2.1	$^{+11.8}_{-10.9}$	$^{+0.9}_{-2.5}$	$^{+18.1}_{-16.3}$

Table 5.15: Summary of systematic uncertainties for the production cross-section, jet energy scale, pile-up, trigger, initial state radiation, choice of parton distribution function, missing transverse energy, and timing as a percentage of the signal yield. The last column reports the overall systematic uncertainty (including the luminosity [49]).

Chapter 6

RESULTS AND LIMITS

The ideal for any search is to declare a discovery. When this is not possible, and it generally is not, limits are set on parameters relevant to the model or process being sought. Whichever is the case, the results from data need to be carefully combined with the predicted yields, backgrounds, and systematics.

For this analysis, an upper limit is set on $\sigma \times \mathrm{BR}$ for the $\Phi \rightarrow \pi_{\mathrm{v}}\pi_{\mathrm{v}}$ process as a function of LLP lifetime. This will be described in more detail in Section 6.2. First, the results of applying the analysis cut flow to the CalRatio triggered events is discussed in Section 6.1. The other necessary pieces for setting the limits, the background analysis and systematics, have already been discussed in Section 5.3 and Section 5.4, respectively.

6.1 Triggered Events

The primary dataset is gathered with the CalRatio analysis trigger, which is designed to identify jets consistent with LLP decays in the HCal. Over 1.5 millions events fired the CalRatio trigger during the full 2012 data taking period. Figure 6.1 shows the $\eta - \phi$ distribution of the triggering jets on the left, and the non-triggering jets in the same events on the right. The structure reflects the ATLAS calorimeter geometry, with the η cut in the trigger responsible for the narrower η range of triggering jets. Blue bands in ϕ are the result of known detector defects. Figure 6.2 shows the $E_{\mathrm{T}}^{\mathrm{miss}}$ and timing distributions of the same events. The label "ATLAS GOOD" in these plots refers to data satisfying all event level DQ criteria. The narrow timing peak and low average $E_{\mathrm{T}}^{\mathrm{miss}}$ value suggest that only a minority of events are from NCB. For all these plots all event level cuts described in Section 5.1, except for the $E_{\mathrm{T}}^{\mathrm{miss}}$ cut, have been applied.

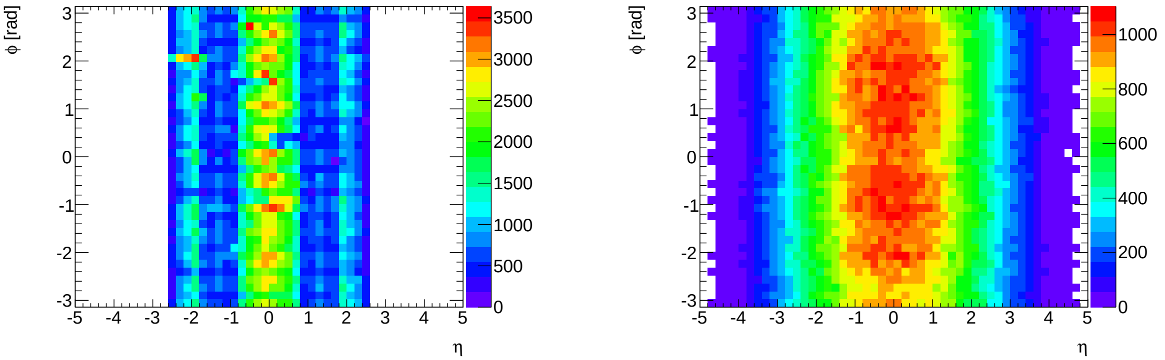

Figure 6.1: Distribution of ϕ vs η of, on the left, triggering jets and, on the right, non-triggering jets in events with one triggering jet. A jet is identified as a triggering jet if $\Delta R < 0.2$ between the jet and the CalRatio trigger object. All jets have an $E_{\mathrm{T}} > 40$ GeV cut applied.

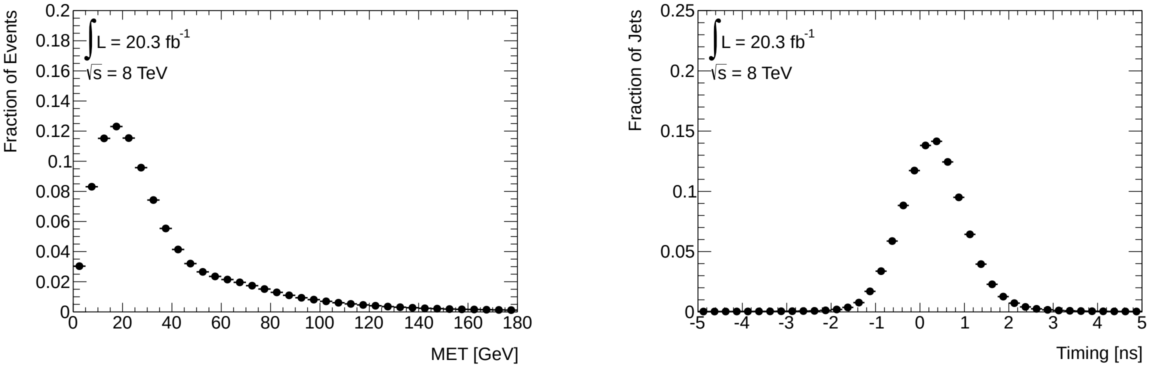

Figure 6.2: Distribution of $E_{\mathrm{T}}^{\mathrm{miss}}$(left) and jet timing (right). The timing distribution includes all jets, triggering and non-triggering, with $E_{\mathrm{T}} > 40$ GeV and $-2.5 < \eta < 2.5$.

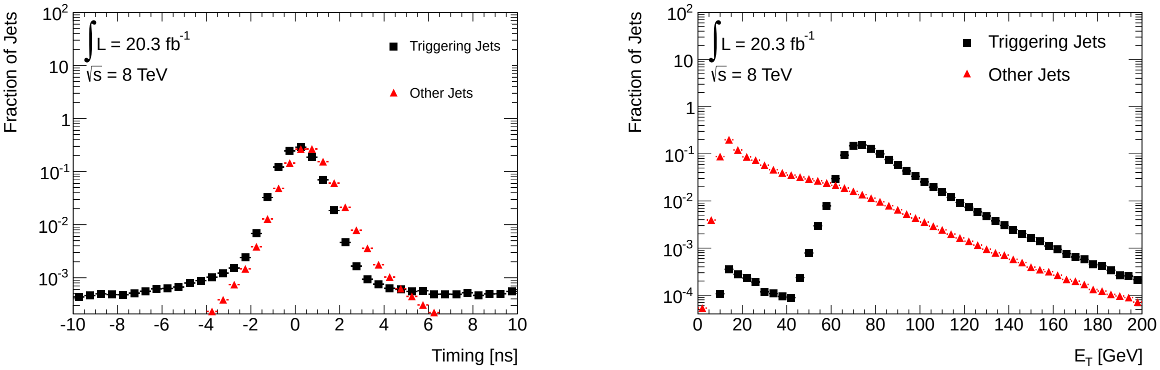

Figure 6.3: Distribution of the jet timing (left) and the E_{T} (right) of triggering (black) and non-triggering (red) jets. The analysis uses a (-1,5) ns time window and requires $E_{\mathrm{T}} > 60$ GeV for the triggering jet (or the leading jet in the case of two triggering jets) and $E_{\mathrm{T}} > 40$ GeV for the second jet.

The timing distribution of jets after the $E_{\mathrm{T}}^{\mathrm{miss}}$ cut is shown on the left of Figure 6.3. The distribution for triggering jets is displayed in black squares while that for other jets in the event are displayed in red triangles. The tails for triggering jets are the result of NCB contamination, particularly cosmic ray events given the presence of both high and low tails.

The right-hand side of Figure 6.3 displays the E_{T} distribution for the same jets, with the lower cut on E_{T} removed to show the behavior at low transverse energies. Low energy triggering jets can result when the HLT energy is significantly different from the offline energy, perhaps due to the various corrections applied to offline jets that are absent for online jets. The triggering jet curves turns on around 60 GeV rather than at the HLT cut level because the JES shifts the overall energy of most jets to higher values.

The $\log_{10}(E_{\mathrm{H}}/E_{\mathrm{EM}})$ and number of tracks associated with triggering and non-triggering jets are displaced respectively on the left and right-hand side of Figure 6.4. The trigger $\log_{10}(E_{\mathrm{H}}/E_{\mathrm{EM}})$ cut biases the $\log_{10}(E_{\mathrm{H}}/E_{\mathrm{EM}})$ peak to higher values than for non-triggering jets. Few triggering jets will fail the offline $\log_{10}(E_{\mathrm{H}}/E_{\mathrm{EM}})$ cut': most offline jet level corrections preserve the EMF of the jet. The number-of-tracks distribution is likewise biased lower for triggering jets than non-triggering jets. However, offline tracking is much more robust

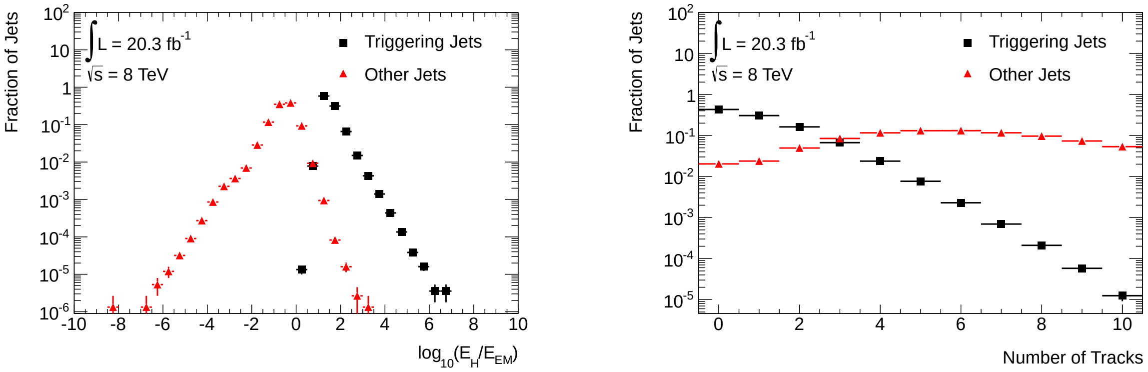

Figure 6.4: Distribution of $\log_{10}(E_{\mathrm{H}}/E_{\mathrm{EM}})$ (left) and the number of tracks with $p_{\mathrm{T}} > 1$ GeV within $\Delta R < 0.2$ (right) of triggering (black) and non-triggering (red) jets. The offline cut flow requires both jets have $\log_{10}(E_{\mathrm{H}}/E_{\mathrm{EM}}) > 1.2$ and that they are trackless.

than online tracking and an associated track is found for over half of the triggering jets.

Finally, Figure 6.5 shows the 1-D η and ϕ distributions for these same jets. While the ϕ distributions are similar for triggering and non-triggering jets the η distribution is shaped by the calorimeter geometry.

The full CalRatio analysis cut flow is applied to the events containing these jets. The number of events surviving each stage of the cut flow is summarized in Table 6.1 for event-level cuts followed by Table 6.2 for the cuts on the jets. Of the over 1.6 million events which both fire the trigger and are present in the GRL, only 24 survive the full cut flow. The $E_{\mathrm{T}}^{\mathrm{miss}}$ cut removes over 300k events, expected to be mostly NCB, while the $\log_{10}(E_{\mathrm{H}}/E_{\mathrm{EM}})$ and track isolation cuts on the second jet have the greatest relative reduction in the number of surviving events. This is not surprising given the distributions in Figure 6.4.

Before the application of the $E_{\mathrm{T}}^{\mathrm{miss}}$ cut, 152 events have two triggering jets while the rest have one. Despite the substantial difference between the number of events with two triggering jets versus the number with a single triggering jet, two of the final 24 events have two triggering jets. This is a result of the much higher rate for triggering jets to pass the offline cuts, a reflection of the trigger's ability to select signal-like jets.

The $\eta - \phi$ distribution of the 24 surviving events is shown in Figure 6.6. The bin color

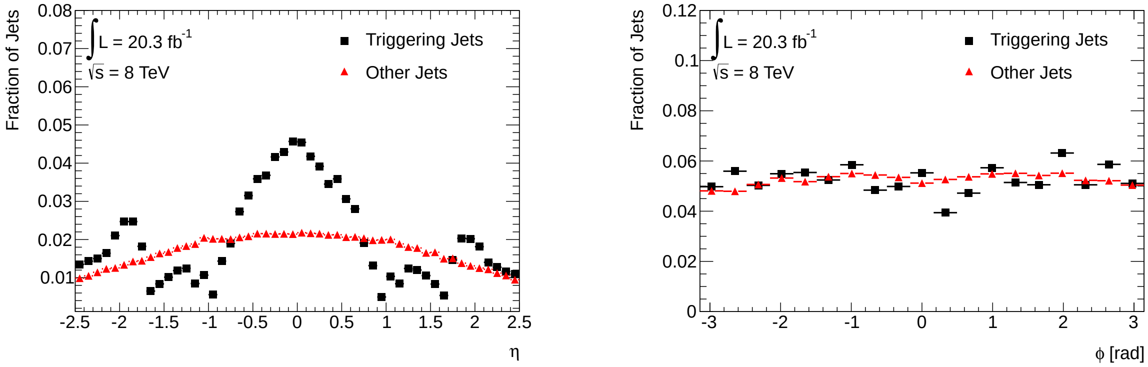

Figure 6.5: Distribution of η (left) and ϕ (right) of triggering (black) and non-triggering (red) jets. The offline analysis cuts require $-2.5 < \eta < 2.5$ while no phi-dependent cuts are applied.

Cut	Number of Events
CaloRatio Triggered Events	1628647
Good PV	1628020
Has > 0 Si tracks with $\eta < 1.0$	1627943
No Line Of Fire Jets	1493744
No DQ Flags	1491320
MET ($<$ 50 GeV)	1142175

Table 6.1: Selection cut flow on the events for the collision events.

is not indicative of the number of events in the bin - red points correspond to the jets to which the 60 GeV cut flow was applied while green points are those to which the 40 GeV cut flow was applied. There is no clustering in $\eta - \phi$ that might suggest some of the events are the result of a detector defect rather than the collision. The $\Delta\phi$ distribution, shown on the right of the same figure, indicates that these events are generally back-to-back. NCB events tend to have a broader $\Delta\phi$ distribution. The timing and Δt distributions shown in Figure 6.7 provide further evidence that these events are standard collision events rather

Cut	Number of Events
Look for a Trigger Jet (first π_v)	
Trigger object matches offline jet	1124269
$-1ns < t < 5ns$	1059331
Jet $E_\mathrm{T} > 60$ GeV	1045699
$\log_{10}(E_\mathrm{H}/E_\mathrm{EM})$ >1.2	890519
No tracks with $p_\mathrm{T} > 1.0$	828423
Jet $\eta < 2.5$	828344
Second Jet (second π_v)	
$-1ns < t < 5ns$	811662
Jet $E_\mathrm{T} > 40$ GeV	557610
$\log_{10}(E_\mathrm{H}/E_\mathrm{EM})$ >1.2	318
No tracks with $p_\mathrm{T} > 1.0$ GeV	97
$\eta < 2.5$	24

Table 6.2: Selection cut flow on the jets for collision events.

than the result of a cosmic or BIB event.

The number of surviving events, 24, is compatible with the background prediction. Limits are therefore set on $\sigma\times$BR using the procedure described in the next section.

6.2 Limit Setting and Statistics

A 95% CLs confidence limit [57] is set on the $\sigma\times$BR for the production of LLPs in the $\Phi \to \pi_\mathrm{v}\pi_\mathrm{v}$ process. The analysis uses the HistFactory framework to do so and produces exclusion limits as a function of LLP lifetime.

Two types of parameters are of interest when setting limits. *Nuisance parameters* are any which are not under direct investigation but which nonetheless have an impact on the pre-

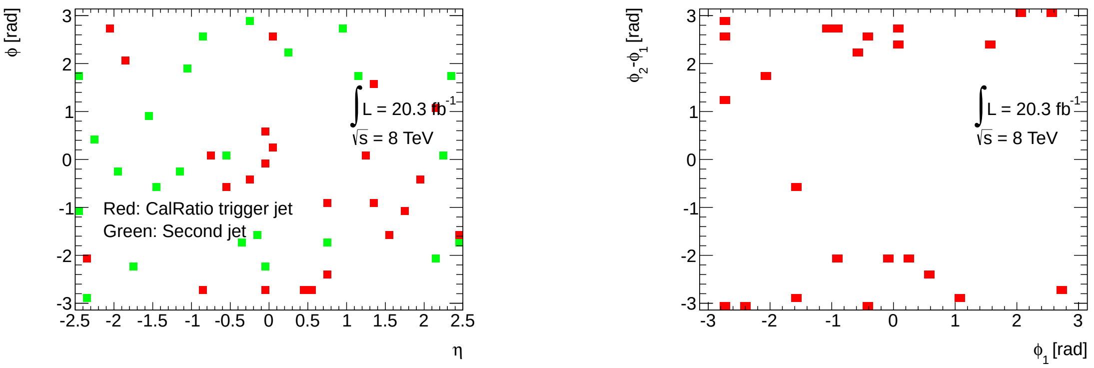

Figure 6.6: (Left) The $\eta - \phi$ distribution of the jet pairs in the 24 surviving events. Red points correspond to jet to which the 60 GeV cut was applied, green to jets to which the 40 GeV cut was applied. Only 2 out of 24 of the jets to which the 40 GeV cut was applied also satisfied the trigger. (Right) The $\phi_1 - \phi_2$ vs. ϕ_1 distribution of the 24 surviving jet pairs, where the subscript 1 indicates the jet to which the 60 GeV cut was applied while the subscript 2 indicates the jet to which the 40 GeV cut was applied.

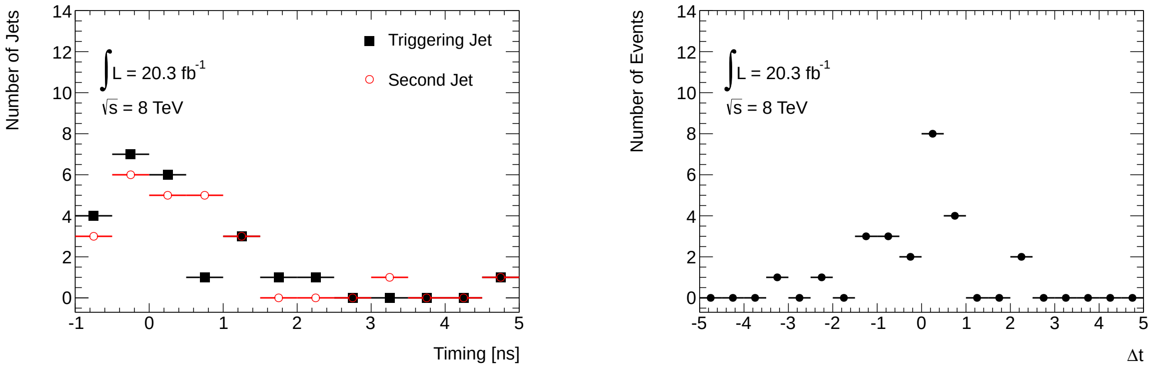

Figure 6.7: (Left) The timing distribution of the jet pairs in the 24 surviving events and (right) the Δt distribution. In the timing histogram black datapoints correspond to the jet to which the 60 GeV cut was applied while red datapoints are those jets to which the 40 GeV cut was applied.

dicted results. The various uncertainties determined in an analysis are nuisance parameters. *Parameters of interest* are those which the analysis or limit setting procedure is constraining. A common parameter of interest is the *signal strength* μ, which if multiplied by the signal cross-section returns the number of events that are compatible with the current data. During limit setting each nuisance parameter is allowed to vary along a $\sigma = 1$ gaussian while determining limits on the parameter of interest.

The CLs method constrains the value of μ, setting exclusion limits when μ is found to be less than one with a sufficient degree of confidence. It does this by determining two frequentest probabilities, a probability determined by measuring the frequency of some observations over a large number of test trials. The first, CL_b, is the probability of finding the observed number of events in data in the background-only hypothesis. The second, CL_{s+b}, is the probability in the signal plus background hypothesis. Ratio of CL_{s+b} to CL_b gives the namesake probability, CL_s. The CLs method is conservative, limiting its usefulness for small signals but preventing the return of aphysical results due to downward background fluctuations. In the case of zero signal $\mathrm{CL}_s = 1$ whatever the background.

The HistFactory framework takes as input the expected number of signal events, the expected backgrounds, the various uncertainties, and the observed numbers of events. The systematics were summarized in Table 5.14 and Table 5.15. The background predictions, expected, and observed yields are summarized in Table 6.3. HistFactory returns the CL_s value. This procedure needs to be reproduced for each signal sample over a range of lifetimes.

The analysis global efficiency depends on the proper lifetime of the LLP, which is unconstrained by the signal model. The longer the LLP proper lifetime, the larger the fraction of particles which will decay beyond the HCal. Conversely, the shorter the proper lifetime, the larger the fraction of particles decaying in the beampipe, ID, or ECal. The effect on the expected number of events as a function of LLP proper lifetime is evident in Figure 6.8. These curves are smoothed at long lifetimes by fitting to a Landau function on the trailing edge. This expected number of events, derived by generating a large number of π_{v} pairs for good statistics and weighting the global efficiency by the momentum distribution present at

Sample (m_Φ, m_{π_v} [GeV])	Expected yields
126, 10	536 ± 23
126, 25	941 ± 44
126, 40	365 ± 31
100, 10	440 ± 29
100, 25	424 ± 37
140, 10	525 ± 20
140, 20	900 ± 37
140, 40	641 ± 30
300, 50	444 ± 11
600, 50	35 ± 1
600, 150	41 ± 2
900, 50	3.5 ± 0.1
900, 150	4.6 ± 0.2
SM Multijets	23.2 ± 8.0
Cosmic rays	0.3 ± 0.2
Total Expected Background	23.5 ± 8.0
Data	24

Table 6.3: Summary of expected number of events, expected background present in the data sample, and the observed number of events in 20.3 fb^{-1}. The error on the signal samples is statistical only, the error on the expected background is statistical and systematic. All results are normalized for a proper decay length of the π_v of 1.5 m. The expected yields assume a SM cross section for $m_H = 126$ GeV of $\sigma_{SM} = 19.0$ pb, and 29.7, 15.4, 3.59, 0.52, and 0.06 pb for $m_\Phi = 100$, 140, 300, 600, and 900 GeV respectively. A 100% branching ratio for $\Phi \rightarrow \pi_v \pi_v$ is assumed.

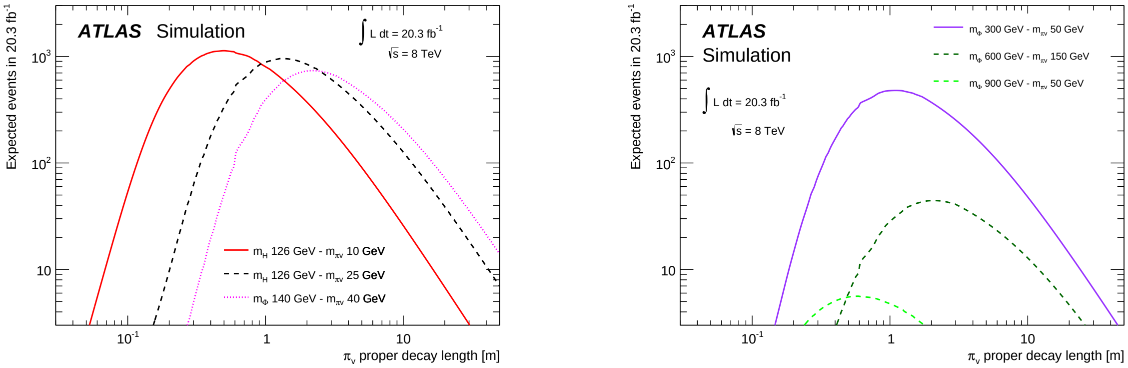

Figure 6.8: The number of events expected to survive the full analysis cut flow for a range of low mass (left) and high mass (right) signal samples. The number of events strongly depends on the proper lifetime of the LLP, which is unconstrained by the signal model.

each lifetime, are fed into HistFactory for each $c\tau$ bin.

The resulting limits for low mass samples are displayed in Figure 6.9, Figure 6.10, and Figure 6.11. For the high mass samples they are displayed in Figure 6.12 and Figure 6.13. The low mass curves include lines at several branching ratios. Expected limits, which are given by the mean result of the many simulations in the CLs method, are shown as the dashed curve. The green and yellow bands show the 1- and 2-σ uncertainties, respectively, on the expected limits. The observed limits are shown by the solid black curve.

The limits tend to be greatest at the low end for higher boosted π_{v} and at the higher end for heavier π_{v}. At low proper lifetimes the signal samples with the fastest π_{v} are expected to have the greatest number of decays in the HCal. The trigger also plays a role - jets must have a minimum energy to fire the trigger. Among the most relevant results are those for the 126 GeV Φ mass point, where the Φ is essentially the Higgs boson. These limits are summarized in Table 6.4. The analysis can exclude π_{v} lifetimes between 14 cm and 8.32 meters, depending on the π_{v} mass.

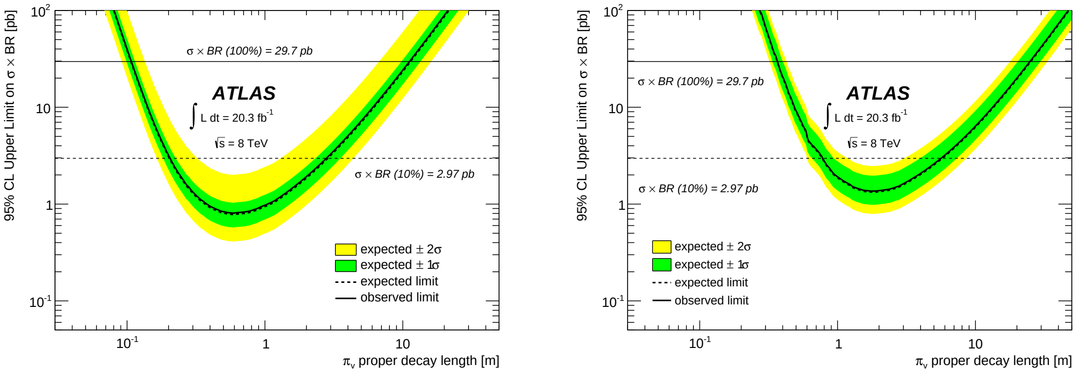

(a) $m_\Phi = 100$ GeV, $m_{\pi_\text{v}} = 10$ GeV.

(b) $m_\Phi = 100$ GeV, $m_{\pi_\text{v}} = 25$ GeV.

Figure 6.9: Observed and expected limits on $\sigma\times$ BR [pb] as a function of the π_v proper decay length for the $m_\Phi = 100$ GeV samples: assuming $\sigma = 29.7$ pb, the horizontal solid line corresponds to a 100% BR and the horizontal dashed line to a 10% BR.

MC sample m_H, m_{π_v} [GeV]	excluded range 30% BR $\Phi \to \pi_\text{v}\pi_\text{v}$ [m]	excluded range 10% BR $\Phi \to \pi_\text{v}\pi_\text{v}$ [m]
126, 10	0.10 – 6.08	0.14 – 3.13
126, 25	0.30 – 14.99	0.41 – 7.57
126, 40	0.68 – 18.50	1.03 – 8.32

Table 6.4: Ranges of π_v proper decay lengths excluded at 95% CL assuming a 30% and a 10% BR for a $m_\text{H} = 126$ GeV.

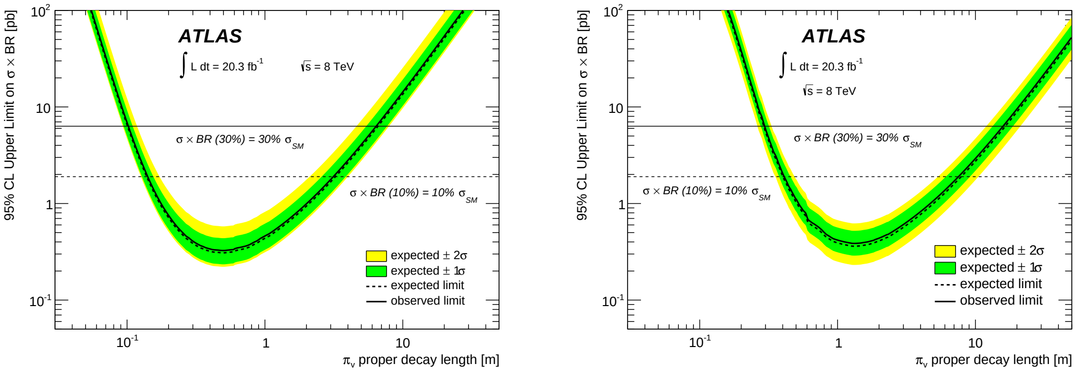

(a) $m_\Phi = 126$ GeV, $m_{\pi_v} = 10$ GeV. (b) $m_\Phi = 126$ GeV, $m_{\pi_v} = 25$ GeV.

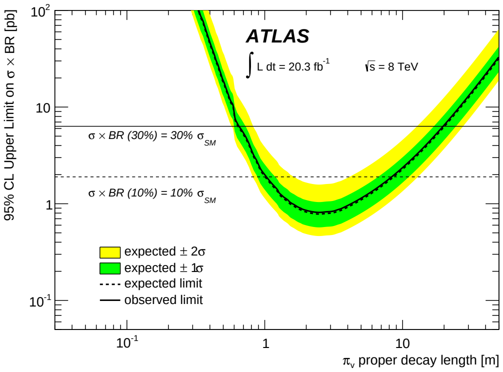

(c) $m_\Phi = 126$ GeV, $m_{\pi_v} = 40$ GeV.

Figure 6.10: Observed and expected limits on $\sigma\times$ BR [pb] as a function of the π_v proper decay length for the $m_\Phi = 126$ GeV samples: assuming $\sigma = 19.0$ pb (SM σ for a 126 GeV Higgs), the solid line corresponds to a 30% BR and the horizontal dashed line corresponds to a 10% BR.

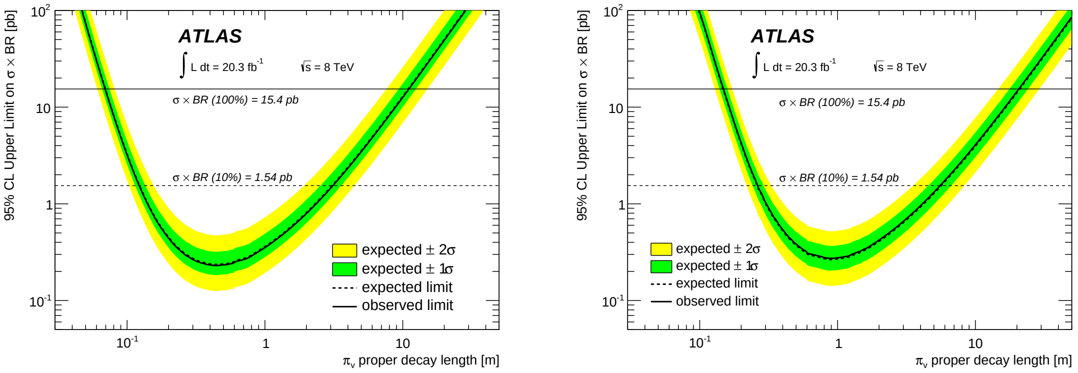

(a) m_Φ = 140 GeV, m_{π_v} = 10 GeV.

(b) m_Φ = 140 GeV, m_{π_v} = 20 GeV.

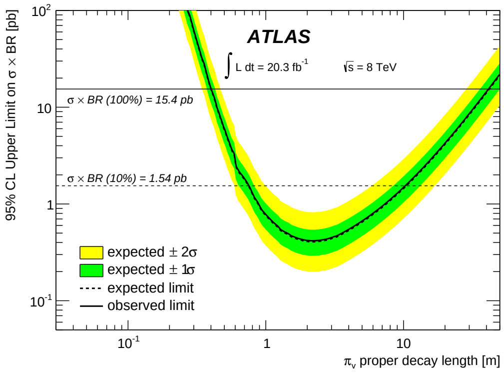

(c) m_Φ = 140 GeV, m_{π_v} = 40 GeV.

Figure 6.11: Observed and expected limits on $\sigma\times$ BR [pb] as a function of the π_v proper decay length for the m_Φ = 140 GeV samples: assuming σ = 15.4 pb, the solid line corresponds to a 100% BR and the horizontal dashed line corresponds to a 10% BR.

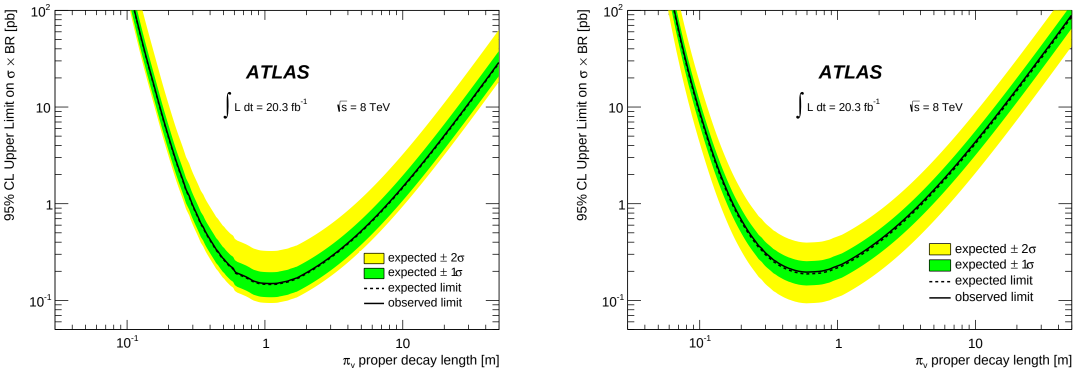

(a) m_Φ = 300 GeV, m_{π_v} = 50 GeV.

(b) m_Φ = 600 GeV, m_{π_v} = 50 GeV.

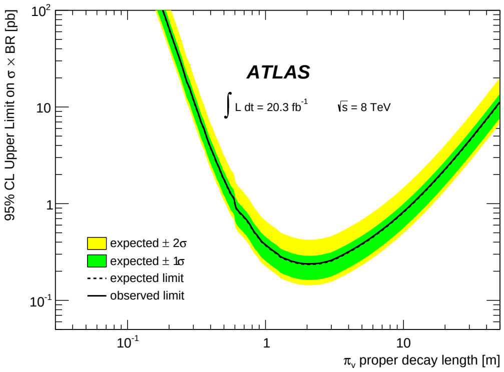

(c) m_Φ = 600 GeV, m_{π_v} = 150 GeV.

Figure 6.12: Observed and expected limits on $\sigma\times$ BR [pb] as a function of the π_v proper decay length for the m_Φ = 300 GeV - m_{π_v} = 50 GeV, m_Φ = 600 GeV - m_{π_v} = 50 GeV, m_Φ = 600 GeV - m_{π_v} = 150 GeV samples.

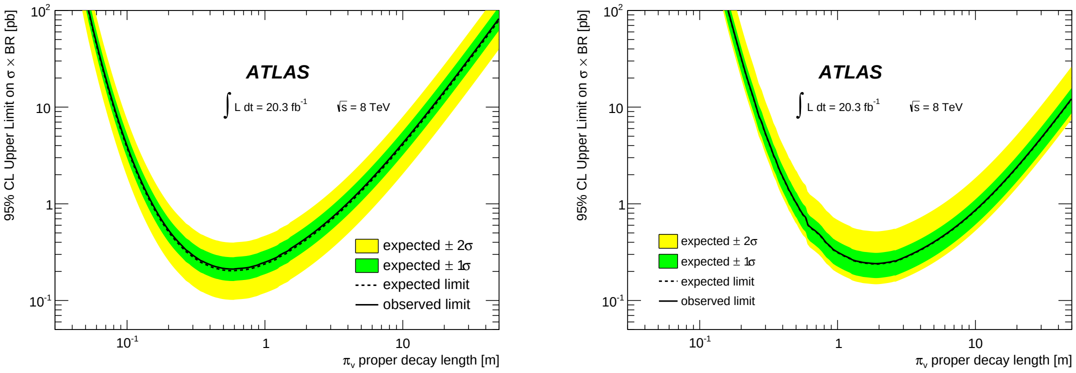

(a) m_Φ = 900 GeV, $m_{\pi_{\mathrm{v}}}$ = 50 GeV.

(b) m_Φ = 900 GeV, $m_{\pi_{\mathrm{v}}}$ = 150 GeV.

Figure 6.13: Observed and expected limits on $\sigma\times$ BR [pb] as a function of the π_{v} proper decay length for the m_Φ = 900 GeV - $m_{\pi_{\mathrm{v}}}$ = 50 GeV and m_Φ = 900 GeV - $m_{\pi_{\mathrm{v}}}$ = 150 GeV samples.

Chapter 7

2015 ANALYSIS UPDATE

In 2015 ATLAS began colliding protons at a center of mass energy of 13 TeV. The CalRatio analysis reproduced its search for the decay of pairs of neutral LLPs in the HCal using the full 2015 dataset, a total of 3.2 fb^{-1} [54]. In general aspects the 2015 and 2012 analyses are very similar. Both are searches for pairs of long-lived neutral particles decaying to jets in the hadronic calorimeter of ATLAS. In several details, however, the analyses are very different. Updates to ATLAS hardware and software are detailed in Section 7.1, as well as changes to the CalRatio trigger and the new signal samples used by the analysis. The major changes to the analysis itself are discussed in subsequent sections.

7.1 Updates to Apparatus, Software, and Signal Samples

7.1.1 Hardware and Trigger Software

The ATLAS hardware remained primarily unchanged between 2012 and 2015. The ID was given an important upgrade, however, in the form of the Insertable B-Layer (IBL). The IBL is a fourth layer for the pixel detector and the innermost layer of the ID. To make space for the IBL the beampipe radius had to be reduced to 2.5 cm from 2.9 cm. It consists of 14 64 cm long staves of pixel models arranged around the beampipe at an average radius of 3.3 cm. Each is at an angle of 14 degrees to the beampipe to allow overlap in ϕ. Pixes have a size of 50 μm in the transverse direction and 250 μm in the longitudinal direction. The IBL improves tracking, especially for b-jets, but does not have a major impact on this analysis.

ATLAS also made several changes to its trigger software. The two software levels of the ATLAS triggering system, Level 2 and Event Filter, have been replaced by a single stage: the High Level Trigger (HLT). Jet reconstruction at the trigger level has also been improved and trigger jets can now be calibrated at the JES. How the CalRatio trigger is affected will be discussed in Section 7.1.3.

7.1.2 Signal Samples

The benchmark model used in the 2015 analysis, a $\Phi \rightarrow ss$ decay, is functionally identical to that used in 2012. In contrast to the 2012 analysis the 2015 analysis was developed based on high mass Φ. This decision was made in order to develop a new background estimate in a region of phase space where NCB contributes less to the background. Specifically, the high mass samples allow for much higher cuts on the jet energy while still maintaining signal sensitivity.

The $\Phi \rightarrow ss$ signal samples were each produced with a proper lifetime such that the mean lifetimes of the LLPs in the lab frame (LF) is 5 m. For a few mass points samples with smaller statistics were also produced to have a LF mean lifetime of 9 m. These samples were used to validate the extrapolation of the limits to other lifetimes, a procedure that remained virtually unchanged from its 2012 iteration. Samples were generated using MadGraph and Pythia combined, rather than only Pythia as was done in 2012. Specifically, MadGraph5_aMC@NLO v2.2.3 [58] with the NNPDF23LO [59] PDF was interfaced with Pythia8 v8.210 [51]. The parton shower and hadronization was performed in Pythia. Geant4 is still used for simulation of particle interaction with ATLAS itself, using GEANT4 [52]. The mass points generated are summarized in Table 7.1.

Once again a set of SM multijet samples was used for various studies. These samples were produced with the Pythia8 using NNPDF23LO for the PDF.

7.1.3 Updates to CalRatio Trigger

The 2015 CalRatio trigger, `HLT_j30_jes_PS_llp_L1TAU60`, is similar in most respects to the 2012 trigger. It identifies signal jets by identifying high $\log_{10}(E_{\mathrm{H}}/E_{\mathrm{EM}})$ jets isolated from ID tracks. The $\log_{10}(E_{\mathrm{H}}/E_{\mathrm{EM}})$ cut remains unchanged, as do the cuts used by the BIB

m_Φ [GeV]	m_s [GeV]	LF=5 m		LF=9 m	
		$c\tau$ [m]	Events	$c\tau$ [m]	Events
400	50	0.700	400k	1.26	200k
	100	1.46	400k	2.64	200k
600	50	0.520	400k	0.960	200k
	150	1.72	400k	3.14	200k
1000	50	0.380	400k	0.670	200k
	150	1.17	400k	2.11	200k
	400	3.96	400k	7.20	200k

Table 7.1: Summary of the Φ and s mass and s lifetime parameters used in the simulation. Both the mean lifetime in the lab-frame (LF) and the sample proper ($c\tau$) lifetimes are listed.

removal algorithm. Nonetheless, several changes were made to the trigger to adapt it to the higher-energy environment present in ATLAS in 2015.

One of the most significant changes is the use of `L1_TAU60` instead of `L1_TAU30` at Level 1. The high rate of the 30 GeV L1 item forced migration to the 60 GeV item in order to avoid prescaling the trigger. This does limit the trigger's ability to identify lower energy signal-like jets, another reason for the first Run-II analysis to focus on high mass samples.

Another notable change was the use of *partial scan* jet reconstruction instead of *full scan* jet reconstruction. In partial scan reconstruction only a subset of the calorimeter, a *super RoI*, determined by the L1 object location, is available to the trigger both to reconstruct jets as well as for use in the BIB rejection algorithm. The super RoI was large enough to easily reconstruct jets, but the loss of access to cells far away from the jet limited the veto power of the BIB removal algorithm and necessitated the use of multiple NCB removal cuts offline despite the higher energy working point used by the analysis.

Jets were also calibrated to JES scale before cuts were applied. In 2012, trigger level cuts were applied to jets at the EM scale. The 35 GeV online (EM scale) cut in 2012 could be approximated by an 60 GeV (JES+corrections) offline cut. The 2015 trigger applies a 30 GeV at the *JES*. Naively, this should improve the trigger's ability to identify low energy signal-like jets, but as described above this is partially offset by the high L1 energy threshold.

Finally, whereas the 2012 trigger vetoed on $p_{\mathrm{T}} > 1$ GeV tracks within $\Delta R < 0.2$ of the jet axis, the 2015 trigger raised the track p_{T} cut to 2 GeV. This was done because the 2015 run conditions include higher pile-up and the trigger efficiency is sensitive to pile-up. The trigger cannot identify the PV, and therefor which tracks come from the PV and which are from pile-up. As a result random pile-up tracks that would be ignored offline can ruin the track isolation online.

Figure reffig:trigEff shows the trigger efficiency for several signal samples used in the 2015 analysis. In both the barrel and the endcap the efficiency improved over the efficiency for similar mass points in 2012 (Figure 5.3). The improvement to the efficiency is due in part to a the higher p_{T} cut on track isolation and the lower cut on jet energy.

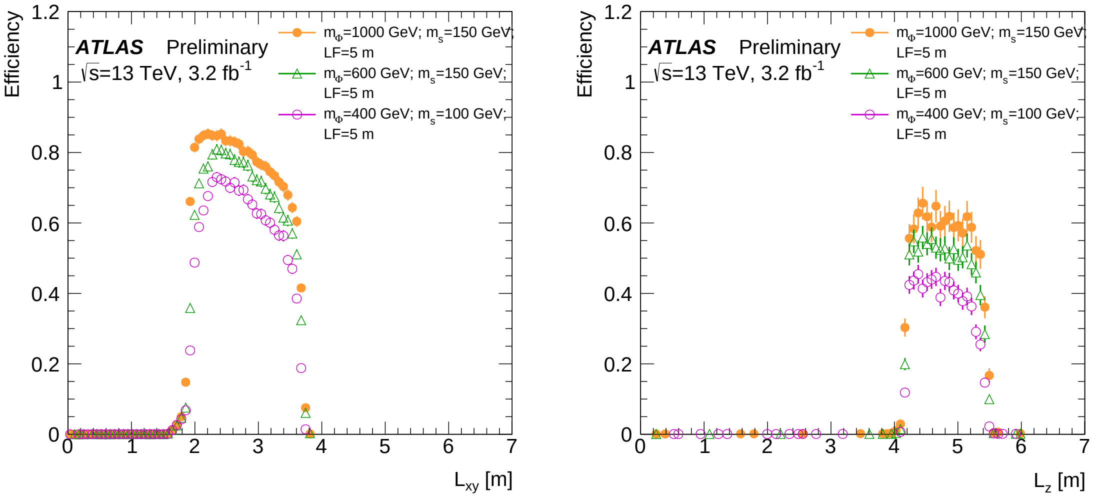

Figure 7.1: CalRatio trigger efficiency in the barrel (left) and endcaps (right) for several different signal samples.

As in 2012 several background triggers were used by the analysis. A CalRatio trigger on empty BCs was again used to study cosmic events. The number of unpaired isolated BCs per was sufficiently reduced compared to the 2012 run that the statistics were too low to use this dataset for analysis. Instead, a version of the CalRatio trigger running on filled BCs, but *without* the BIB removal algorithm, was used to gather BIB events for background studies.

7.1.4 Jet Cleaning

During the course of early studies of CalRatio triggered events in data it was discovered that the trigger was sensitive to LAr noise bursts. In order to remove these events offline a new jet cleaning cut was developed to be appended to the standard cleaning. The standard cleaning itself was very similar to the 2012 cleaning but no longer included a cut on jet timing. The new cut labels a jet as having poor quality if it satisfies $\mathrm{a}bs(negativeE) < 4GeV$ & $FracSamplingMax > 0.85$, where $negativeE$ is the negative energy component of the total jet energy and $FracSamplingMax$ is the maximum fraction of the total energy contained in a single layer of the calorimeter. Signal jets may have their energy concentrated mostly in one layer in the case of very late decays, but they have a small amount of negative energy. The DQ criteria used by the analysis still bypasses any standard cut on low EMF jets.

7.2 CalRatio BDT

The analysis of 2015 data replaced the set of linear cuts used to identify candidate signal events with a boosted decision tree (BDT) [60, 61]. A BDT takes as input several variables for an object, in this case a jet, and compares them in two or more samples to identify regions of the parameter phase space that have a higher density of objects from signal compared to background. The CalRatio analysis used a full set of signal samples and the SM multijet background sample for the training. The BDT assigns a BDT value to each jet where positive values indicate the jet is more signal-like and negative values indicate that it is more background-like. For the training only each signal sample was weighted by its p_{T} to have a flat p_{T} spectrum. A total of thirteen variables, including the jet p_{T}, were used to train the BDT. Included are both parameters of the jet and of its *leading* cluster. They are listed here in descending order of their importance as determined by the training algorithm:

1. $\log_{10}(E_{\mathrm{H}}/E_{\mathrm{EM}})$
2. Jet width - The p_{T} weighted sum of the ΔR between each of the jet's clusters and the jet axis.
3. Cluster longitudinal length - A measure of the cluster's spread along the jet axis
4. Jet p_{T}- The p_{T} of the jet. Events are reweighted to flatten the jet p_{T} distribution, allowing the BDT to identify correlations between other parameters and p_{T} without relying directly on p_{T} (which has a sample and lifetime dependence)
5. Cluster lateral width - A measure of the cluster's spread perpendicular to the jet axis.
6. Cluster shower center λ - The distance along the jet axis to the shower center as measured from the *inner edge of the ECal*.
7. ΔR to Nearest $p_{\mathrm{T}} > 2$ GeV Track - Default of 0.4 if there is no $p_{\mathrm{T}} > 2$ GeV track is found.
8. Cluster shower center r - The distance to the shower center as measured *from the IP*.
9. Cluster energy density - The $\frac{\sum E_i^2/V_i}{\sum E_i}$, where E_i is the energy of each cell, and V_i is the volume of the cell. The sums are over each cell with positive energy in the cluster.
10. Number of tracks - The number of tracks with $p_{\mathrm{T}} > 2$ GeV within a $\Delta R < 0.2$ radius of the jet axis.
11. Sum p_{T} of tracks - The sum of the p_{T} of all tracks within $\Delta R < 0.2$.

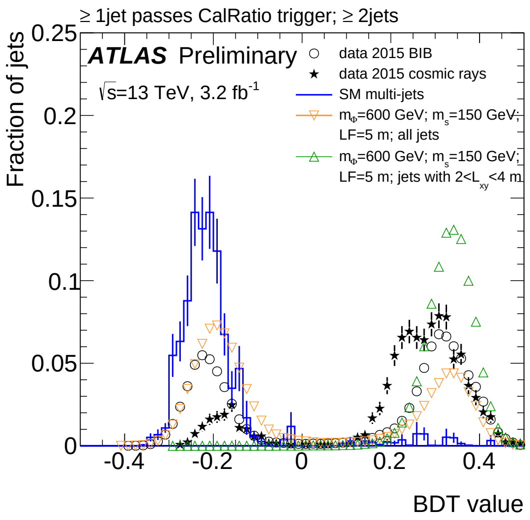

Figure 7.2: BDT value distribution in events passing the CalRatio trigger, for data BIB, cosmic ray muons, SM multijet MC, and a single sample with both the distribution for all jets and that for only jets with $2 < L_{xy} < 4$ m, where L_{xy} is the transverse decay length of the LLP. The error bars show the statistical error for each bin.

12. Layer 1 energy fraction - The fraction of the hadronic calorimeter's energy located in the innermost HCal layer. This value will be small for LLPs decaying late within the HCal.

13. Max track p_T- The maximum p_T of all tracks within $\Delta R < 0.2$.

Figure 7.2 shows the output from the BDT for several samples. The two signal sample distributions are both from the $m_\Phi = 600\mathrm{GeV}$, $m_\mathrm{s} = 150\mathrm{GeV}$ sample. The orange downwards-pointing triangles show the BDT for all jets in the sample, while the green upwards-pointing triangles show the BDT for jets with a LLP decaying in the HCal barrel. Jets from LLPs decaying in the HCal usually have a high BDT value, while more prompt decays tend to look background-like to the BDT. NCB, which the BDT was not trained against, tends to produce signal-like jets as well.

7.3 Event Selection

As in the 2012 analysis events are required to fire the CalRatio trigger and pass all event level DQ criteria. The two jets in the event with the highest BDT values were required to satisfy the LLP DQ clean jet criteria and have $|\eta| < 2.5$. The higher BDT jet was required to have a BDT value of at least 0.2 and satisfy $p_{\mathrm{T}} > 150$ GeV. The second jet was required to have a BDT value of at least 0.2 and satisfy $p_{\mathrm{T}} > 120$ GeV. The higher p_{T} cuts were chosen to reduce the impact of NCB, allowing for the first implementation by the analysis of the ABCD method for estimating the background. These high p_{T} cuts do limit the analysis sensitivity to signal from decays of lighter particles. Finally, the jets and event were required to pass the series of additional cuts described in Section 7.4.1 to reduce NCB contamination. Jets in events passing all the above cuts, excepting the use of a lower p_{T} cut ($p_{\mathrm{T}} > 50$ GeV) on both jets, are referred to as *candidate signal jets*.

7.4 Background Estimation

The 2015 analysis simplified the background estimation from that used in 2012. Rather than estimating the three backgrounds separately, a data-driven method that looks at all backgrounds together was used. The ABCD method [62] is performed after a series of cuts are used to remove NCB events.

7.4.1 NCB Removal

The higher jet p_{T} cuts used in the 2015 analysis compared to the 2012 analysis play a major role in reducing the NCB background. Nonetheless, additional cuts are still needed to reduce the background to an acceptable level for the application of the ABCD method. As in 2012, several cuts are used in combination to reduce the NCB. Unlike in 2012, the NCB backgrounds were not estimated separately: if a pair of (after all other cuts are applied) *uncorrelated* variables is chosen for the ABCD method it will estimate the total background, not just the background from collision sources.

Due to the impact of the $E_{\mathrm{T}}^{\mathrm{miss}}$ cut on the analysis sensitivity to high energy jets it was replaced for the 2015 analysis with a cut on $H_{\mathrm{T}}^{\mathrm{miss}}/H_{\mathrm{T}}$, where H_{T} is the scalar sum of jet p_{T} for all jets in the event with $p_{\mathrm{T}} > 30$ GeV and $|\eta| < 3.2$ and $H_{\mathrm{T}}^{\mathrm{miss}}$ is the magnitude of the negative vectorial sum of the same jets. This change both considers only the jet contribution to the $E_{\mathrm{T}}^{\mathrm{miss}}$ and allows for larger $E_{\mathrm{T}}^{\mathrm{miss}}$ when there are higher energy jets in the event. The timing cut was likewise broadened to reduce the rejection of slow moving LLPs. Additionally, a cut on the $\Delta\phi$ between the two jets was added due to the tendency of BIB events to contain multiple jets at similar values of ϕ.

Figure 7.3 shows the jet p_{T} and event $H_{\mathrm{T}}^{\mathrm{miss}}/H_{\mathrm{T}}$ distributions on the left and right, respectively, for events from the BIB dataset, the SM multijet MC, and a signal sample. Figure 7.4 displays the timing distribution on the left and the $\Delta\phi$ distribution on the right for several samples. The $\Delta\phi$ distribution is for the pair of jets with the highest BDT value. In all cases the distributions are for candidate signal jets - the higher p_{T} cuts are not yet applied.

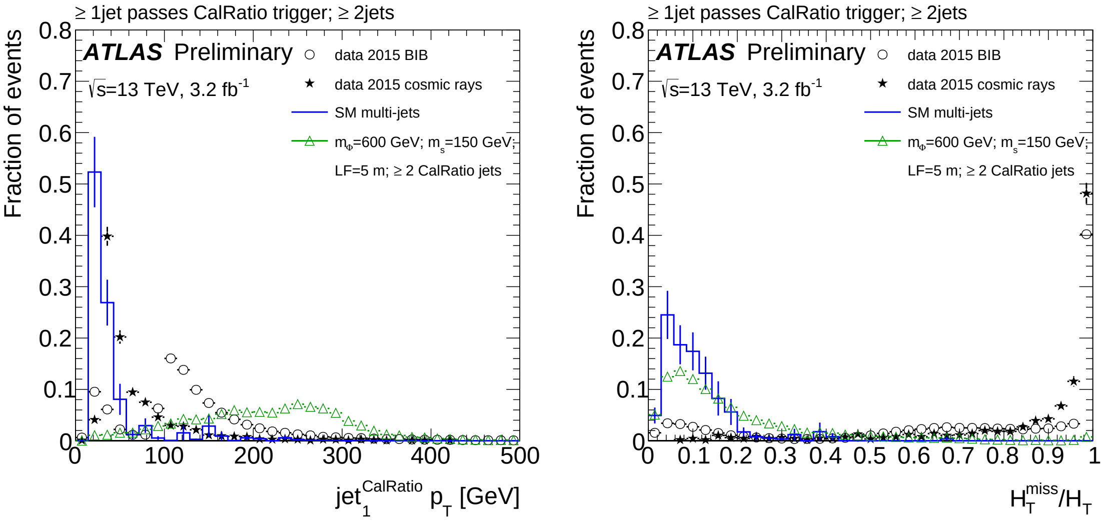

Figure 7.3: Jet p_{T} distribution (left) and event $H_{\mathrm{T}}^{\mathrm{miss}}/H_{\mathrm{T}}$ (right) for several different samples. The high Φ and s mass of the signal samples result in high p_{T} jets from decays of the s in the calorimeter. Event $H_{\mathrm{T}}^{\mathrm{miss}}/H_{\mathrm{T}}$ scales with jet energy, resulting in lower values even for events with punchthrough jets compared to BIB events.

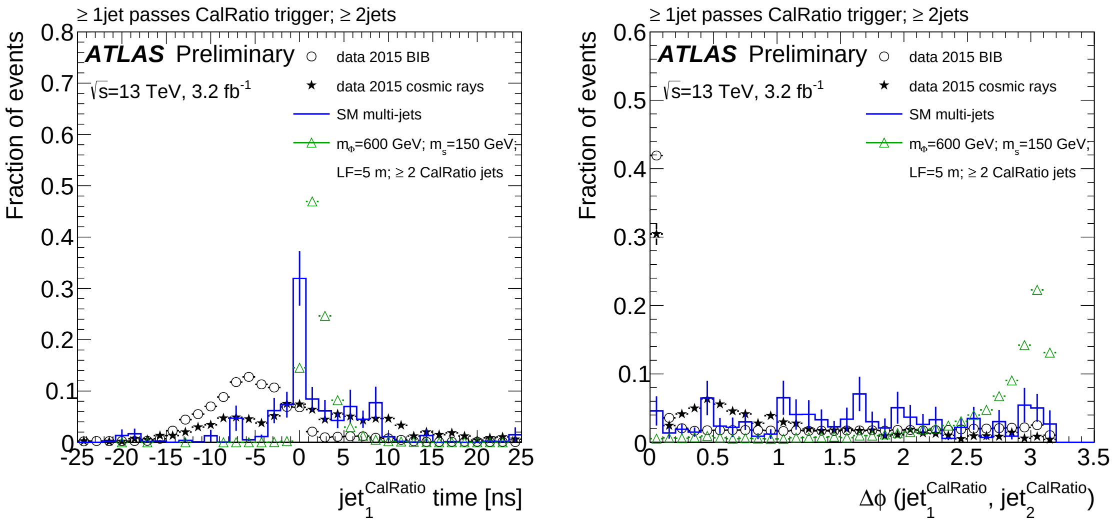

Figure 7.4: Jet timing distribution for the jet with the highest value osf BDT in the event (left) and the $\Delta\phi$ distribution for the two jets with the highest BDT values (right) for BIB jets, cosmic ray muons, QCD MC and signal. Only signal MC events with two candidate jets are shown.

The final jet selection chosen to reject NCB is:

- $\Delta\phi(BDT_1, BDT_2) > 0.75$
- $H_{\mathrm{T}}^{\mathrm{miss}}/H_{\mathrm{T}} < 0.3$
- $-3 < \mathrm{t} < 15$ ns

These cuts were chosen to be as loose as possible while still removing the correlation added to the ABCD place by NCB events.

7.4.2 Application of ABCD Method

The ABCD method is a data-driven method for estimating the total background to a search. The method divides the plane defined by two *uncorrelated* variables into three regions, labeled A, B, C, and D. Signal should be confined to one region, traditionally that labeled A. This allows for the prediction of the number of background events in region A (N_A) based on the number of events in each of the other three regions (N_B, N_C, N_D):

$$N_A = \frac{N_B \times N_C}{N_D} \tag{7.1}$$

The analysis uses a modified version of the ABCD analysis that is appropriate for use when signal contamination outside of region A is a concern. In this method the background and signal are fit simultaneously. The application of this modified method will be discussed in Section 7.5.

The two variables chosen to define the ABCD plane were $\sum BDT$ and $\sum min\Delta R(jet, tracks)$. $\sum BDT$ is the sum of the BDT values of the two jets with the highest BDT, which are necessarily the candidate signal jets. The second variable, $\sum min\Delta R(jet, tracks)$, is the sum of the distance between each $p_{\mathrm{T}} > 50$ GeV jet and closest track with $p_{\mathrm{T}} > 2$ GeV. This sum is performed for all jets in the event, not only the two jets with the highest BDT value.

Figure 7.5 and Figure 7.6 show the distributions of these variables for several samples before and after application of the NCB cuts, respectively. The peak at higher $\sum BDT$ for signal corresponds to events in which both LLPs decay in the HCal. BIB produces jets very similar to signal jets, but the NCB cuts remove nearly all BIB events in the higher peak. The BDT was trained to reject SM mutlijet events, these events tend towards low $\sum BDT$. They are not included in the $\sum BDT$ plot, however, due to their very poor statistics after other cuts have been applied. SM multijet events also usually produce jets with associated tracks, resulting in a small $\sum min\Delta R(jet, tracks)$. Signal jets and NCB, on the other hand, produce jets without associated tracks.

Figure 7.7 shows the ABCD plane for the SM multijet MC sample on the left and a signal sample on the right. The SM MC sample is not used in the background estimation, but is included in the figure to illustrate the separation between signal and the multijet background. The correlation in events with at least two candidate signal jets is about 8%, while that in the SM multijet MC sample is about 12%. While not ideal, this correlation is sufficiently low to apply the ABCD method.

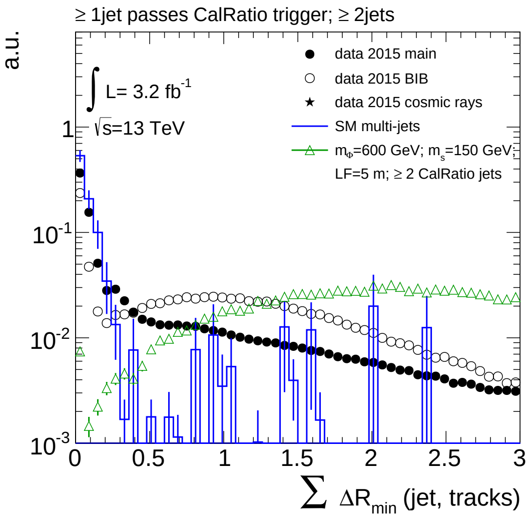

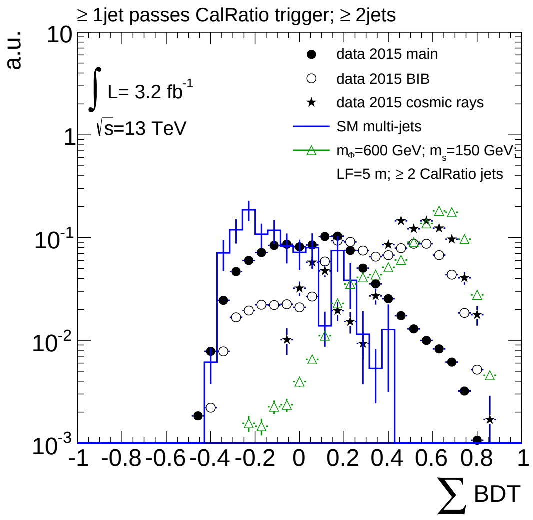

Figure 7.5: The $\sum minΔR(jet, tracks)$ (left) and $\sum BDT$ (right) distributions for jets from the main, BIB, cosmic ray, SM multijet, and example signal samples before application of the NCB cuts. Only signal MC events with two candidate signal jets are shown.

During the calculation of the systematic associated with the application of the ABCD method a new correlation was observed at low $\sum minΔR$ for a separate dijet sample. For this reason the cut $\sum minΔR > 0.5$ is included in the cut flow. This cut has no effect on the low observed correlation in the analysis plane.

Figure 7.8 shows the ABCD plane divided into its four regions. The plot on the left shows the distribution for a signal sample with only jets decaying in the HCal displayed. The plot on the right shows the distribution from the same sample with all LLP jets included. There is sufficient signal contamination outside of the signal region to motivate the use of the modified ABCD method. This method is applied during limit calculation and will therefore be discussed in Section 7.5.

7.5 Results and Systematics

The systematics associated with the 2015 analysis are similar to those associated with the 2012 analysis. The 2015 analysis was considered preliminary, so certain systematics expected

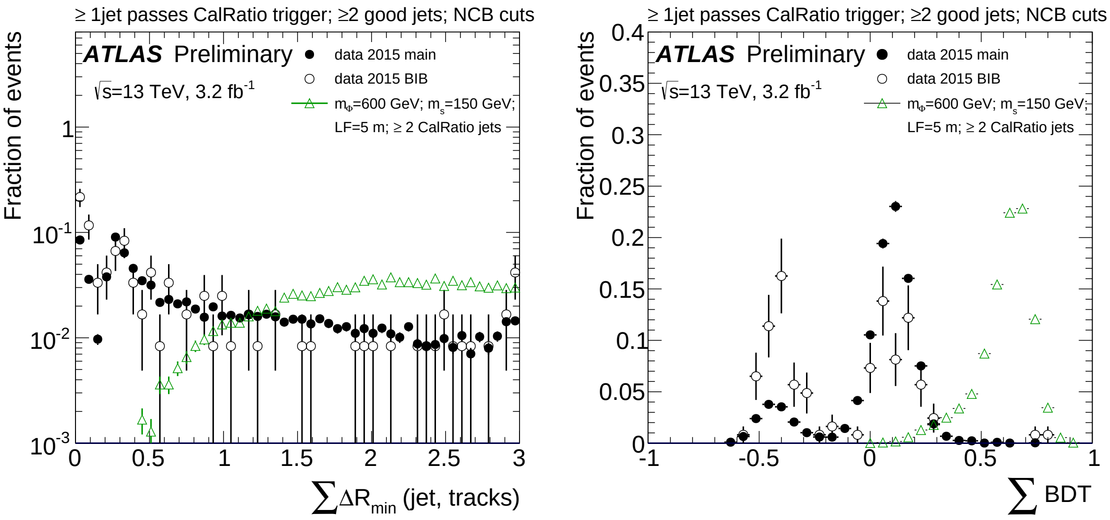

Figure 7.6: The $\sum min\Delta R(jet, tracks)$ (left) and $\sum BDT$ (right) distributions for jets from the main, BIB and example signal samples. The NCB cuts leave too few events in the cosmic and SM multijet samples to include them in the plots. Only signal MC events with two candidate signal jets are shown.

to be small, such as the ISR systematic, were not re-evaluated. Their full evaluation will be part of the analysis on 2016 data. The uncertainties included in the 2015 analysis are summarized in Table 7.4.

7.5.1 ABCD Systematics

The systematic uncertainty associated with the application of the ABCD method was evaluated using a dijet enriched sample to study the sensitivity of the ABCD plane to the location of the region boundaries. For each choice of boundaries the discrepancy between the estimated and observed number of events is recorded. The maximum deviation is taken as the uncertainty.

Large statistics are needed for this method to be valid. The discrepancy taken as the systematic will always have some statistical component, but large statistics suppress this contribution. A set of cuts was chosen to match those used by a search for new physics in

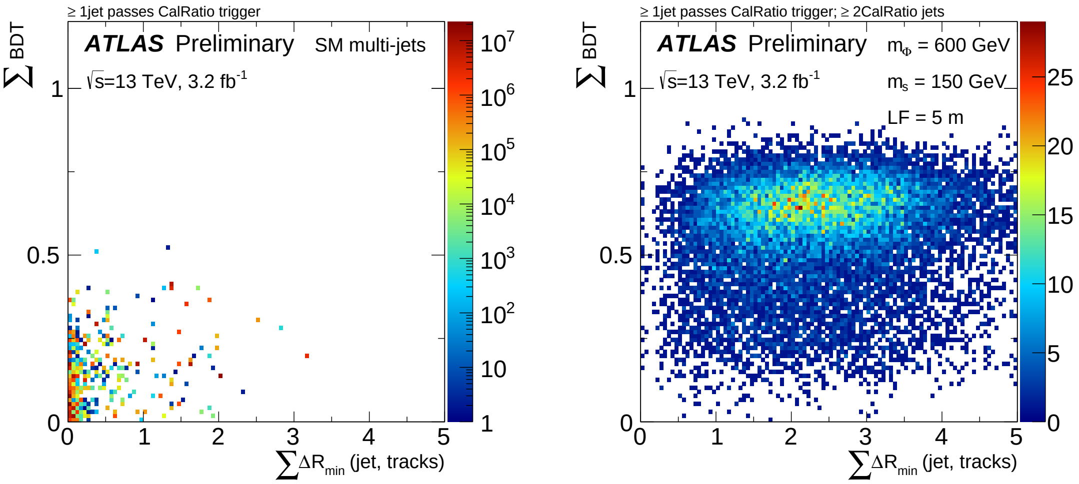

Figure 7.7: The ABCD plane, $\sum min\Delta R(jet, tracks)$ vs. $\sum BDT$, distributions for SM multijet MC (left) and signal MC (right). The signal distribution includes only with two candidate signal events.

dijet events and are as follows:

- The HLT_j400 trigger.
- At least 2 good DQ jets with $p_{\mathrm{T}} > 60$ GeV.
- $p_{\mathrm{T}}(jet_1) > 400$ GeV.
- $|\Delta\phi(jet_1, jet_2)| > 3.0$.
- $(p_{\mathrm{T}}(jet1) - p_{\mathrm{T}}(jet2))/(p_{\mathrm{T}}(jet1) + p_{\mathrm{T}}(jet2)) < 0.3$.
- Event must not satisfy a logical OR of the following conditions: Missing$H_T > 120$ GeV, $|time(jet_1)| > 2.5$, $|\Delta\phi(\mathrm{jet}_1, \mathrm{MHT}|) > 3.0$, where Missing H_T is the magnitude of the negative vectorial sum of all the jets with $p_{\mathrm{T}} > 30$ GeV in the event.

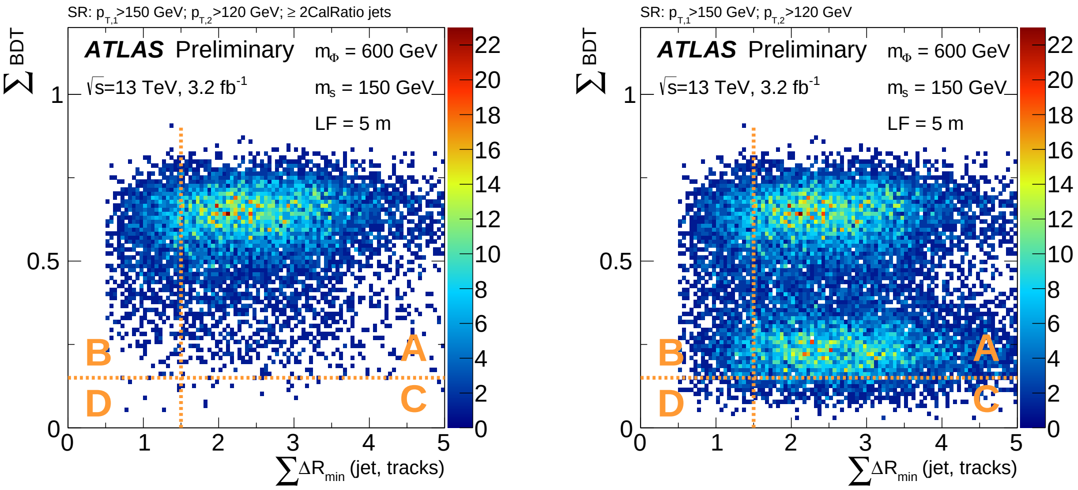

Figure 7.8: The ABCD plane, $\sum min\Delta R(jet, tracks)$ vs. $\sum BDT$, distributions for SM multijet MC (left) and signal MC (right). The signal distribution includes only with two candidate signal events.

Table 7.2 shows the predicted and observed number of events for different choices of region boundaries in the ABCD plane of the dijet sample. Statistics are sufficient to maintain the statistical error at less than 10% for every boundary choice. The systematic is taken as the largest discrepancy between the predicted and observed number of events, 36%.

7.5.2 Luminosity

The uncertainty in the integrated luminosity is ±2.1%. It is derived, following a methodology similar to that detailed in Refs. [49] and [50], from a calibration of the luminosity scale using x-y beam-separation scans performed in August 2015.

7.5.3 Jet Energy Scale

The standard JES systematic is determined using a recommended tool for ATLAS analyses. The energy of the jets is varied for each of four reduced uncertainty set and the effect on the acceptance is observed. The results are similar for all four samples so the results obtained

$\sum BDT$, $\sum Min\Delta R$	A_{obs}	B	C	D	$A_{\text{est}} = BC/D$	$\sigma_{\text{stat}}/A_{\text{est}}$	$\lvert 1 - (A_{\text{est}}/A_{\text{obs}})\rvert$
−0.30, 1.25	195	137	500	490	140 ± 14.9	0.11	0.28
−0.35, 1.25	287	251	408	376	272 ± 26	0.10	0.05
−0.40, 1.25	428	404	267	223	484 ± 50	0.10	0.13
−0.30, 1.50	163	169	407	583	118 ± 11.9	0.10	0.28
−0.35, 1.50	240	298	330	454	217 ± 20.1	0.09	0.10
−0.40, 1.50	355	477	215	275	373 ± 38	0.10	0.05
−0.30, 1.75	140	192	316	674	90 ± 8.94	0.10	0.36
−0.35, 1.75	196	342	260	524	170 ± 15.8	0.09	0.13
−0.40, 1.75	281	551	175	315	306 ± 31.7	0.10	0.09

Table 7.2: The number of events in each region and the predicted number of events obtained via the ABCD method to the dijet sample. All cuts including the NCB cuts and $\sum Min\Delta R > 0.5$ are applied. The observed number of cuts in region A is A_{obs}, the estimated number is A_{est}, and the statistical uncertainty on the estimate is σ_{stat}.

with the parameter set using the fewest number of parameters is taken as the standard JES uncertainty.

This uncertainty is combined with the recalculated JES uncertainty for low EMF jets (Section 5.4.7). The procedure for 2015 data was repeated by the Lepton-Jet analysis [63]. The two JES uncertainties are separately calculated for each sample. This results in some overestimation of the uncertainty: low EMF jets are included in both estimations. Both results are included in Table 7.4.

7.5.4 Jet Energy Resolution

The uncertainty associated with the jet energy resolution is determined with a standard tool. The tool was developed using a dijet balance technique similar to that used for the standard JES systematic tool. For the jet energy resolution the widths of the asymmetry peaks are compared in MC and data.

7.5.5 Trigger

As in 2012 the uncertainty associated with the modeling of the trigger was calculated separately for each cut: E_{T}, $\log_{10}(E_{\mathrm{H}}/E_{\mathrm{EM}})$, and the track p_{T} used for track isolation. The 2015 procedure does differ from the 2012 procedure. Data and MC distributions are compared for each of the three trigger cuts to determine a scale factor. The scale factor is then applied to a emulation of the trigger in the MC samples to determine the systematic.

A tag-and-probe method is used to identify clean multijet events in MC and data using events selected by a series of b-jet triggers: `HLT_j35_bperf`, `HLT_j45_bperf`, `HLT_j55_bperf`, `HLT_j85_bperf`, `HLT_j110_bperf`, `HLT_j150_bperf`. The b-jet triggers are chosen to ensure that tracking is run in each selected event. The events are also required to pass the same L1 tau trigger used by the CalRatio trigger. This requirement ensures that the first stage of the jet reconstruction used by the CalRatio trigger is run, allowing the same type of jet (partial scan jets with the same trigger level calibration) to be used for the systematic calculation.

The tag jet is an offline jet required to satisfy:

- Is the leading jet.
- Matches a triggering HLT jet.
- $E_{\mathrm{T}} > 20$ GeV
- $|\eta| < 2.5$
- Is a good quality jet.

The probe jet is an offline jet required to satisfy:

- Is the subleading jet.
- Matches an HLT jet used by the CalRatio trigger.

- $E_{\mathrm{T}} > 20$ GeV
- $|\eta| < 2.5$
- Is a good quality jet.
- $\Delta\phi(tag, probe) > 2.0$

The MC and data distributions of each trigger parameter are compared by taking the ratio of the offline quantity to the online quantity and comparing the mean of this distribution in MC and data. The means are constant as a function of the online quantity, allowing a single mean to be used. A scale factor is calculated for each parameter as the amount by which the MC HLT parameter should be shifted such that the mean in MC is equal to that in data. These scale factors are listed in Table 7.3.

$\mathrm{SF}_{\mathrm{ET}}$	$\mathrm{SF}_{\mathrm{log}}$	$\mathrm{SF}_{\mathrm{trkpT}}$
1.00 ± 0.10	1.04 ± 0.16	1.03 ± 0.30

Table 7.3: The scale factor that should be applied to each HLT parameter to bring its ratio of the offline and online values of the parameter in MC equal to that in data.

The scale factors are applied separately to a cut-by-cut emulation of the CalRatio trigger and the effect on the acceptance is taken as the uncertainty. Only the $\log_{10}(E_{\mathrm{H}}/E_{\mathrm{EM}})$ uncertainty is significant. The offline cut applied to the jet energy is sufficiently high to suppress the effects of any mismodeling of the cuts on that parameter. The trigger is additionally much more sensitive to small changes (or mismodeling) in the $\log_{10}(E_{\mathrm{H}}/E_{\mathrm{EM}})$ of the jet than to similarly small changes in the p_{T} of the tracks. The combined trigger uncertainty is included in Table 7.4.

Mass Point (GeV, GeV)	JES (%)	JES EMF (%)	JER (%)	Trigger (%)	Pile-up (%)	Luminosity (%)
(400,150)	3.3	14	0.43	2.3	4.0	2.1
(600,150)	1.5	5.4	0.40	1.5	0.56	2.1
(1000,150)	0.51	1.8	0.05	1.0	2.0	2.1

Table 7.4: Summary of the signal systematic uncertainties at the three reference mass points are shown. The systematic uncertainties are driven by the mass of Φ, so for mass points with the same m_Φ they are taken to be the same. The only systematic uncertainty not shown in the table is the one connected with the ABCD method, 36%, and is applied to the background model only.

7.5.6 Pile-up uncertainty

The pile-up uncertainty in 2012 was determined with a study of pile-up dependence in data and MC of the dependence of various parameters on the pile-up. In 2015, this procedure was replaced with an ATLAS standard procedure. Studies comparing the number of vertices found in MC and data for the same value of μ revealed a mismodeling in the MC. This is corrected with the application of a scale factor, $1.16^{+0.07}_{-0.16}$, to the pile-up weight in MC events. To determine the systematic the scale factor is varied by its uncertainty. The variation in the final acceptance is taken as the uncertainty. The results are included in Table 7.4.

7.6 Application of Full Cut Flow

Table 7.5 shows the number of events surviving each stage of the cut flow for only those events with two LLPs decaying in the HCal for several signal samples. The acceptance for such events ranges between 23% for samples with less-boosted LLPs and 50% for samples with highly energetic LLPs. Table 7.6 shows the same information, but for events in the sample. Although all three samples have the same mean lifetime in the lab frame the trigger selects a larger portion of the events from samples with higher energy jets.

(m_ϕ, m_s) [GeV]	1000, 150	600, 150	400, 100
		LF = 5 m	
Events passing the trigger	90.1%	83.3%	74.2%
≥ 2 good DQ jets	86.5%	79.7%	70.2%
Good DQ for 2 highest BDT jets	74.4%	66.7%	59.1%
$\Delta\phi > 0.75$	74.1%	65.8%	58.1%
$-3 <$ time < 15 ns	74.1%	65.7%	58.1%
$H_{\mathrm{T}}^{miss}/H_{\mathrm{T}} < 0.3$	63.1%	57.9%	52.4%
$\sum min\Delta R > 0.5$	62.9%	57.8%	52.3%
B$DT\ value(\mathrm{jet}_1^{\mathrm{CalRatio}}) > 0.2$	62.7%	57.6%	52.1%
B$DT\ value(\mathrm{jet}_2^{\mathrm{CalRatio}}) > -0.2$	62.7%	57.5%	52.1%
$p_{\mathrm{T},1} > 150$ GeV	60.9%	50.6%	32.0%
$p_{\mathrm{T},2} > 120$ GeV	60.3%	48.4%	27.8%
region A:			
$\sum min\Delta R > 1.5$	50.8%	41.3%	23.8%
$\sum BDT > 0.15$	50.7%	41.2%	23.7%

Table 7.5: Impact of the analysis selection criteria as applied in the SR definition taking into account events where both LLPs decay in the HCal.

Table 7.7 shows the cut flow as applied to several samples studied by the analysis. The values listed for the signal are the percentage of the total number of events surviving each stage of the cut flow. For the NCB, the percentages are of the total number of events firing the corresponding trigger. The “Data main” column shows the actual number of events from the CalRatio triggered dataset surviving that stage of the cut flow. Finally, the “SM multijet MC” shows the number of events in the full SM multijet MC sample. Only the values in the “Data main” column enter into the background estimate and associated systematic.

The NCB cuts eliminate all events from the NCB samples. It is possible some NCB

(m_ϕ, m_s) [GeV]	1000, 150	600, 150	400, 100
		LF = 5 m	
Events passing the trigger	30.4%	25.7%	19.9%
≥ 2 good DQ jets	26.2%	22.1%	16.9%
Good DQ for 2 highest BDT jets	9.63%	7.21%	5.2%
$\Delta\phi > 0.75$	9.4%	6.85%	5.06%
$-3 <$ time < 15 ns	9.38%	6.84%	5.04%
$H_{\mathrm{T}}^{\mathrm{miss}}/H_{\mathrm{T}} < 0.3$	8.14%	6.09%	4.56%
$\sum \Delta \mathrm{R}_{\mathrm{min}} > 0.5$	8.13%	6.08%	4.56%
BDT value(jet$_1^{\mathrm{CalRatio}}$) > 0.2	7.97%	5.95%	4.49%
BDT value(jet$_2^{\mathrm{CalRatio}}$) > -0.2	7.96%	5.93%	4.46%
$p_{\mathrm{T},1} > 150$ GeV	7.76%	5.31%	2.95%
$p_{\mathrm{T},2} > 120$ GeV	7.18%	4.27%	2.01%
region A:			
$\sum \Delta \mathrm{R}_{\mathrm{min}} > 1.5$	6.26%	3.73%	1.74%
$\sum \mathrm{BDT} > 0.15$	6.02%	3.57%	1.66%

Table 7.6: Impact of the analysis selection criteria as applied in the SR definition taking into account all events in each sample.

events remain in the main CalRatio triggered data sample, but any which do are sufficiently similar to the SM multijet background that the ABCD method can incorporate them into its estimate. If this were not the case a larger correlation would exist in the ABCD plane.

7.7 Limits

A total of 24 events are observed in data after applying the full cut flow. The background prediction from the ABCD method is 18.4 ± 6.3 (stat) ± 6.6(syst) events. No excess of events is found in the data and 95% confidence limits are therefor set on the LLP lifetimes.

Requirement	Data Main	SM Multijet MC	$m_\phi = 600$ GeV $m_\mathrm{s} = 50$ GeV	Data BIB	Data Cosmic
Events passing the trigger	548600 ± 740	404000 ± 27000	25.7%	100%	100%
≥ 2 clean jets	421800 ± 650	197000 ± 19000	22.1%	38.3%	21%
$\mathrm{jet}_{1,2}^{\mathrm{CalRatio}}$ clean	23860 ± 150	900 ± 440	7.21%	6.67%	7.28%
$\Delta\phi > 0.75$	17590 ± 130	600 ± 350	6.85%	0.86%	3.38%
$-3 < \mathrm{time} < 15$	16180 ± 130	600 ± 350	6.84%	0.35%	1.10%
$H_\mathrm{T}^\mathrm{miss}/H_\mathrm{T} < 0.3$	14880 ± 120	600 ± 350	6.09%	0.30%	0.25%
$\sum \Delta\mathrm{R}_\mathrm{min} > 0.5$	9500 ± 97	500 ± 330	6.08%	0.14%	0.25%
BDT value($\mathrm{jet}_1^{\mathrm{CalRatio}}$) > 0.2	8190 ± 91	500 ± 330	5.95%	0.09%	0.25%
BDT value($\mathrm{jet}_2^{\mathrm{CalRatio}}$) > -0.2	4890 ± 70	300 ± 260	5.93%	0.06%	0.25%
$p_{\mathrm{T},1} > 150$ GeV	330 ± 18	0 ± 0	5.31%	0.005%	0%
$p_{\mathrm{T},2} > 120$ GeV	110 ± 10	0 ± 0	4.27%	0.001%	0%
region A:					
$\sum \Delta\mathrm{R}_\mathrm{min} > 1.5$	60 ± 8.0	0 ± 0	3.73%	0%	0%
$\sum \mathrm{BDT} > 0.15$	24 ± 4.9	0 ± 0	3.57%	0%	0%

Table 7.7: Impact of the application of the selection criteria on the fraction of generated events in the SR definition. The cross-section of the SM multi-jet MC sample is scaled to 3.2 fb^{-1}. Only statistical uncertainties are shown.

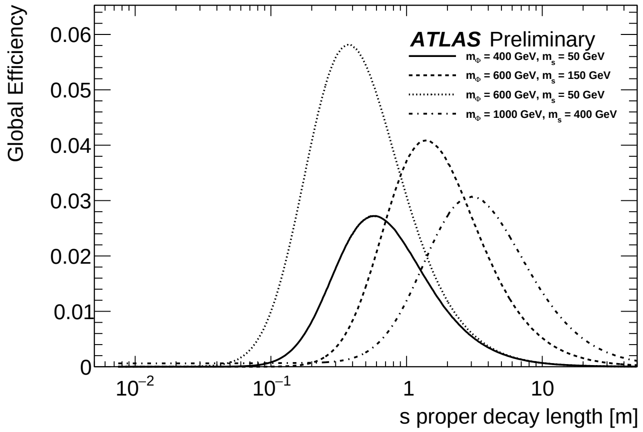

Figure 7.9: The efficiencies as a function of proper lifetime of the $\pi_{\rm v}$ for several different MC samples. The statistical error on the efficiency and extrapolation is approximately 1% when close to the generated lifetime increasing to about 2% at the large lifetimes.

The standard ABCD method assumes no signal contamination, but Figure 7.8 shows that a non-negligible amount of signal contamination is expected outside of the signal region (region A). A modified ABCD method is therefor used during limit setting. In the modified method a simultaneous fit is performed in regions B, C, and D for both the signal and background. The fit includes the fractional signal contamination predicted by the signal sample. The limit setting proceeds with the CLs method as in 2012, but with a signal strength parameter accounting for the contamination in each region.

As in 2012 the signal efficiency must be extrapolated as a function of lifetime. In 2012, this extrapolation was performed without any accompanying cross-check. In 2015, extra samples were produced at a second lifetime to allow for validation of the extrapolation. In all cases the actual efficiency at the cross-check lifetime was within the statistical error (about 2%) of the extrapolated efficiency.

Figure 7.9 shows the efficiency as a function of lifetime for select signal samples. The efficiency is higher for both more boosted LLPs and for higher mass LLPs. This is due primarily to the offline cuts on the transverse energy.

	$m_{\mathrm{s}} = 50$ GeV	$m_{\mathrm{s}} = 100$ GeV	$m_{\mathrm{s}} = 150$ GeV	$m_{\mathrm{s}} = 400$ GeV
	Decay length range excluded at 95% CL for $\sigma\times$ BR = 1 pb			
$m_{\Phi} = 400$ GeV	(0.20, 2.4) m	(0.52, 4.6) m	–	–
$m_{\Phi} = 600$ GeV	(0.09, 2.7) m	–	(0.38, 8.2) m	–
$m_{\Phi} = 1$ TeV	(0.05, 2.0) m	–	(0.14, 7.2) m	(0.78, 16) m

Table 7.8: Range of the s proper decay length excluded at 95% CL for all samples studied, assuming a 1 pb production cross-section and a 100% BR for $\Phi \rightarrow \pi_{\mathrm{v}}\pi_{\mathrm{v}}$.

The limits were calculated much as in the 2012 analysis. The produced limit plots are displayed in Figure 7.10. Table 7.8 list the excluded lifetimes assuming a production cross-section of 1 pb. The excluded limits at this cross-section are as small as 5 cm for the m_{Φ} = 1TeV, m_{s} = 2.0GeV sample to as high as 16 m for the m_{Φ} = 1TeV, m_{s} = 2.0GeV sample.

These limits cannot be easily compared to the 2012 limits, even at similar mass points. This is due in part to the unknown production cross-section for the Φ at the different center of mass energies. However, the global efficiencies are greatly improved. This is thanks to the improved trigger efficiency, to the alteration of the $E_{\mathrm{T}}^{\mathrm{miss}}$ cut, and to the improved means of identifying signal-like jets with the BDT. Furthermore, the much simpler background estimation simplifies and streamlines the analysis. While the analysis is not yet at the point where it can search for any combination of a high $\log_{10}(E_{\mathrm{H}}/E_{\mathrm{EM}})$ jet with another object, expanding its scope, it is now in a state where such a long-term goal can be worked on directly.

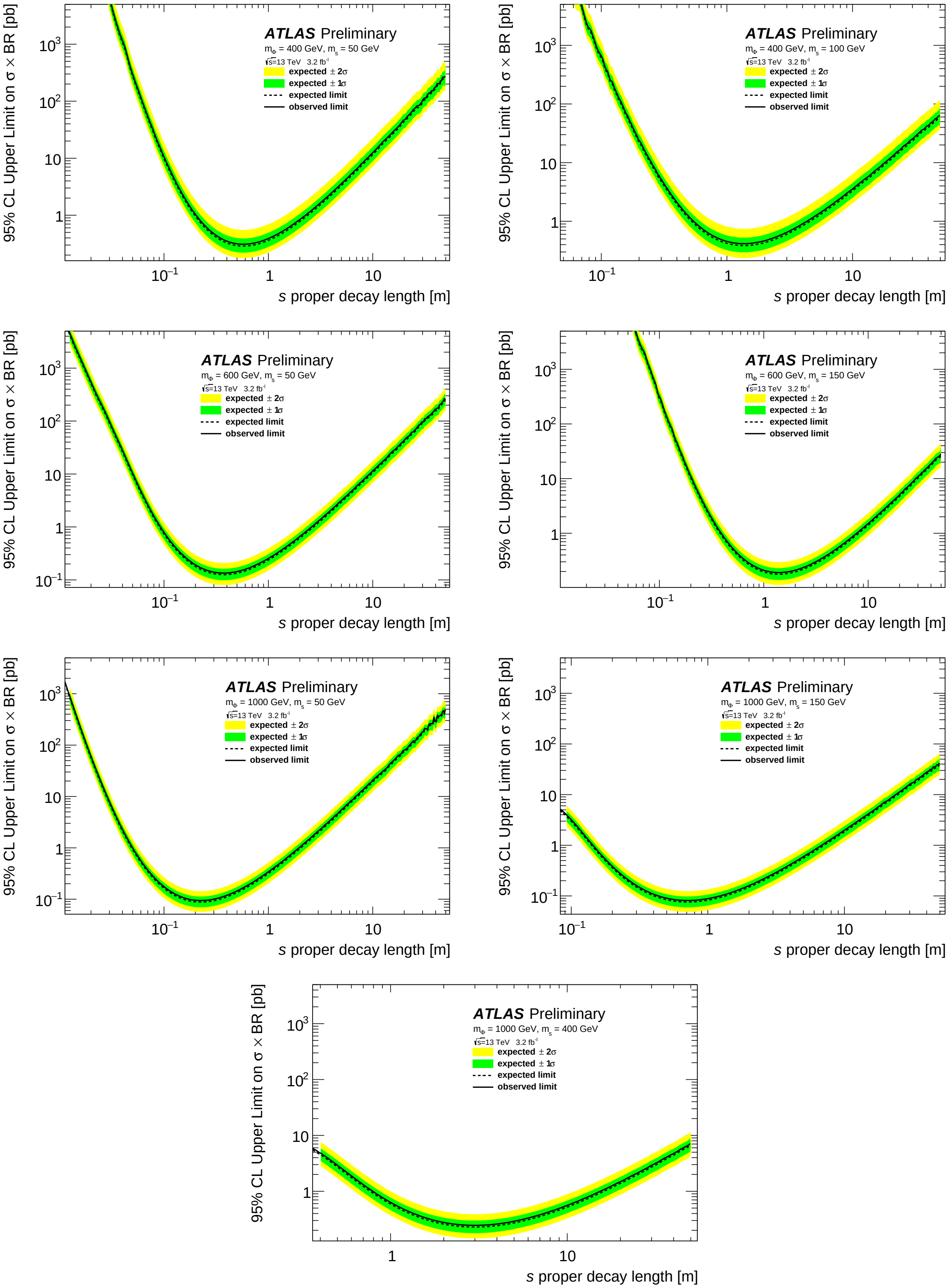

Figure 7.10: The expected, observed and ±1 and 2 sigma bands for the ϕ masses of $400, 600$, and 1000 GeV.

Chapter 8

CONCLUSIONS

This thesis presented a search for the decay of long-lived neutral particles to heavy fermion pairs within the ATLAS detector at the LHC. Two analyses were performed: on 2012 data at $\sqrt{s} = 8$ TeV and on 2015 data at $\sqrt{s} = 13$ TeV data. In both cases the benchmark model was that of a heavy scalar decaying to two long-lived particles. No significant excess of events over the background estimate was observed in either search.

The 2012 search set limits on the proper decay length of the long-lived particle for heavy scalar masses ranging from 100 GeV to 900 GeV and long-lived particle masses ranging from 10 GeV to 40 GeV. For a Standar Model Higgs boson with an assumed branching ratio of 10% to long-lived particles this resulted in the exclusion of lifetimes between 0.10 m and 8.32 m, depending on the mass of the long-lived particle.

The 2015 search replaced the more complicated background method of the 2012 search with the ABCD method and altered cuts which had affected sensitivity to high energy jets in the earlier analysis. The analysis also introduced a boosted decision tree to identify candidate signal jets, which allowed for the consideration of more jet variables than could be done reasonably with a straight cut flow. While this iteration of the analysis was not sensitive to low mass scalar bosons, such as the Higgs boson, because of the high p_{T} requirements placed on jets, it did improve the acceptance for the high mass samples by a factor of 20.

The future of the analysis lies in advancing the use of machine learning techniques trialed in 2015. This can include improvments to the signal jet identification, but also event level and jet level rejection of non-collision background. Furthermore, replacement of simple requirements, such as that on $\log_{10}(E_{\mathrm{H}}/E_{\mathrm{EM}})$, with algorithms trained to estimate a particle's decay position within the calorimeter would allow for identificaiton of decays in the electromagnetic as well as the hadronic calorimeter, and aid in separating signal jets from neutral hadron showers originating at the primary vertex. With such advancements, the analysis should be able to continue setting competitive limits in future runs.

BIBLIOGRAPHY

[1] A. D. Martin, W.J. Stirling, R.S. Thorne, G. Watt. Parton distributions for the LHC. *Eur. Phys. J. C*, 63:189, 2009.

[2] Jean-Luc Caron. CERN Accelerator Complex (operating and approved projects), Jun 1991. General Photo.

[3] LHC Layout. https://profmattstrassler.files.wordpress.com/2011/07/lhclayout.jpg.

[4] Total Integrated Luminosity in 2012. https://atlas.web.cern.ch/Atlas/GROUPS/DATAPREPARATION/PublicPlots/2012/DataSummary/figs/sumLumiByDay.png.

[5] Total Integrated Luminosity in 2015. https://atlas.web.cern.ch/Atlas/GROUPS/DATAPREPARATION/PublicPlots/2015/DataSummary/figs/sumLumiByDay.png.

[6] ATLAS Collaboration. The ATLAS Experiment at the CERN Large Hadron Collider. *JINST*, 3:S08003, 2008.

[7] J. Pequenao, A. Maio. Virtual reality image of ATLAS with cavern walls and shafts visible, 2002. General Photo.

[8] ATLAS Collaboration. Expected Performance of the ATLAS Experiment - Detector, Trigger and Physics. CERN-OPEN-2008-020, 2007.

[9] ATLAS Collaboration. Triggers for displaced decays of long-lived neutral particles in the ATLAS detector. *JINST*, 8:P07015, 2013.

[10] Joao Pequenao, Paul Schaffner. An computer generated image representing how ATLAS detects particles, 16 Jan 2013. General Photo.

[11] ATLAS Collaboration. Jet energy measurement with the ATLAS detector in proton-proton collisions at $\sqrt{s} = 7$ TeV. *Eur. Phys. J. C*, 73 3:2304, 2013.

[12] R. Davis, D. S. Harmer, C. Kenneth. Search for Neutrinos from the Sun. *Phys. Rev. Lett.*, 20:1205, 1968.

[13] SNO Collaboration. Measurement of the rate of $\nu_\mathrm{e} + d \rightarrow p + p + e^-$ interactions produced by 8B solar neutrinos at the Sudbury Neutrino Observatory. *Phys. Rev. Lett.*, 87:071301, 2001.

[14] M. Gell-Mann. Symmetries of baryons and mesons. *Phys. Rev.*, 125:1067, 1962.

[15] P. W. Higgs. Broken Symmetries, Massless Particles and Gauge Fields. *Phys. Lett.*, 12:132, 1964.

[16] P. W. Higgs. Broken Symmetries and the Masses of Gauge Bosons. *Phys. Rev. Lett.*, 13:508, 1964.

[17] P. W. Higgs. Spontaneous Symmetry Breakdown without Massless Bosons. *Phys. Rev.*, 145:1156, 1966.

[18] F. Englert and R. Brout. Broken Symmetry and the Mass of Gauge Vector Mesons. *Phys. Rev. Lett.*, 13:321, 1964.

[19] G. S. Guralnik, C. R. Hagen and T. W. B. Kibble. Global Conservation Laws and Massless Particles. *Phys. Rev. Lett.*, 13:585, 1964.

[20] S. Glashow. Partial Symmetries of Weak Interactions. *Nucl. Phys.*, 22:579, 1961.

[21] S. Weinberg. A model of leptons. *Phys. Rev. Lett.*, 19:1264, 1967.

[22] A. Salam. Weak and Electromagnetic Interactions. *Conf. Proc.*, C680519:367, 1968.

[23] S. Chang, P.J. Fox, N. Weiner. Naturalness and Higgs Decays in the MSSM with a Singlet. *JHEP*, 0608:68, 2006.

[24] S. Chang, R. Dermisek, J.F. Gunion, N. Weiner. Nonstandard Higgs Boson Decays. *Ann. Rev. Nucl. Part. Sci.*, 58:75–98, 2008.

[25] M. J. Strassler, K. M. Zurek. Echoes of a Hidden Valley at Hadron Colliders. *Phys. Lett. B*, 651:374–379, 2007.

[26] M. J. Strassler, K. M. Zurek. Discovering the Higgs Through Highly-Displaced Vertices. *Phys. Lett. B*, 661:263–267, 2008.

[27] L. Evans and P. Bryant. LHC Machine. *JINST*, 3:S08001, 2008.

[28] T. Cornelissen, et al. Concepts, Design and Implementation of the ATLAS New Tracking (NEWT). ATL-SOFT-PUB-2007-007, 2007.

[29] E. Bouhova-Thacker, et al. Vertex Reconstruction in the ATLAS Experiment at the LHC. ATL-INDET-PUB-2009-001, 2009.

[30] ATLAS Collaboration. Performance of primary vertex reconstruction in proton–proton collisions at $\sqrt{s} = 7$ TeV in the ATLAS experiment. ATLAS-CONF-2010-069, 2010.

[31] ATLAS Collaboration. Performance of the ATLAS Inner Detector Track and Vertex Reconstruction in the High Pile-Up LHC Enviroment. ATLAS-CONF-2012-042, 2012.

[32] ATLAS Collaboration. Beam-induced and cosmic-ray backgrounds observed in the ATLAS detector during the LHC 2012 proton-proton running period. *JINST*, 11:P05013, 2016.

[33] ATLAS Collaboration. Electron and photon reconstruction and identification in ATLAS: expected performance at high energy and results at 900 GeV. ATLAS-CONF-2010-005, 2010.

[34] ATLAS Collaboration. Observation of inclusive electrons in the ATLAS experiment at $\sqrt{s} = 7$ TeV. ATLAS-CONF-2010-073, 2010.

[35] ATLAS Collaboration. Evidence for prompt photon production in pp collisions at $\sqrt{s} = 7$ TeV with the ATLAS detector. ATLAS-CONF-2010-077, 2010.

[36] ATLAS Collaboration. Identification of muon candidates in pp collisions at $\sqrt{s} = 900$ GeV with the ATLAS Detector. ATLAS-CONF-2010-015, 2010.

[37] ATLAS Collaboration. Studies of the performance of the ATLAS detector using cosmic-ray muons. *Eur. Phys. J. C*, 71:1593, 2011.

[38] ATLAS Collaboration. Calorimeter Clustering Algorithms: Description and Performance. ATL-LARG-PUB-2008-002, 2008.

[39] ATLAS Collaboration. Inputs to Jet Reconstruction and Calibration with the ATLAS Detector Using Proton–Proton Collisions at $\sqrt{s} = 900$ GeV. ATLAS-CONF-2010-016, 2010.

[40] ATLAS Collaboration. Jet kinematic distributions in proton–proton collisions at $\sqrt{s} = 900$ GeV with the ATLAS detector. ATLAS-CONF-2010-001, 2010.

[41] M. Cacciari, G. P. Salam and G. Soyez. The anti-k_t jet clustering algorithm. *JHEP*, 0804:063, 2008.

[42] Yu.L. Dokshitzer, et al. Better Jet Clustering Algorithms. *JHEP*, 9708:001, 1997.

[43] M. Wobisch, T. Wengler. Hadronization Corrections to Jet Cross Sections in Deep-Inelastic Scattering. *Proceedings of the Workshop on Monte Carlo Generators for HERA Physics*, 1999.

[44] ATLAS Collaboration. Data-Quality Requirements and Event Cleaning for Jets and Missing Transverse Energy Reconstruction with the ATLAS Detector in Proton–Proton Collisions at a Center-of-Mass Energy of $\sqrt{s} = 7$ TeV. ATLAS-CONF-2010-038, 2010.

[45] ATLAS Collaboration. ATLAS Calorimeter Response to Single Isolated Hadrons and Estimation of the Calorimeter Jet Scale Uncertainty. ATLAS-CONF-2011-028, 2011.

[46] ATLAS Collaboration. Determination of the ATLAS jet energy measurement uncertainty using photon-jet events in proton-proton collisions at $\sqrt{s} = 7$ TeV. ATLAS-CONF-2011-031, 2011.

[47] ATLAS Collaboration. Probing the measurement of jet energies with the ATLAS detector using Z+jet events from proton-proton collisions at $\sqrt{s} = 7$ TeV. ATLAS-CONF-2012-053, 2012.

[48] ATLAS Collaboration. Performance of missing transverse momentum reconstruction in proton–proton collisions at $\sqrt{s} = 7$ TeV with ATLAS. *Eur. Phys. J. C*, 72:1844, 2012.

[49] ATLAS Collaboration. Luminosity determination in pp collisions at $\sqrt{s} = 7$ TeV using the ATLAS detector at the LHC. *Eur. Phys. J. C*, 71:1630, 2011.

[50] ATLAS Collaboration. Improved Luminosity determination in pp collisions at $\sqrt{s} = 7$ TeV using the ATLAS detector at the LHC. *Eur. Phys. J. C*, 73:2518, 2013.

[51] Torbjorn Sjostrand, Stephen Mrenna and Peter Skands. A Brief Introduction to PYTHIA 8. *Comput.Phys.Commun.*, 178:852, 2008.

[52] ATLAS Collaboration. The ATLAS Simulation Infrastructure. *Eur. Phys. J. C*, 70:823, 2010.

[53] ATLAS Collaboration. Search for pair-produced long-lived neutral particles decaying to jets in the ATLAS hadronic calorimeter in pp collisions at $\sqrt{s} = 8$ TeV. *Phys. Lett. B*, 743:15, 2015.

[54] ATLAS Collaboration. Search for long-lived neutral particles decaying in the hadronic calorimeter of ATLAS at $\sqrt{s} = 13$ TeV in 3.2 fb^{-1} of data. ATLAS-CONF-2016-103, 2016.

[55] S. Alkire. Line of Fire in Hidden Valley Triggers.

[56] PAT User Analysis Tools. Pileup Uncertainties.

[57] A.L. Read. Presentation of search results: The CL(s) technique. *J. Phys.*, G 28:2693–2704, 2002.

[58] J. Alwall et al. The automated computation of tree-level and next-to-leading order differential cross sections, and their matching to parton shower simulations. *JHEP*, 07:079, 2014.

[59] R. Ball et al. Parton distributions with lhc data. *Nuclear Physics B*, 867(2):244–289, 2013.

[60] Freund, Yoav. Boosting a weak learning algorithm by majority. *Information and Computation*, 121:256–285, 1995.

[61] Quinlan, R. J. Bagging, Boosting, and C. *National Conference on Artificial Intelligence*, 1996.

[62] ATLAS Statistics Forum. ABCD Method in Searches.

[63] ATLAS Collaboration. Search for long-lived neutral particles decaying into displaced lepton jets in proton–proton collisions at $\sqrt{s} = 13$ TeV with the ATLAS detector. ATLAS-COM-CONF-2016-091, 2016.